XENON POLARIZER CHARACTERIZATION AND BIOLOGICAL STUDIES

by

Geoffry M. Schrank

A dissertation submitted to the faculty of
The University of Utah
in partial fulfillment of the requirements for the degree of

Doctor of Philosophy

in

Physics

Department of Physics and Astronomy

The University of Utah

May 2010

ProQuest LLC
789 East Eisenhower Parkway
P.O. Box 1346
Ann Arbor, MI 48106-1346

THE UNIVERSITY OF UTAH GRADUATE SCHOOL

SUPERVISORY COMMITTEE APPROVAL

of a dissertation submitted by

Geoffry M. Schrank

This dissertation has been read by each member of the following supervisory committee and by majority vote has been found to be satisfactory.

8 Sept. 2009 — [redacted]
Chair: Brian Saam

Sept 8. 2009 — [redacted]
Alexei Efros

September 8th 2009 — [redacted]
Stephan LoBohec

Sept. 8, 2009 — [redacted]
Jordon Gerton

8 Sept 2009 — [redacted]
David Goldenberg

THE UNIVERSITY OF UTAH GRADUATE SCHOOL

FINAL READING APPROVAL

To the Graduate Council of the University of Utah:

I have read the dissertation of Geoffry M. Schrank in its final form and have found that (1) its format, citations, and bibliographic style are consistent and acceptable; (2) its illustrative materials including figures, tables, and charts are in place; and (3) the final manuscript is satisfactory to the Supervisory Committee and is ready for submission to The Graduate School.

3 Dec. 2009
Date

[redacted]
Brian Saam
Chair, Supervisory Committee

Approved for the Major Department

[redacted]
David Kieda
Chair/Dean

Approved for the Graduate Council

[redacted]
David S. Chapman
Dean of The Graduate School

ABSTRACT

I will describe a low-pressure flow-through ^{129}Xe polarizer and report its performance by examining both the output ^{129}Xe and in situ Rb polarization. The ^{129}Xe polarization was made using standard NMR techniques, and the Rb polarization measurement was made using optically detected electron paramagnetic resonance. I compared the results of these measurements to a one-dimensional numerical model of the system. While we qualitatively understand the behavior of the system, the comparison between measurement and model reveals several inadequacies in our understanding of many important physical mechanisms. I will discuss the relevant physics necessary to qualitatively understand the system's behavior and suggest what mechanisms may cause the discrepancies in the modeled and measured behavior.

I will demonstrate the utility of this Xe polarizer by measuring xenon's chemical shift dependence on the concentration of Bovine Pancreatic Trypsin Inhibitor (BPTI) and some of its mutants. Mutants Y23A and F45G have measured dependence of 0.56 ± 0.05 ppm/mM and 0.47 ± 0.07 ppm/mM, respectively, which is consistent with relatively strong, manufactured binding sites in the structure. Wild type BPTI has a measured dependence of only 0.15 ± 0.02 ppm/mM, suggesting that there exists no specific binding site to which Xe can bind. Finally, the mutant Y35G has a dependence of 0.10 ± 0.07 ppm/mM. This, with previous data, suggests that a large fraction of solution-phase Y35G does not exist in a conformation that allows Xe access to its binding cavity.

to the Lord Almighty

He created all that I study

He gave me the intellect to understand

"The papers we publish are islands of reproducibility in a sea of what-the-hell."

– B. Saam

CONTENTS

LIST OF FIGURES

LIST OF TABLES

ACKNOWLEDGMENTS

I would like to acknowledge the support and contributions of all those who were involved in the work of this thesis. I gratefully acknowledge the help of Kevin Teaford for work on glass cell fabrication, Ed Munford and Roy Rydman for metal component fabrication and consultation, Kim Butler and Liz Dupont for their assistance with construction of the polarizer, and Aiyesha Ma for data extraction software. Also, I acknowledge the assistance of Zayd Ma and Allison Schoeck in experiment design, data taking, and device production. I would also like to thank David Goldenberg, David Ailion, Peter Flynn, Dennis Edwards, Mark Solom, Gernot Laicher, Eric Sorte, Ben Anger, Steve Morgan, and Brian Saam for helpful discussions.

I also need to recognize the friends and family that supported me during my tenure at the University of Utah. Most of those listed above helped not only in the experimental work, but also helped prevent me from spending all of my time in the lab. In addition, I want to thank Nate Shepherd, David Pawlowski, and Josh Holt for keeping me sane during the first few years of graduate school. I also want to thank Bob Hill; Jim Williams; Andrew, Sarah, and Peter Reikoester; Royal and Alexandria Easton; Lee, Heather, Madline, and Grace Fuhrken; Josh and Becky (and now Miriam) Speulda; and Roger and Pam Martin for their unrelenting encouragement throughout the entire process. Finally, I need to thank and acknowledge my parents, Steve and Deborah Schrank, my brothers, Jon and Joel Schrank, and my God, without whom I never would have reached a place where I could enter graduate school, let alone complete it.

CHAPTER 1

INTRODUCTION

1.1 Hyperpolarized Noble Gases

1.1.1 Overview of Spin-Exchange Optical Pumping

Spin-Exchange Optical Pumping (SEOP) is a process that creates nonthermal populations in nuclear Zeeman-split energy levels. This population difference is generally expressed in terms of polarization, and for spin $\frac{1}{2}$ particles it can be written as:

$$P = \frac{N_\uparrow - N_\downarrow}{N_\uparrow + N_\downarrow} \tag{1.1}$$

where $N_\uparrow$ and $N_\downarrow$ are the populations of the minus and plus $\frac{1}{2}$ states. We accomplish SEOP in two steps: transfer of spin angular momentum from photons to an alkali metal atom via its electron and then transfer from that atom to the gas nuclei of interest via the alkali metal atom's electron.

In the first step of SEOP, called depopulation optical pumping, the spin angular momentum of circular polarized laser light is transferred to the alkali metal electrons. This step is shown schematically in Figure 1.1. A circularly polarized beam of light is composed of photons that have either spin +1 or -1, depending on the particular helicity. For most SEOP experiments, one uses σ^- polarized light with spin -1. The light is at a wavelength such that it induces an electronic transition in the alkali metal from the ground state to the first excited state. The σ^- imposes a selection rule requiring the azimuthal spin quantum number to change by -1. As electrons are spin $\frac{1}{2}$ particles, this selection rule has the effect of moving the population from the spin $+\frac{1}{2}$ state to the spin $-\frac{1}{2}$. The Rb electrons in the spin $-\frac{1}{2}$ state are transparent to the light because they cannot make a transition to satisfy the selection rule.

The existence of the selection rule can easily be seen by applying first order time-dependent perturbation theory to a two level system.[1] Consider the σ^- polarized light to be the perturbing Hamiltonian. The light only interacts with the electron spin via magnetic coupling. Therefore, we can write the Hamiltonian as

$$V = \mu \cdot B = Re(\gamma\hbar B_L \left(I_x e^{i\omega t} - iI_y e^{i\omega t}\right)) = Re(\gamma\hbar B_L e^{i\omega t} I_-) \tag{1.2}$$

[1]One can find a good review of first order time-dependent perturbation theory in Sakurai's *Modern Quantum Mechanics* [1].

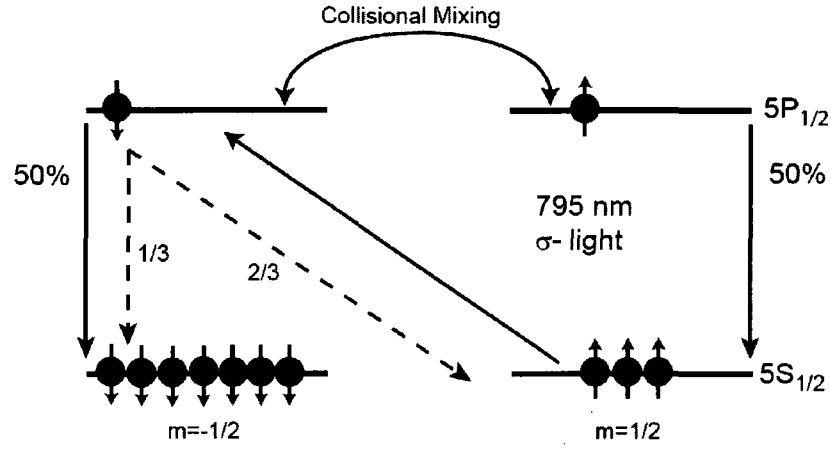

Figure 1.1. A schematic of depopulation optical pumping of rubidium. Circularly polarized light can only induce transitions from the m=$\frac{1}{2}$ state. Any electrons in the m=$-\frac{1}{2}$ state are transparent to the light. Once excited to the $5P_{1/2}$ level, collisions with other species in the system cause the excited state magnetic sublevels to equalize. Thus, the excited electron relaxes to either magnetic sublevel ground state with equal probability. However, since we are only exciting electrons in the m=$\frac{1}{2}$ state, this level will depopulate. Figure adapted with thanks to Ben Anger.

where γ is the gyromagnetic ratio of the alkali electron, B_L is the magnitude of the magnetic field component of the incident light, ω is the angular frequency of the light, I_x and I_y are the dimensionless Pauli spin matrices, and I_- is the dimensionless lowering operator. The lowering operator guarantees that all of the transition probabilities are zero except for the transition that lowers the spin angular momentum by one unit. For a spin-$\frac{1}{2}$ particle such as an electron, this corresponds to only the transition from the $+\frac{1}{2}$ state to the $-\frac{1}{2}$ state.

The alkali electron would normally relax back to its ground state by emitting an unpolarized photon. This is an undesirable relaxation process because the emitted photon is randomly polarized and may scatter several times in the vapor. This process, called radiation trapping, can degrade the produced polarization in SEOP experiments [2]. For this reason, we frequently introduce some quantity of nitrogen into the mixture. The nitrogen will quench the excited atoms, that is collide with excited alkali atoms, causing them to relax to the ground state nonradiatively. It is known that the nitrogen then disperses the energy associated with the relaxation in the vibrational and rotational modes of the molecule. Nitrogen is used because of its large quenching cross section, which has been measured to be in excess of 50 Å^2 [2].

The nitrogen also aids in the depopulation pumping process by redistributing the

excited state electrons among their Zeeman sublevels in a process called collisional mixing. In the absence of collisional mixing, the Clebsh-Gordon coefficients are $\frac{2}{3}$ for the transition between the levels with different azimuthal spin quantum numbers and only $\frac{1}{3}$ for the levels with the same azimuthal quantum numbers [3]. Thus, it is more likely for the electron to relax back into the state from which the circularly polarized light excited it. The collisional mixing quickly equalizes the spin populations of the excited states causing the transition probabilities to also be equal. Under these conditions, it takes an average of two σ^- photons to pump an electron into the $-\frac{1}{2}$ ground state.

In the second step of the process of SEOP, called spin-exchange, a polarized Rb atom interacts with a noble gas nucleus to transfer the spin angular momentum in the Rb electron to the nuclei. This interaction has the form $H = \alpha \mathbf{I} \cdot \mathbf{S}$, where $\mathbf{I}$ is the nuclear spin of the noble gas, $\mathbf{S}$ is the electron spin of the Rb, and α is the coupling coefficient, which is dependent of the separation of the atoms. This interaction is known as the Fermi contact interaction. One of the possible results of this interaction is the desired exchange of spin from the Rb electron to the noble gas nuclei.

The full atomic dipole interaction Hamiltonian is given by [4]

$$H_{dipole} = \gamma_e \gamma_n \hbar^2 \left\{ \frac{[\mathbf{I} \cdot \mathbf{S} - 3(\mathbf{I} \cdot \hat{\mathbf{r}})(\mathbf{S} \cdot \hat{\mathbf{r}})]}{r^3} + \frac{8\pi}{3} \mathbf{I} \cdot \mathbf{S} \delta(\mathbf{r}) \right\}. \tag{1.3}$$

It is the second term in this expression that gives rise to the Fermi contact interaction. Because of the δ function, the term is only realized between the nuclei and electrons with substantial S character. Other electrons' wave functions do not overlap the nucleus.

The term $\mathbf{I} \cdot \mathbf{S}$ can be written as $I_z S_z + I_+ S_- + I_- S_+$. The raising and lowering operators in the last two terms give rise to the spin-exchange between the Rb electron and the noble gas nuclei. There are other interactions, which will be treated in more detail later, that can flip the Rb spin without changing the noble gas nuclear spin. However, spin-exchange occurs with sufficient efficiency to create large nuclear polarizations in the noble gas.

A good review of current spin-exchange optical pumping theory can be found in Ref. [5].

1.1.2 Historical Overview of Spin-Exchange Optical Pumping

Optical pumping dates back to 1940s when Kastler proposed illuminating alkali vapors with circularly polarized light to obtain nonthermal populations in the spin angular momentum sublevels [6]. Brossel et al.[7] later tested this on sodium nuclei. In 1960, a group at Princeton achieved spin-exchange between Rb and ^{3}He[8]. Although they only achieved a very small polarization, 0.01%, it represented a polarization orders of

magnitude greater than thermal polarization. This work led to the field of hyperpolarzied (HP) gases.

1.1.2.1 Polarization of ^{3}He

The first nucleus successfully polarized using spin-exchange optical pumping was ^{3}He and it has continued to be used in many SEOP experiments. ^{3}He has a small cross section for spin-exchange with alkali metals, and so the time spin-exchange time is slow, measured in tens of hours. ^{3}He also has a very long relaxation time, also measured in the tens of hours.

Various groups have done research into methods of accelerating the spin-exchange process in ^{3}He. One method that has proven successful is hybrid pumping, where one uses two alkali metals to polarize ^{3}He [9]. The first alkali metal, usually Rb, is very effectively optically pumped, the second alkali metal, usually K, is very effective at spin-exchange. The K has a better spin-exchange efficiency by approximately a factor of ten. The Rb is optically pumped using conventional techniques, and the two alkali metals rapidly exchange spin so that the K become spin polarized. The K can then interact with the ^{3}He and induce rapid spin-exchange. By this method, one can saturate the ^{3}He polarization in less than ten hours.

1.1.2.2 Polarization of ^{129}Xe

In contrast to ^{3}He, spin-exchange time in ^{129}Xe is measured in minutes to tens of seconds [10]. It owes this to a large spin-exchange cross-section and its ability to form long-lived molecules with Rb.

^{129}Xe has a large and highly deformable electron cloud, and a Rb atom that slightly penetrates the cloud will immediately begin to feel the electric field of the ^{129}Xe nucleus, which strongly attracts the Rb atom. As the Rb atom penetrates further into the electron cloud less of the Xe nucleus is screened, and the Rb experiences an increasing attraction. Thus, the Rb atom is able to get very close to the Xe nucleus to effectively and quickly exchange spin.

^{129}Xe is also able to form long-lived van der Waals molecules with Rb. These molecules facilitate longer interaction times between Rb and ^{129}Xe and thus increase the probability of spin-exchange. A proposed expression spin-exchange rate for ^{129}Xe with Rb is given by [11]

$$\gamma_{SE} = \left(\frac{1}{\frac{[Xe]}{\gamma_{Xe}} + \frac{[N_2]}{\gamma_{N_2}} + \frac{[He]}{\gamma_{He}}} + \langle \sigma_{SE} v \rangle \right) [\mathrm{Rb}] \tag{1.4}$$

where γ_{SE} is the spin-exchange rate, $[G]$ is the concentration of the respective gases or alkali metal, $\langle \sigma_{SE} v \rangle$ is the velocity-averaged spin-exchange cross section for binary Xe-Rb

collisions, and γ_G is the van der Waals specific spin-exchange rates for the respective gases. The first term in the parentheses is due to the molecular interaction of ^{129}Xe and Rb, and the second term is due to the binary collisions between noble and the alkali. This proposed expression has some faults as we will see in Chapter 4.

1.2 Methods of ^{129}Xe Polarization

1.2.1 Batch Mode Polarization

One method of polarizing ^{129}Xe, called batch mode, is illustrated in Figure 1.2. In batch mode, a glass cell containing a moderate pressure of Xe (100-1000 mbar) and a macroscopic amount of Rb metal is heated in an oven to establish a moderate Rb vapor pressure. It is optically pumped with a high-powered laser tuned to the frequency corresponding to the Rb D_1 transition. After minutes, the gas reaches a saturated polarized state. It can then be removed from the pumping setup and used in an experiment. This technique has been successfully implemented by Pines et al. to achieve a ^{129}Xe nuclear polarization of 0.5% [12]. Rosen et al. [13] used a system with several orders of magnitude more laser power and reported 7.5% polarization.

Batch mode is advantageous because of its simplicity. There is no requirement of monitoring flow rates or maintaining pressures. Using a moderately precise pressure gauge, one can fill a cell and know the densities of Xe and buffer gases to within a few percent. Once the gas mixture is transferred to the polarizing cell, its number density and relative make-up remain during the SEOP process. Batch mode is disadvantageous because it is not a continuous process. If a particular experiment relaxes all of the ^{129}Xe, it will take tens of minutes before fresh HP ^{129}Xe can be obtained to continue the experiment. For experiments that quickly destroy ^{129}Xe polarization and require averaging, this is particularly undesirable. Batch mode also severely limits the quantity of ^{129}Xe one can produce. High densities of Xe required to efficiently use SEOP in batch mode will quickly destroy Rb spin polarization, and the ultimate Xe polarization will suffer as a result.

Despite these disadvantages, batch mode spin polarization of ^{129}Xe is still a very useful technique for experiments that do not require high pressures of Xe and do not require a continuous supply of polarized ^{129}Xe.

1.2.2 Flow-Through Mode

Batch mode polarization of ^{129}Xe is not the preferred method of creating high polarization due to low spin-exchange efficiency at high Xe densities. This low efficiency is due to the strong spin-rotation interaction the Rb experience during collisions with Xe atoms [2]. The spin angular momentum in the Rb electron readily couples to the

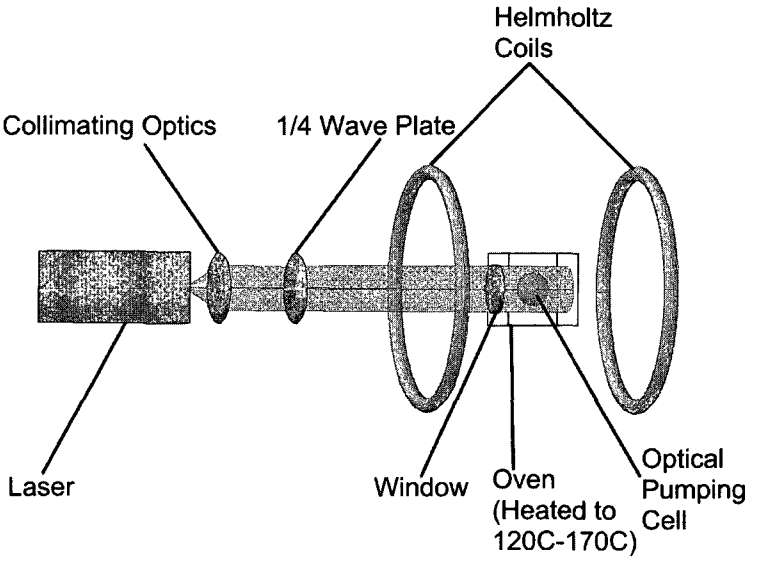

Figure 1.2. Batch mode pumping is the simplest method of SEOP. A transparent cell is place in an oven and illuminated with laser light. Most modern batch mode SEOP setups use high-powered laser diode arrays with a large angular divergence. It is necessary to decrease this divergence otherwise a large fraction of the light intensity will not illuminate the cell resulting in a smaller alkali metal polarization. Here the collimating optics are shown schematically as a single element, although proper collimation generally requires more than one. After collimation, the linear polarized laser light passes through a $\frac{1}{4}\lambda$-plate. This transforms the light into circularly polarized light of the desired helicity to excite the alkali metal.

angular momentum of the two atoms about each other and can relax the Rb electron without undergoing spin-exchange. The Rb polarization will thus drop with increasing Xe densities. As the ultimate ^{129}Xe polarization is limited by the Rb polarization, the ^{129}Xe polarization suffers as well.

The current method to address this is by flowing lean mixtures of Xe through an optical pumping cell. Spin-exchange for ^{129}Xe is fast, of order tens of seconds to minutes, and the ^{129}Xe polarization saturates in the time it takes for the gas to pass through the cell. The Xe density is kept low enough to not seriously impede the polarization of the Rb.

This process was pioneered by Driehuys et al. [14] at Princeton University. They reported polarizing ^{129}Xe to 5% after cryogenic separation and 22% in the gas phase. They used a 140 W laser diode array to provide light to optically pump the Rb vapor. The laser was spectrally very broad (2-3 nm), so $\approx$ 10 atm of buffer gases (gas that did not undergo spin-exchange) were used to broaden the Rb absorption line to more efficiently use the incident light.

Since then, other groups have produced similar polarizers based on the same concept. Most recently, Ruset et al.[15, 11] at the University of New Hampshire designed and produced a flow-through system that contained several unique ideas. The first was to polarize ^{129}Xe in the low-pressure regime (1 atm or less) due to higher spin-exchange rates realized in this regime.[1] The second was to use a longer optical pumping region to better utilize the available pumping light and to allow the Xe to spend a longer resident time in the pumping region. Third, the Xe mixture flowed counter to the direction of the propagation of the pumping light to achieve the highest Rb (and thus ^{129}Xe) polarization just as the Xe left the pumping region. Finally, the polarizer employed an extended Rb presaturation region to fully saturate the gas mixture with alkali vapor before entering the optical pumping region. Figure 1.3 shows a schematic of this design and highlights some of its features. After polarization, the current practice is to separate the polarized Xe by freezing it in a coldfinger. The freezing point of Xe is much higher than the buffer gases that are normally used. In addition, the relaxation time of ^{129}Xe at 77 K in a field of thousands of gauss is of order 2.5 hours [17]. One can accumulate liters of highly polarized Xe for a given experiment.

1.3 Hyperpolarized Gas Research and Applications

HP gases have found use in varied fields of science and have made low-density gas phase Nuclear Magnetic Resonance (NMR) possible. HP gases have also found use in high energy physics where ^{3}He nuclei has been used as a target that lead to discovery of spin-structure of the neutron [18]. HP ^{3}He is also being used to search for parity violation in the weak interaction between the proton and the neutron[19] and in the search for the neutron dipole moment [20]. Most notably and spectacularly, ^{3}He has been used for human and animal lung imaging and study of pulmonary function [21, 22].

^{129}Xe has probed equally useful in fields outside of study of hyperpolarized gases. ^{129}Xe has been found useful for characterizing porous materials using NMR. The Pines group at University of Berkley California uses it in a multitude of experiments including as a dipolar sensor [23], to characterize proteins and distinguish different protein conformations [24, 25], and as functionalized biosensor for cell or tissue spectroscopy or imaging [26]. Our own group has used hyperpolarized ^{129}Xe solid to study long-time behavior in solid spin decays [27]. These lists are far from exhaustive, and new application for hyperpolarize gas are continuing to be discovered.

---

[1] Until 2000, to effectively use the broad diode laser sources, the Rb had to be optically pumped at high gas pressures to broaden the absorption line. With the advent of external frequency narrowing of diode laser arrays [16], this is no longer necessary. See section 2.3.1.2 for more information.

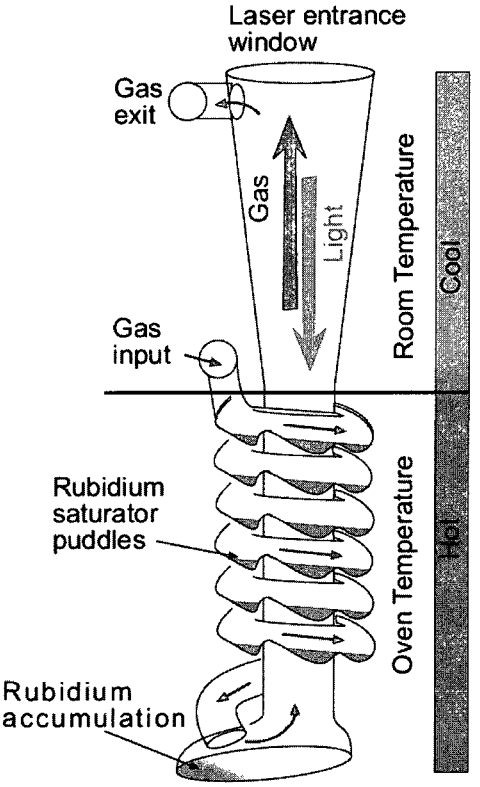

Figure 1.3. The most recent design for flow-through ^{129}Xe polarization is the Ruset et al. [15] design. The design features a Rb pre-saturation region to assure the gas mixture is completely saturated with Rb vapor before entering the optical pumping region, a long optical pumping region, and counter propagation of the light with respect to the gas flow. The entire system is designed to operate at or below 1 atm. The upper half of the optical pumping cell is cooled to assure that regions down stream of the cell do not contain high densities of unpolarized Rb vapor as this would promote spin-relaxation in the ^{129}Xe. The entire cell is contained in seven coils in Helmholtz configuration, which provide a magnetic field of $\approx$ 30 G. Figure adapted from [11] and used with permission.

1.4 Dissertation Summary

This dissertation will explore the large-scale production of HP ^{129}Xe by flow-through polarization and demonstrate a biophysical application. First, it will describe a new flow-through polarizer, based on the Ruset design [15], built by our group. It will explore the behavior of the polarizer by describing the measured output ^{129}Xe polarization and the in situ Rb polarization as a function of a number of parameters: oven temperature, Xe concentration, total pressure, and total gas flow rate. Each of these parameters affects different physical quantities in the system, and the measurements provide excellent diagnostics of our understanding of the underlying physical mechanisms. Next, it will compare the polarization measurements to a numerical model which contains all the

known relevant physics of the system. Finally, the dissertation will demonstrate the utility of highly polarized gas by characterizing the interaction of Xe with Bovine Pancreatic Trypsin Inhibitor (BPTI) and some associated mutants.

The interested reader may refer to reference [28] for complimentary information on the data presented in Chapters 2, 3, and 4.

CHAPTER 2

IMPLEMENTATION OF A ^{129}XE FLOW-THROUGH POLARIZER

2.1 Introduction

In this Chapter, we will look at the mechanics of building a ^{129}Xe flow-through polarizer. This Chapter will contain technical information on the design and construction of such polarizer.[1] The end of this Chapter contains a discussion on the performance of our polarizer, discussion on the results, and suggestions on how to improve the performance.

2.2 Introduction to Polarizer Designs

There have been a plethora of designs for flow-through polarizers. Some of these designs were briefly discussed in the introduction. In this Section, we will examine some of the various designs in more detail and comment on the advantages and disadvantages of each.

2.2.1 Standard Designs

The first flow-through polarizer of was produced by the Happer group at Princeton in 1996 [14]. The optical pumping cell for this polarizer was a 25 mm diameter, 80 mm long cylinder housed in an oven heated between 130 °C and 150 °C. The gas through the cell was premixture of 98% ^{4}He, 1% N_2, and 1% Xe. The gas mixture first passed through a zirconium getter to remove impurities. It then passed over hot copper wool mesh containing Rb to introduce Rb vapor into the gas stream. After polarization, the gas stream was directed into a cold finger to cryogenically separate the hyperpolarized Xe. The system operated at high gas densities of $\approx$10 amagat to pressure-broaden the Rb D_1 line to increase the fraction of light absorbed by the Rb. A 140 W broad (2-3 nm) diode laser array (DLA) provided light to excite the Rb. The authors report producing 1 liter of Xe polarized to 5%.

---

[1] For those interested in designing and constructing a flow-through polarizer or any piece of scientific equipment, I suggest browsing *Building Scientific Apparatus: A Practical Guide To Design And Construction* by Moore et al. [29].

The group members started a company in 1996 producing flow-through polarizers of the type described by Driehuys et al. [14]. The company was later purchased by Amersham Helath and then by GE. Currently, GE holds the rights on flow-through polarizers of the Driehuys type.

In 1999, the Pines group at Berkley described a continuous loop flow-through polarizer [30]. Like the Princeton polarizer, this polarizer operated at pressures ≈10 amagat. The novelty of this design lay in the recirculation of the gas mixture after passing it through the experiment of interest. A premixture of gas was admitted into the loop, polarized, passed over the sample of interested, and then went through a gas circulation pump. This polarizer had the advantage of providing a continuous supply of hyperpolarized Xe over the sample without losing the Xe. Unfortunately, the Xe that passed over the sample had to be at a low partial pressure in order achieve fairly high polarization.

Our own group produced a closed loop flow-through polarizer [31]. However, unlike the Berkley polarizer, our polarizer circulated the gas via convection. The front half of the optical pumping cell was heated to ≈100°C and illuminated with appropriate light. The back half of the cell was cooled just below the liquid point of Xe. Convection drove HP Xe from the front of the cell where it condenses in the rear and forms a column of HP liquid Xe. Phase exchange between the gas and liquid kept the liquid column hyperpolarized indefinitely. The liquid could either be used as a solvent to study other materials or it can be frozen to explore properties of the HP solid.

The Bowers group at the University of Florida developed a very high power laser flow-through polarizer [32]. Also a polarizer like that described by Driehuys, the novelty of the design lay in the use of 210 W of laser power provided by seven laser diode arrays. The line width of the laser employed was only 1.6 nm, which allowed them to operate at the lower total pressures of 4.5 atm. The group reported polarizations as high as 67% for a mixture of consisting of 0.6% Xe and a total flow rate of ≈400 sccm.

2.2.2 UNH Novel Design

In 2006, Hersman's group at the University of New Hampshire announced a novel, high capacity flow through polarizer [15] that employed four important innovations. First, the total gas pressure in the polarizer was at or below a standard atmosphere. Previous polarizers employed total gas pressure of 4-10 atm to pressure-broaden the Rb absorption line. However, Xe-Rb spin-exchange rates can be up to five times faster in the low pressure regime, and with new external laser narrowing techniques available [16], pressure broadening of the Rb absorption line was not as important. Second, the optical pumping cell was much longer than those used in previous polarizers. Hersman's polarizer employed a two meter long optical pumping cell, while previous polarizers used cells ≈10 cm long.

The long optical pumping region provided a long resident time for ^{129}Xe to interact with highly polarized Rb while still maintaining high flow rates. Third, the direction of the flow of the gas was opposite the direction of the propagation of the laser beam. The counter-flow of the gas assured the ^{129}Xe experienced the most highly polarized Rb at the outlet of the optical pumping cell. As light propagates through the optical pumping cell, light is attenuated by the Rb vapor. As a result, the Rb polarization drops in the lowest portions of the optical pumping cell. To prevent polarization losses in the ^{129}Xe due to interaction with low polarized Rb, the Xe leaves the optical pumping cell at the point where the Rb polarization is the highest.

2.3 VOLoPXePol Design

Our group developed two Vertically Oriented Low Pressure Xenon Polarizers (VOLoPXePol's) like those described by Ruset et al. [15] However, we attempted to simplify many of the structures employed by the Hersman group in the implementation of their polarizer, and the results were comparable.

In this Section, we will examine the equipment and materials used to implement the Utah polarizers. This should provide a useful guide for those involved in the development of their own polarizers or interested in improving this design.

The two polarizer differ slightly in their design. I will refer to the first polarizer as Polarizer 1 and the second polarizer as Polarizer 2. Most of the data presented here were taken with Polarizer 2. In the next Sections, I will describe the two polarizers and their differences.

2.3.1 Laser and Optics

Circularly polarized light coupled well into the optical pumping cell is necessary to achieve very high polarizations. Sloppy implementation can result in loss of intensity at the cell resulting in lower polarization. One must take careful care to properly narrow, align, and collimate the beam.

2.3.1.1 Laser

Two different lasers were used for the two polarizers. Polarizer 1 used an nLight 100 W laser diode array. The laser package required directly cooling, that is, it required deionized cooling water to flow into the laser package. The company provided a water manifold to mate the laser package to water supply. The resistivity of the water had to be carefully controlled. Thus, the water chiller incorporated a deionization loop that actively monitored the resistivity of the water. The temperature of this laser could be only grossly controlled by the set point of the water chiller. It was noted that fluctuations in ambient

room temperature could effect the temperature at the laser diode. Diode lasers' spectral characteristics depend on the temperature at the junction. The temperature fluctuations required daily tuning of the water chiller's temperature set point to optimize the diode's lasing frequency.

A Lambda ZUP 6-132/U, capable of 6V and 132A variable output, powered the laser. The supply was interlocked with two temperature sensors and a flow sensor designed to cut the power to the laser in case of a failure in the cooling system.

Polarizer 2 incorporated a 50 W QPC laser diode array. Unlike the nLight diode, this laser was convection cooled. We built a mounting plate to which we attached the laser. Indium foil between the laser and the mounting plate enhanced thermal contact between the two. Behind the mounting plate lay a Thermal Electric Cooler (TEC). By applying a voltage, the TEC became a heat engine, and one side of the TEC become cold and the other warm. The TEC used for this laser was rated to transport a maximum of 50 W of heat. The warm side of the TEC thermally contacted a plate through which chilled water ran.

A temperature sensor glued to the anode of the diode monitored the laser's temperature and relayed that information to a Omega CNi 16D53 Controller. The Controller attempted to keep the temperature of the laser at some set point by varying the current through the TEC. Using this method, the laser junction temperature stayed within 0.05 °C of the set point temperature. Since the temperature controller monitored the temperature at the laser, there was no need to daily tune the set point temperature to optimize the laser spectral characteristics.

This laser was powered by a Power Ten supply capable of 10 V, 100 A output. This supply was similarly interlocked to prevent damage to the laser in case of cooling failure.

The manufactures' specifications for both laser are given in Table 2.1.

Table 2.1. The specifications for both lasers used in the construction of the two Utah polarizers.

	Polarizer 1	Polarizer 2
Laser Part #	nLight NL-Cascades-100-794	QPC 4101-B
Output Power(W)	100	50
Fast Axis Divergence (deg.)	<36	<40
Slow Axis Divergence (deg.)	≤10	<10
Smile(μm)	<2	Not Specified
Temperature Dependence (nm/°C)	0.3	0.28

2.3.1.2 External Cavity

The typical free-running spectral line width of high powered diode array lasers is 2-3 nm, and the Rb absorption line's natural line width is 0.0117 pm [33]. The optical pumping rate,γ_{opt}, of the Rb is given by [34]

$$\gamma_{opt}(z) = \int_0^\infty \psi(\nu, z)\sigma_s(\nu)d\nu, \tag{2.1}$$

where $\psi(\nu, z)$ is the photon flux density, $\sigma_s(\nu)$ is the Rb absorption line shape, and ν is the frequency. The optical pumping rate is not strongly influenced by light that is outside the spectral width of the Rb absorption line, thus to maximally use the available light, it is advantageous to at least match the spectral widths of the Rb absorption line and the pump light.

Although this is generally not realized in an experimental setup, we do take care to try to match the line widths as well as possible. Until recently, this was done by adding a large density ($\approx$10 amagats) of buffer gas to pressure broaden the Rb absorption line. Buffer gases generally add about 18 GHz per amagat to the Rb line width [35].

It is possible to narrow the spectral width of the pumping laser by an order of magnitude using an external Littrow cavity. In a Littrow cavity, the light from the laser is directed onto a diffraction grating. The first order reflection from the grating is directed back into the laser, which serves to narrow the laser and allows for frequency selection. The zeroeth order reflection is used as the laser output.

DLAs add difficulty to this simple arrangement due to the misalignment (smile) of laser emitters and the large divergence angles. Due to the manufacturing process, diode array emitters do not lay on a straight line but rather along a bowed curve. The typical diode offset can be between 1-10 μm. Diode arrays also tend to have large divergence angles, as high as 40° (the fast axis) along the axis perpendicular the line of diodes and about 10° along the axis parallel to the line of the diodes (the slow axis).

The difficulty these two artifacts introduce can be understood by examining the equation governing the Littrow feedback condition for light propagating in the $\hat{z}\cos(\alpha)\cos(\phi)+\hat{y}\sin(\alpha)+\hat{(x)}\sin(\alpha)\sin(\phi)$ direction as was done by Chann et al. [16]:

$$\lambda = 2d\sin(\theta - \phi)\cos(\alpha) \tag{2.2}$$

which can be approximated as

$$\frac{\delta\lambda}{\lambda_0} \approx \frac{-\alpha^2}{2} - \phi\cot(\theta), \tag{2.3}$$

where $\lambda_0 = 2d\sin(\theta)$, $\delta\lambda = \lambda - \lambda_0$, θ is the angle between the incident light and the normal of the grating, α is the divergence of the light along the slow axis, and ϕ is the

angle due to the smile of the laser. $\delta\lambda$ increases proportionally to both the divergence angle and the angle due to the smile. Chann et al. [16] proposed two solutions to this difficulty. First, a cylindrical lens was generally attached to the laser diode array by the manufacturer to reduce the slow axis divergence. Second, one can send the light through an afocal telescope with magnification $M > 1$. The telescope reduced the angular spread both due to the divergence and the smile by a factor of $1/M$. Specifically, for a laser with divergence α_0 and smile offset x, the narrowed line width of a laser using telescope and collimating cylindrical lens of focal length f_c has been shown to be[16]

$$\frac{\delta\lambda}{\lambda} = \frac{x\cot(\theta)}{Mf_c}. \tag{2.4}$$

We employed such a setup for both polarizers. Figure 2.1 shows a schematic of the setup. The diffraction grating was mounted to an L-bracket with a corotating mirror.

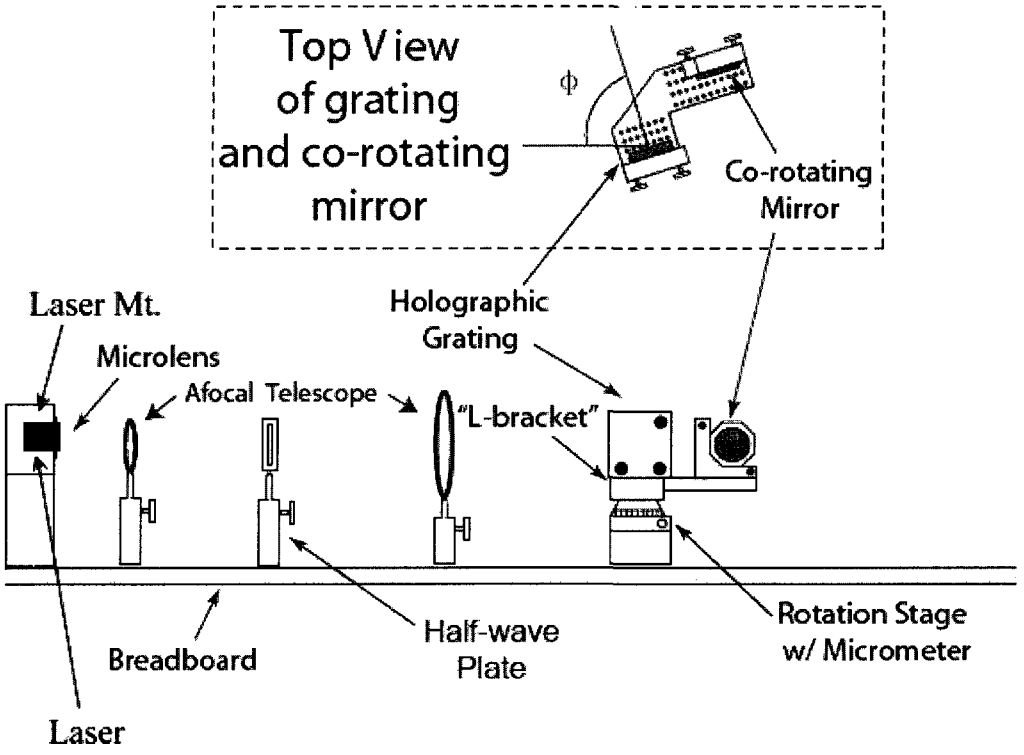

Figure 2.1. The layout of the laser diode array and narrowing feedback optics. The manufacturer mounted a cylindrical collimating micro-lens to the front of the laser. The lenses used in the afocal telescope have focal lengths of 50.8 mm and 200 mm giving a magnification of ≈ 4. The half waveplate is placed near the focus of the first lens because of the small aperture of the waveplate. The corotating mirror is mounted such that it directs the zeroth order reflection parallel to the original optical path. Figured adapted and used with permission with thanks to Jared Teter.

The mirror redirected the zeroth order reflection along the original optical path. This allowed us to rotate the diffraction grating for laser tuning without seriously disrupting optical alignment after the grating.

A half wave plate was placed near the focal point of the telescope to allow for rotation of the linear polarization of the laser light. The efficiency of the grating is defined as the ratio of the power of the light reflected in the m^{th} order and the power of the incident light and is dependent on the angle the polarization makes with respect to the grooves. Figure 2.2 shows the quoted efficiency of our grating for s-polarization and p-polarizations. A relatively small amount of feedback was required to effectively narrow our diode arrays, so the angle the electric field vector made with the grating grooves was kept very small.

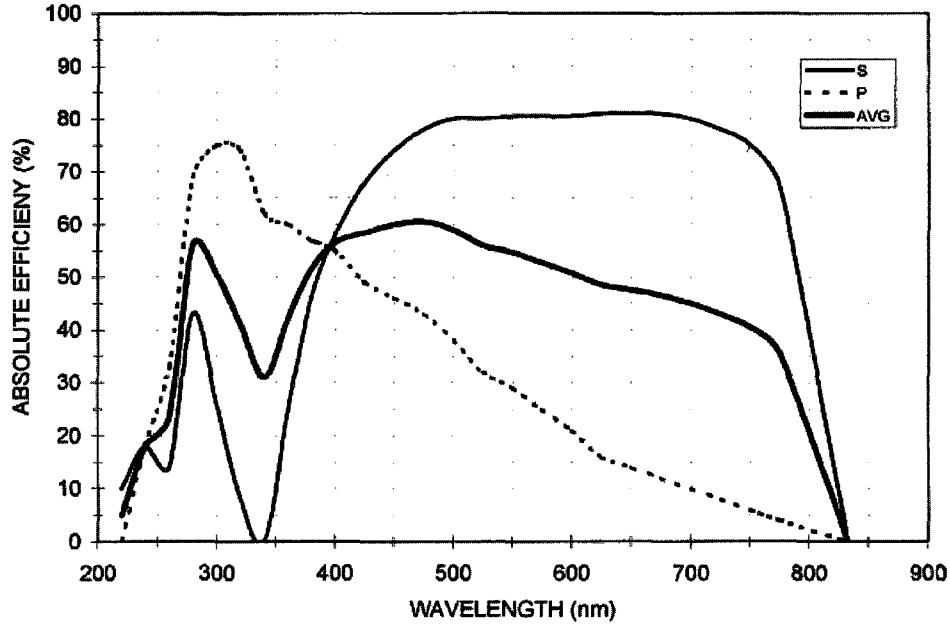

Figure 2.2. The efficiency with which the grating reflects power into the first order reflection as a function of wavelength and light polarization. The absolute efficiency is defined as the power reflected into the m^{th} order reflection divided by the power of the incident light. In the graph, the line labels "S" to refers polarization of the electric field vector perpendicular to the grating's grooves. The line labeled "P" refers to the electric field vector polarization oriented parallel to the grooves. Graph supplied by Edmunds Optics.

Using this method, we were able to reduce the spectral line width by an order of magnitude to ≈0.3 nm. With one atmosphere of gas, the Rb line width is ≈ 0.04 nm. These widths allow for enough overlap to provide substantial optical pumping rates, up to 10^5/sec.[2]

Polarizer 1 employed a permanently attached Ocean Optics Spectrometer to monitor the line width and spectral features of the beam. This was necessary due to the above mentioned instability of the temperature of the laser diodes' junctions due to changes in the ambient temperature. Changes in the water chiller temperature were made to optimize this line shape.

Polarizer 2 did not incorporate a dedicated spectrometer. Since the laser junction temperature could be controlled more finely, it was not necessary. However, the spectral line was checked periodically to check for long-term drift in the spectral characteristics.

We initially were concerned about heat dissipation from the grating in the cavity for the 100 W nLight laser employed in Polarizer 1. The gratings are not completely efficient, and some of the light is absorbed heating the grating. If the heating is too severe, the grating may stress and crack. An NT43-266 holographic grating produced by Edmund Optics was used for our polarizers employed a glass substrate. The glass is not particularly well suited to transport heat away from the grating, and this hindered the cooling methods we attempted to employ. Later, we learned that Edmund Optics quoted a damage threshold for this type of grating at 350 mJ/cm^2 for pulsed lasers and 40 W/cm^2 for CW lasers. Due to the expansion of beam and the angle of incidence, we estimated the beam intensity was at most 25 W/cm^2 and stopped attempting to actively cool the grating. We did not have similar concerns for the grating used with the 50 W QPC laser.[3]

2.3.1.3 Beam Shaping Optics and Optical Alignment

We must properly shape and collimate the beam after the laser has been spectrally narrowed. The laser beam must be well collimated so substantial light is not lost as the beam transverses the cell. However, the beam must also completely fill the volume of the cell, otherwise regions of very low polarized Rb will exist in the dark spots. DLA beams have a rectangular geometry, but we sought to produce a well-collimated 10 cm diameter circular beam. It is prohibitively difficult to transmute a rectangular beam

---

[2]This value was based on the numerical simulations reported in Chapter 4, not on actual measurements.

[3]In his thesis, Ruset describes testing two types of grating for use with his 300 W laser diode array stack. He concluded that for high power lasers one needs gratings with low modulation depth and a good thermally conductive substrate such as copper [11].

into a circular beam using simple optical techniques. Therefore, we compromised with a square beam geometry with 4.5 cm length sides. To convert the rectangular beam emitted by the LDA, we employed four cylindrical lenses to adjust the two laser axes separately. Selection of proper focal length lenses was aided by an educational ray tracing program, OSLO-EDU, and by calculating ray paths using refraction and transfer matrices.[4] The beam shaping optics took the form of two cylindrical lens telescopes with magnifications such that the fast and slow axes of the laser became equal after passing through the optics. The telescopes also served to reduce the divergence of the beam. The telescopes were positioned so that the focus of both telescopes was in the same location. A quarter wave plate positioned at the telescope's foci gave the necessary helicity to accomplish optical pumping.

Figure 2.3 shows an overhead view of the entire optical arrangement with dimensions in cm. Notice that in order to conserve space, we employ three mirrors to wrap the beam around the optics table. All the optics were carefully aligned to assure that they were centered on the beam axis. Removing an optic that had been placed and noting that the beam direction did not change served as a check of the alignment. The alignment could also be checked by reflecting the beam back along its path using the last mirror and noting that the image of the return beam overlapped the image of the out going beam. The latter method was particularly useful in aligning the last two mirrors.

The beam was directed through a 10.16 cm diameter hole in the optics table onto the polarizing cell. This final alignment was critical to guarantee that the beam illuminates the entire length of the cell. To accomplish this final alignment, we set up a plumb line centered about the hole in the optics table. The plumb line marked a position on the base of the polarizer that was directly below the center of the hole in the optics table. We then positioned the final mirror such that when the laser was on, the beam passed through the center of the hole and struck the position marked by the plumb line. The beam was then centered with respect to the hole in the optics table and plumb. Later, we centered the cell with respect to the hole using the same plumb line. We leveled the top of the cell and assumed that the sides of the cell were square with the top. Thus, after doing this, the optical pumping cell should have also been plumb and centered.[5]

---

[4] A good review of this method is found in Hecht's *Optics* [36].

[5] I should note that we later found out that the procedure I describe does not always work as well as it might seem it should. We discovered that it is desirable to adjust the beam direction after the optical pumping cell has been placed so that the beam appears centered on the top of the cell. You might worry that this introduces all sorts of unknowns and ruins the plumb of the beam path, but I found that it does not seem to be catastrophic and can actually help improve the performance of the polarizer. One might argue that one would do better to adjust the position of the optical pumping cell, and that may be correct. However, we have much finer control over the final mirror's orientation than we do over the cells

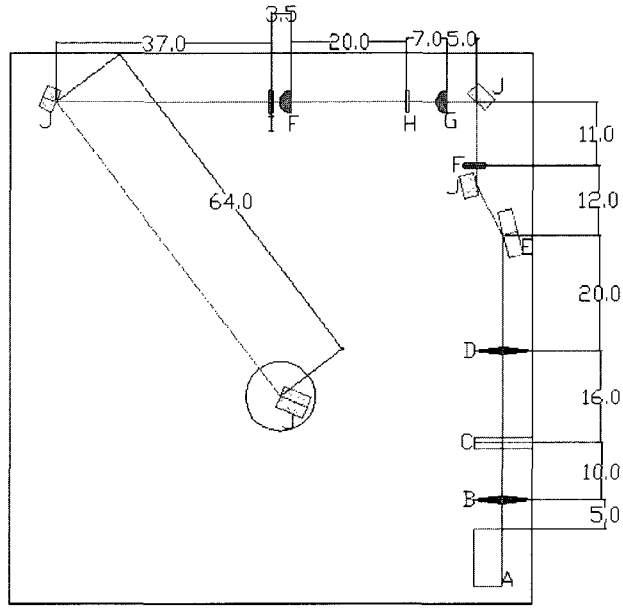

Figure 2.3. A diagram of the optics table for Polarizer 2. Polarizer 1's optical layout was similar. All dimension are given in centimeters. A: Laser Mount and Laser, B:55 mm Spherical Lens, C:$\frac{1}{2}$ – λ plate, D:200 mm Spherical Lens, E:Holographic Grating, F:250 mm Cylindrical Lens, G:40 mm Cylindrical Lens, H:$\frac{1}{4}$ – λ plate, I:200 mm Cylindrical Lens, J: Mirror. The red line represents the laser path. The final mirror in the optics train directs the light through a hole in the optics table onto the polarizing cell below.

2.3.2 The Optical Pumping Cell

The optical pumping cells used in both Utah Polarizers were substantially larger than those used in most other flow-through polarizers. Only the UNH optical pumping cells were larger, which measure ≈1.8 m tall [15]. In comparison, the Utah cells were nominally 1.2 m tall. The optical pumping cell consisted of three regions: the inlet tube, the Rb mixing region, and the optical pumping region (see Figure 2.4).

The inlet tube was a nominally 75 cm long, 3/4 in. diameter Pyrex® tube through which the gas mixture entered the cell. The tube was valved at the top to allow gas lines to be disconnected without contaminating the cell. Gas lines for the polarizers' gas handling system were attached to the cell using ChemThread compression fittings, which were easily dismantled for quick disconnect of the gas lines.

It takes only about 10 seconds for the gas to travel from the top of the inlet tube down to the bottom of the oven. This led to concern that the gas mixture was not thermally equilibrating with the oven before reaching the Rb mixing chamber. To test this, we

position. One can quickly reach the point of diminishing returns if one spends too much time adjusting the cell position. With that disclaimer, I think the procedure I describe above is a good starting place.

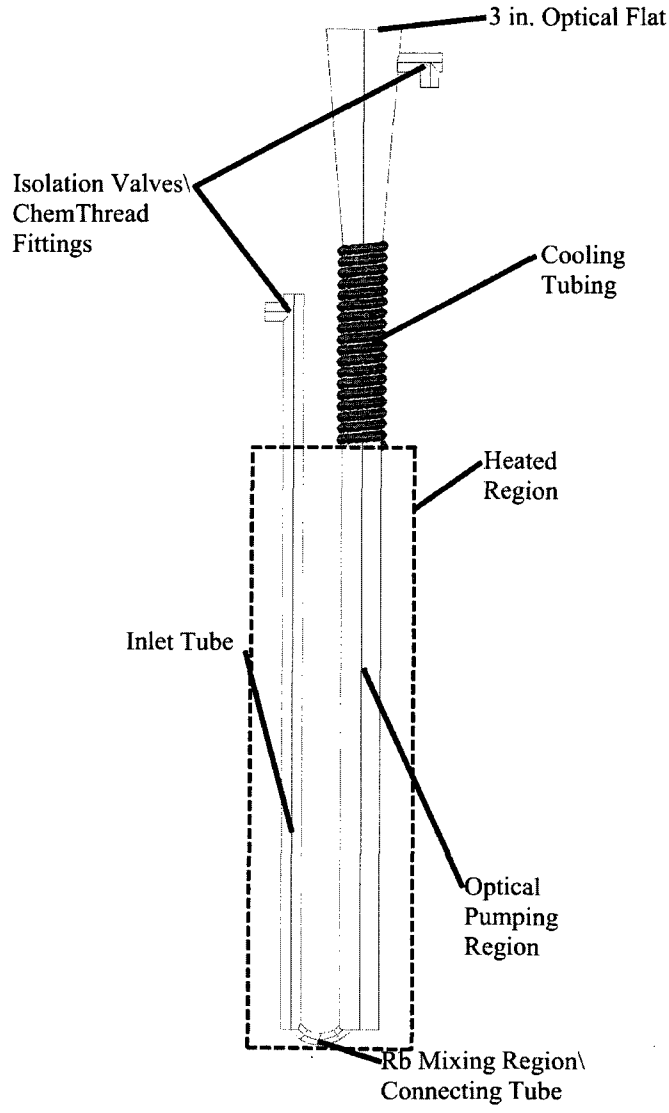

Figure 2.4. A diagram of the Optical Pumping Cell. In this diagram, the gas mixture entered on the left through the valve on the inlet tube. It traveled down into the heated region and through the connecting tube where it mixed with hot Rb vapor. Saturated with Rb vapor, the gas mixture traveled up through the optical pumping region during which time the ^{129}Xe was polarized. After leaving the heated region, the gas was quickly cooled by the cooling tubes surrounding the cell. The Rb vapor condensed on the walls of the cell at this point. The gas mixture exited the cell on the right through the valve connected to the tapered Section of the optical pumping region. In this diagram, the laser beam propagated down through the optical pumping region.

wrapped heat tape around the 1/2 in. and 1/4 in. soft copper tubing immediately before the inlet tube to preheat the gas mixture of Polarizer 1. The heat tape covered a linear distance of about 31 cm before the cell inlet and heated the gas such that it entered the optical pumping cell at 160 °C. We did not see an appreciable change in ^{129}Xe polarization and concluded this was not critical for the performance of the polarizer. This experiment was repeated on Polarizer 2, and similar results were found.

The Rb mixing region was in a connecting tube between the optical pumping region and the inlet tube. We inserted glass wool into this connecting tube and saturated it with one gram of Rb. The gas mixture passed over the glass wool and became saturated with Rb vapor. The original design of the cell had no method of keeping the glass wool in the connecting tube. The glass wool could become dislodged if high velocity gas mixtures hit it. To prevent this, later designs of the cell incorporated screens around the connecting tube to prevent the glass wool from either moving forward into the optical pumping region or back into the inlet tube.

Unlike Hersman's polarizer, our design did not include a long Rb saturation region with Rb pools and was omitted for several reasons. First, based on the experience of our group, such a long region was not necessary for complete Rb saturation. We believed that glass wool saturated with Rb would provide sufficient surface area for the the gas mixture to become fully saturated. Second, the inclusion of a spiraling glass Rb saturation region like Hersman's would have made it very difficult to conduct the Rb polarimetry experiments described in Chapter 3. However, it is possible that the Rb mixing region does not adequately saturate the gas mixture, and this could partially explain what appears to be depressed Rb number density as compared to our model's predictions (see Section 4.7 for more information).

In the optical pumping region, the laser light, Rb, and ^{129}Xe interacted to produced HP Xe. The region was constructed in two Sections. The lower Section is an 80 cm long, 45 mm OD medium wall thickness Pyrex® glass tube. The lower 50 cm of this tube were heated to temperatures above 120°C.

Immediately above the heated region, the glass is wrapped with plastic tubing through which chilled water flowed. In this region, the gas mixture quickly cooled and the Rb condensed on sidewalls of the cell. A thick layer of Rb could be observed trapped in this region. The chilled water in the cooling lines also cooled the laser, so the temperature of the water was set by the requirements of the laser. This was typically about ≈10 °C to ≈20 °C for Polarizer 1 and 17.5 °C for Polarizer 2.

The second Section of the optical pumping region consists of a 22 cm long tube that expands from the diameter of the lower region to nominally a 3 in. diameter.

This expansion was originally designed for two reasons. The first was because the UNH group observed that this geometry better accommodated laser beam geometry. The second reason was to aid in supporting the cell vertically. After construction, we found the former justification to be superfluous. The beam is well collimated enough that it did not considerably converge from the top of the optical pumping region. The latter justification may still be valid, but to better illuminate the optical pumping region, cells without an expanded region should be considered for future use. We do not, however, necessarily believe that the dark regions in the cell due to the expansion seriously effect the performance of the polarizer because the Rb number density should be low enough in this portion of the cell that it is no longer effectively contributing spin-exchange or destruction with ^{129}Xe.

A 3 in. optical flat was affixed to the top of the optical pumping region. This optical flat allowed the light to transmit through the cell without seriously changing the beam geometry. There was likely modest reflection off the optical flat because it was not coated with anti-reflective coating. Future designs may attempt to incorporate anti-reflective coating on this optical flat to facilitate light transmission.

The cells were carefully prepared in an attempt to assure that the interior surface is not a major source of relaxation for either the Rb or the Xe. A new cell was prepared by first rigorously rinsing the interior surface with deionized water, washing the surface with Piranha solution, and rerinsing the surface multiple times with deionized water. The cell was dried while dry nitrogen was flowing through it. After drying, the cell's interior was coated with SurfaSil^{TM}, made by Thermo Scientific, to reduce the wall's relaxation properties [37]. The cell was again dried under a dry nitrogen flow. At this point, the glass wool, also cleaned with Piranha solution and rinsed in deionized water, was introduced to the cell through a small tube, which was then flame sealed. Next, the Rb was distilled into the cell, also through a tube that was flame sealed. Then, the entire cell was evacuated and baked at $\approx$ 90 °C for several days. Finally, the cell could be back filled with nitrogen or left under vacuum until needed. A detailed procedure describing the preparation procedure can be found in Appendix C.

2.3.3 Heating System

A forced air oven heated the optical pumping cell. The heated air was split into four parts and delivered at different points along the oven to attempt to level temperature gradients. At a temperature of 130°C we measured a temperature difference of 6°C from the bottom of the to the top.

A temperature sensor attached to the interior side of the oven monitored the oven temperature and provided feedback for an Omega CNi16D22 PID controller to regulate

the oven temperature. The PID controller regulated the current to two 1 kW electric air heaters over which building air was forced. Generally, the controller regulated to within 0.5°C.

The Polarizer 1's oven was designed such that the hot air ports were both at different heights but also on different sides of the oven box. This design proved unnecessary and cumbersome. Polarizer 2's oven was redesigned with the hot air ports at different heights but only entered the oven on one side. This provided the same performance and easier access to the interior of the oven.

2.3.4 Gas Handling System

The flow-through polarizers must have some sort of gas handling system to properly mix the Xe and buffer gases and to transport the HP gas from the polarizer after polarization. Improper handling of the gas may result in a decrease in polarizer performance or contamination of the system. This next Section provides a detailed look at how Utah's polarizers handle the gas mixture both before the optical pumping cell and after. Figure 2.5 provides an overview of the gas handling system.

2.3.4.1 Pre-Polarization Manifold

We referred to the plumbing and gas handling system upstream of the optical pumping cell as the Pre-Polarization Manifold. In this manifold, the Xe and buffer gases were metered, mixed, and purified.

The gas mixture propagated through the system consisted of He, N_2, and Xe. The main constituent was He due to its relatively low Rb spin destruction rate [38] and usually accounts for $\approx$66% of the mixture. A modest amount of N_2 is added to nonradiatively relax the Rb and to reduce the lifetime of the Rb excited state [2, 11]. The mixture is very lean in Xe concentration, and for most experiments it accounts for less than 1% of the mixture.

For Polarizer 1, we used an Omega Gas Proportioning Rotometer Manifold (FL-5GP Series). Omega provided rotometer calibrations for common gases, but we found it necessary to recalibrate the rotometers. The pressure of the monitored gases was carefully regulated as the rotometer calibration depended upon it. The rotometers have a quoted accuracy of 2% full scale.

Polarizer 2 incorporated three AALborg GFC Model Mass Flow Controllers (models GFCS-011401, GFCS-010549, and SKUW-183460, AALBorg) to allow for independent control of the He, N_2, and Xe, respectively. These controllers had the advantage of providing a much more stable flow than the rotometer and are accurate over a wide range of pressures. The Mass Controllers have a quoted accuracy of 1.5% full scale.

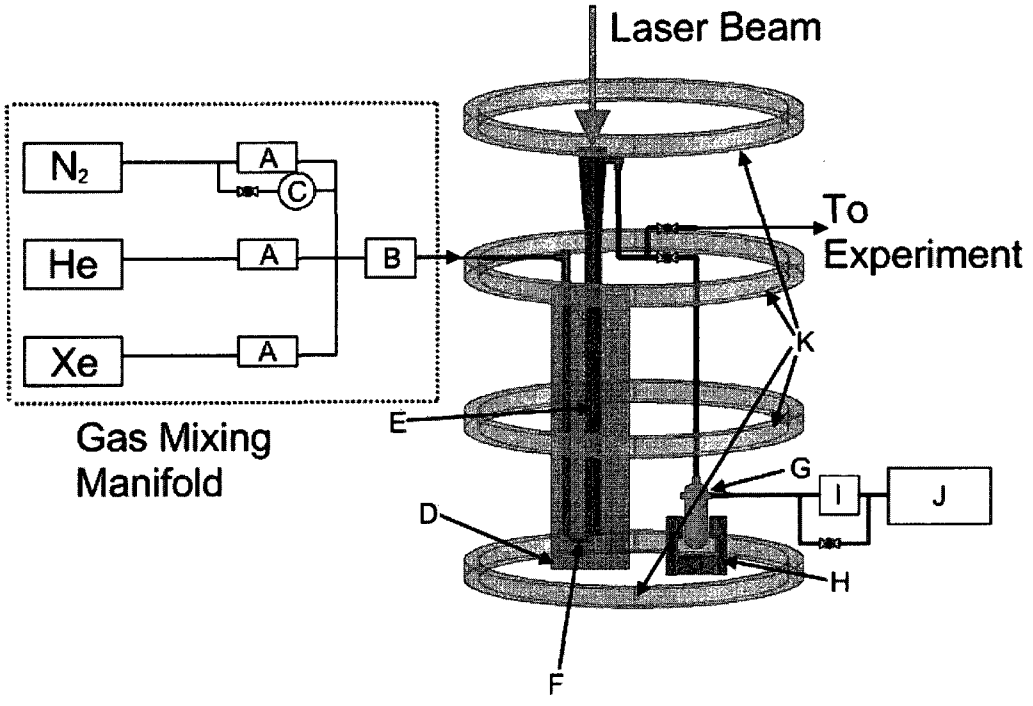

Figure 2.5. A diagram of the polarizer including plumbing and supporting equipment. The gas mixing manifold consists of the N_2, He, and Xe gas canisters, their respective gas flow controllers (A), and the gas purifier (B), which is specified to reduce impurities to <1 ppb. An emergency normally-open bypass solenoid (C) allows for continued N_2 flow through the system in case of a power outage. A forced-air oven (D) is used to heat the lower portion of the optical pumping cell (E) and vaporize the Rb in the Rb presaturation region (F). A custom cold finger (G) cryogenically separates and stores hyperpolarized Xe (see Figure 2.6). The storage magnetic field is provided by a 2000 G permanent magnet (H). A vacuum regulator (I) controls the pressure in the optical pumping cell from 0.3-1.2 bar, and is backed by a mechanical vacuum pump (J). Four 40 cm diam. coils (K) provide the 30 G applied magnetic field for optical pumping. All gas lines upstream of the cell are made with soft copper, brass, or stainless steel tubing. Gas lines downstream of the cell are either glass or PFA tubing.

Using either the Rotometer Manifold or the Mass Flow Controllers, we were able to custom blend the gases allowing exploration of different gas mixtures and different total flow rates.

After metering, the gas mixture passed through a SAES PureGas FaciliTorr FT400-902 purifier. The purifier reduced oxygen and hydrocarbon contaminants to < 1ppb, and it was rated to accept gas flows of up to 75 L/min. The typical total flow rates through the polarizer were 100-1900 sccm. The purifier also served as a chamber in which the constituent gases mixed.

We initially constructed the connecting tubes in the pre-polarization manifold of PFA tubing. However, we found this tubing would not seal well to the fittings and allowed excessive leaking. We replaced the PFA tubing with soft copper. The soft copper formed leak tight seals with compression fittings, but still had the advantage of being relatively flexible and easy to form.

To reduce the risk of contamination, it may be wise to replace the soft copper tubing with stainless steel tubing. However, it is not clear that this would significantly improve the polarizer's performance.

2.3.4.2 Post-Polarization Manifold

After polarization, the HP Xe may either be cryogenically separated from the gas mixture and stored for a later experiment or it may be directed to an experiment that requires a continuous flow of HP gas. A mode valve provided a simple mechanism to switch between the two different modes of operation. In "free-flow mode," the HP Xe flows to a continuous flow experiment. When attempting experiments of this type, care must be taken to assure that the pressure load presented by the experiment does not exceed the metered pressure of any of the gases or the pressure rating of the fittings in the polarizer. For the Utah polarizers, one should avoid pressures above 1.5 atm.

In "freeze-out mode," the gas flow is directed to a coldfinger for cryogenic separation. The freezing point of Xe is -111.9 °C [39], which is much higher than the other buffer gases. We constructed a coldfinger like that described by Driehuys et al. [40]. The coldfinger consisted of 1 cm ID inner tube through which the gas entered and traveled to the bottom of the coldfinger. This inner tube tapered to a narrow, 2 mm nozzle that served as a jet to propel the gas onto the coldfinger's cold outer tube surface. The outer tube was 15 cm long and 2 cm in diameter. The tube terminated in a 2 cm radius bowl. It was onto this bowl that the gas jet was propelled. A warming jacket surrounded the inner tube to prevent Xe from freezing in either the tube or nozzle. A constant supply of warm nitrogen flowed into the warming jacket. Figure 2.6 shows a crossSection of the coldfinger.

The exhaust tube of the coldfinger was attached to a Marsh Bellowfram 960-501-000 vacuum regulator backed by an Alcatel 2008A mechanical vane pump. This setup allowed us to regulate the pressure in the optical pumping cell below an atmosphere.

2.4 VOLoPXePol Performance

^{129}Xe polarimetry measurements were made by comparing ^{129}Xe NMR to protons in deionized water. A resistive 50 Ω NMR probe was used to measure both the ^{129}Xe and proton FIDs. The resistive probe sacrificed sensitivity for a flat frequency response. To avoid any frequency dependent systematic errors in the NMR spectrometer electronics

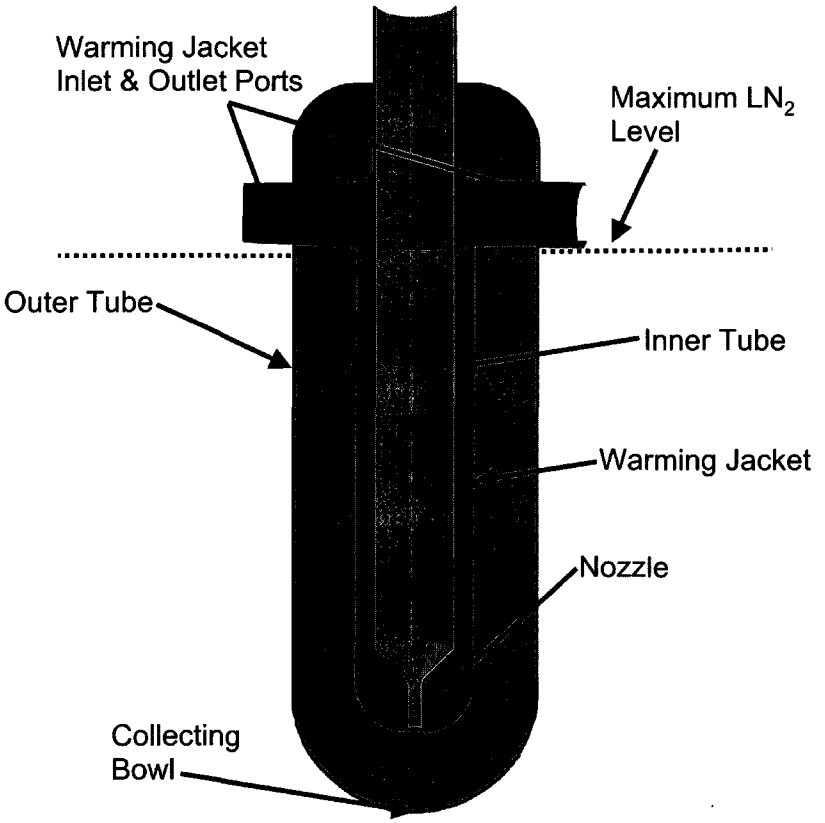

Figure 2.6. A cross-Section of the coldfinger used to cryogenically separate the Xe from the other gases. It is made of Pyrex^{TM} glass which easily handles the thermal gradients and shocks associated with immersion in liquid N_2. The hyperpolarized gas mixture travels from the inlet down through the inner tube, which is kept warm by circulating N_2 gas through the warming jacket. The nozzle propels the gas stream onto the cold surface of the collecting bowl. The rapid expansion of the gas also serves to cool it by Joule expansion. The Xe condenses on the surface while the other gases travel back up the coldfinger in the outer tube and out through the exhaust port (not shown). After a sufficient amount of Xe is accumulated, the vessel is evacuated and the Xe is revolatilized. A significant fraction of the polarization survives the freeze/thaw cycle.

the NMR frequency was chosen to be 10.7 MHz and the field was changed when probing Xe or protons to accommodate the different gyromagnetic ratios of ^{129}Xe and ^{1}H.

After polarization, the gas mixture was piped through a ≈10 m length of 1/2 in. PFA Teflon tubing to the NMR probe in a Varian electromagnet. We assured that depolarization in the connecting tubing was negligible by doubling the length of the connecting tube and noting no change in the measured polarization. For pressure dependent measurements, the gas mixture was routed back to the vacuum regulator on the polarizer after passing through the NMR probe.

We determined the ^{129}Xe polarization by deriving the following expression for ratio of ^{129}Xe and proton NMR signals. We first started with the ratio of the signals:

$$\frac{S_{\mathrm{Xe}}}{S_p} = \frac{\mathcal{P}_{\mathrm{Xe}}}{\mathcal{P}_p}\frac{N_{^{129}\mathrm{Xe}}}{N_p}\frac{\gamma_{\mathrm{Xe}}}{\gamma_p}\frac{\sin(\alpha_{\mathrm{Xe}})}{\sin(\alpha_p)}. \tag{2.5}$$

Here, S_G is the NMR signal from due to the ^{129}Xe or the protons, $\mathcal{P}_G$ is the polarization of the ^{129}Xe or proton nuclei, N_G is the number of ^{129}Xe or proton particles, γ_G is the gyromagnetic ratios and α_G is the flip angle used to tip the magnetization into the transverse plane. For our experiments, $\alpha_{\mathrm{Xe}} = \alpha_p \approx 90°$.

We can express the number of particles as follows. For ^{129}Xe, the ideal gas law tells us

$$N_{^{129}\mathrm{Xe}} = \frac{P_{^{129}\mathrm{Xe}}V}{kT}, \tag{2.6}$$

where $P_{^{129}\mathrm{Xe}}$ is the partial pressure of ^{129}Xe and is equal to the product of the fraction of ^{129}Xe and the total pressure of Xe, $\beta_{^{129}\mathrm{Xe}}P_{\mathrm{Xe}}$.

To determine the number of protons, we will first use the fact that the mass of the water used is given by density of water times the sample volume, $\rho_{\mathrm{H_2O}}V$. The number of water molecules is this mass divided by the molar mass of water times Avogadro's number, so now we have $\frac{\rho_{\mathrm{H_2O}}VN_a}{\mathcal{M}}$. Finally, there are two protons for every one water molecule; therefore, we multiply by 2 and obtain the following expression for the number of protons in the sample:

$$N_p = \frac{2\rho_{\mathrm{H_2O}}VN_A}{\mathcal{M}}. \tag{2.7}$$

Finally, we need to calculate an expression for the thermal polarization of the protons, $\mathcal{P}_p$. The thermal polarization of any material in a magnetic field can be shown to be [41]

$$\mathcal{P}_p = \tanh\left(\frac{\mu B}{kT}\right) \approx \frac{\mu B}{kT}, \tag{2.8}$$

where the approximation is valid in the limit of low polarization. For spin $\frac{1}{2}$ particles, $\mu = \frac{1}{2}\hbar\gamma$. By substituting into equation (2.8), we find

$$\mathcal{P}_p = \frac{\hbar\gamma B}{2kT} = \frac{hf}{2kT}, \tag{2.9}$$

where we have used $\gamma B = 2\pi f$.

Using equations (2.6), (2.7), and (2.9) with equation (2.5), we find

$$\frac{S_{\mathrm{Xe}}}{S_p} = \frac{\mathcal{P}_{\mathrm{Xe}}}{hf}\frac{\mathcal{M}P_{^{129}\mathrm{Xe}}}{\rho_{\mathrm{H_2O}}N_A}\frac{\gamma_{\mathrm{Xe}}}{\gamma_p}. \tag{2.10}$$

The tip angle ratio term has vanished because of the assumption of equal tip angles. Solving for $\mathcal{P}_{\mathrm{Xe}}$ and using the values in Table 2.2, we can write:

$$\mathcal{P}_{\mathrm{Xe}} = (7.949689 \times 10^{-11}\mathrm{J\cdot s\cdot cm^{-3}})\frac{f}{P_{^{129}\mathrm{Xe}}}\frac{S_{\mathrm{Xe}}}{S_p}. \tag{2.11}$$

In equation (2.11), the frequency, f, is expressed in Hz and the pressure, $P_{^{129}\mathrm{Xe}}$, is expressed in J·cm^{-3}. It is convenient to be able to express f in MHz and $P_{^{129}Xe}$ in atm. To convert f in equation (2.11), we multiply the front coefficient by $\frac{10^6\mathrm{Hz}}{\mathrm{MHz}}$. To express $P_{^{129}\mathrm{Xe}}$ in atm, we first multiply by $\frac{10^6\mathrm{cm}^3}{\mathrm{m}^3}$, which will allow us to express $P_{^{129}\mathrm{Xe}}$ in Pascal. Finally to convert to atm, we multiply the equation by $\frac{\mathrm{atm}}{101000\mathrm{Pa}}$. Using all this, we obtain the following expression:

$$\mathcal{P}_{\mathrm{Xe}} = (7.949689 \times 10^{-11}\mathrm{J\cdot s\cdot cm^{-3}})\frac{f}{P_{^{129}\mathrm{Xe}}}\frac{S_{\mathrm{Xe}}}{S_p}\frac{10^6\mathrm{Hz}}{\mathrm{MHz}}\frac{10^6\mathrm{cm}^3}{\mathrm{m}^3}\frac{\mathrm{atm}}{101000\mathrm{Pa}} \tag{2.12}$$

$$= \frac{(7.8457 \times 10^{-4}\mathrm{atm\cdot MHz^{-1}})f}{P_{^{129}\mathrm{Xe}}}\frac{S_{\mathrm{Xe}}}{S_p} \tag{2.13}$$

Unless it was the parameter under examination, the polarizers' data was taken under the following, standard operating conditions: total pressure → 0.83 atm, oven temperature → 140 °C, gas flows → He:N_2:Xe 1000:500:10 sccm.

2.4.1 Temperature Dependence

We measured the temperature dependence of the ^{129}Xe polarization output for both Polarizer 1 and Polarizer 2 (Figure 2.7). For this measurement the pressure and gas flow were held at standard operating conditions. Both polarizers exhibit a characteristic maximum ^{129}Xe polarization as a function of temperature. Polarizer 1's temperature maximum was higher than Polarizer 2's because Polarizer 1 employed a laser with twice the laser output power.

Table 2.2. Various important physical constants used in the derivation of the relationship between $\mathcal{P}_{\mathrm{Xe}}$ and the ratio of ^{129}Xe and proton NMR signals. These values were used to calculate the prefactor in equation (2.11).

Physical Constant	Value	Units
h	6.626×10^{-34}	J·s
ρ_{H_2O}	1	g·cm^{-3}
N_A	6.022×10^{23}	mol^{-1}
$\mathcal{M}$	18.01	g·mol^{-1}
γ_{Xe}	1.18604	kHz·G^{-1}
γ_p	4.2257	kHz·G^{-1}

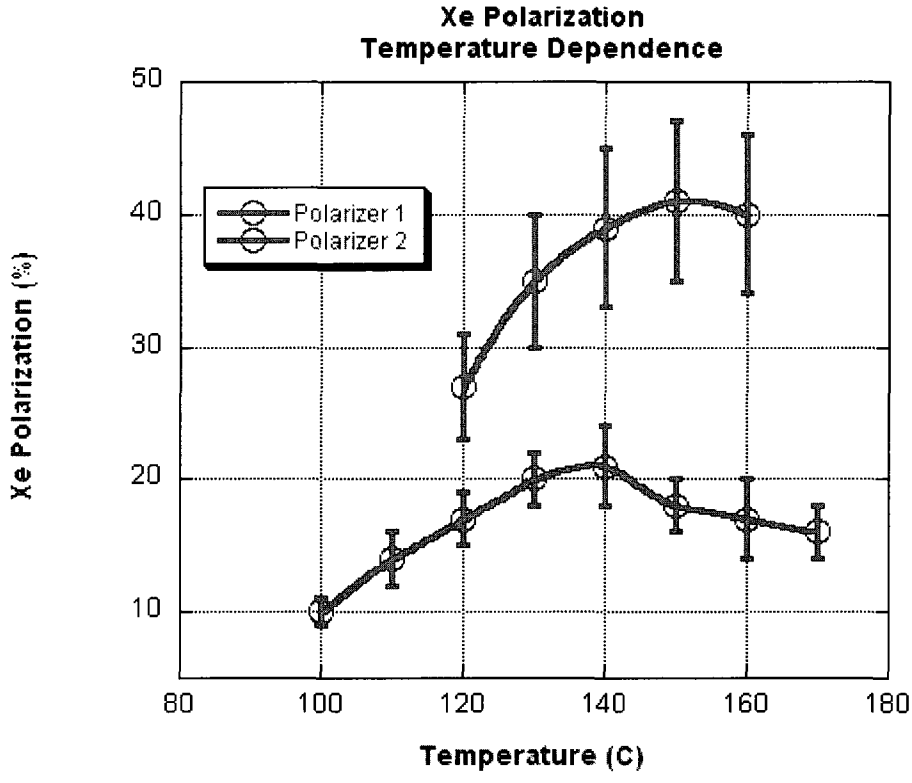

Figure 2.7. The temperature dependence of the ^{129}Xe polarization of both Polarizer 1 and Polarizer 2. Both polarizers have a maximum in the polarization temperature dependence. Polarizer 1's maximum occurred at a higher temperature than Polarizer 2's because the increased laser power available for Polarizer 1 enabled us to maintain high Rb polarization for higher [Rb].

The observed temperature maximum appears because of the competition of spin exchange rate and available light. The polarization of the ^{129}Xe will initially increase with rising temperature because the increase in the [Rb]. However, eventually the [Rb] will be high enough that one cannot maintain high polarizations of Rb with the available light, and the ^{129}Xe polarization will suffer as a result. Increasing the intensity of the incident light will move the temperature maximum to higher temperatures.

In addition, we believe that the rate of increase of the spin-exchange rate begins to slow at higher temperatures. This is due to an increase in the break-up rate of Rb-Xe van der Waals molecules. The importance of the temperature dependence of the spin-exchange rate was inferred in attempts to fit the data to numerical simulations. Section 4.4 contains more information on the form of the spin-exchange rate term used to evaluate the data.

2.4.2 Total Flow Rate Dependence

The output polarization of the ^{129}Xe depends on the total flow rate of the gas mixture through the optical pumping region. Adjusting the total flow of the gas changes the time the ^{129}Xe is in contact with highly polarized Rb. It also increases the time the gas spends in the relaxing environment of the cool portion of the optical pumping cell.

We observed a maximum in the total flow dependence when the oven temperature was held at both the standard operating temperature and at 130 °C. The maximum occurred at similar total flow rates (Figure 2.8). The difference in the magnitude of the ^{129}Xe polarization at the two different temperatures was likely due to the age of the optical pumping cell at the time the data were taken. The total flow data at 130 °C were taken at an early time in the optical pumping cell's life, and the 140 °C data were taken later. We have observed the apparent increase in relaxing mechanisms in older optical pumping cells, and believe that the aging of the cell caused this discrepancy.

The total flow maximum can be understood as a competition between resident time in the optical pumping region and ^{129}Xe spin destruction due to wall interactions in the unheated portion of the cell. Decreasing the flow rate will cause the ^{129}Xe to spend a longer time in the heated portion of the optical pumping cell, thus becoming closer to saturating its polarization. Continuing to decrease the total flow rate will result in the ^{129}Xe spending too much time in the unheated portion of the optical pumping cell resulting in depolarization due to interactions with the wall.

2.4.3 [Xe] Dependence

Decreasing the Xe partial pressure in the gas mixture can substantially increase the ^{129}Xe polarization. We measured the Xe partial pressure dependence of the output polarization in both polarizers (see Figure 2.9). Polarizer 1, again, showed large ^{129}Xe

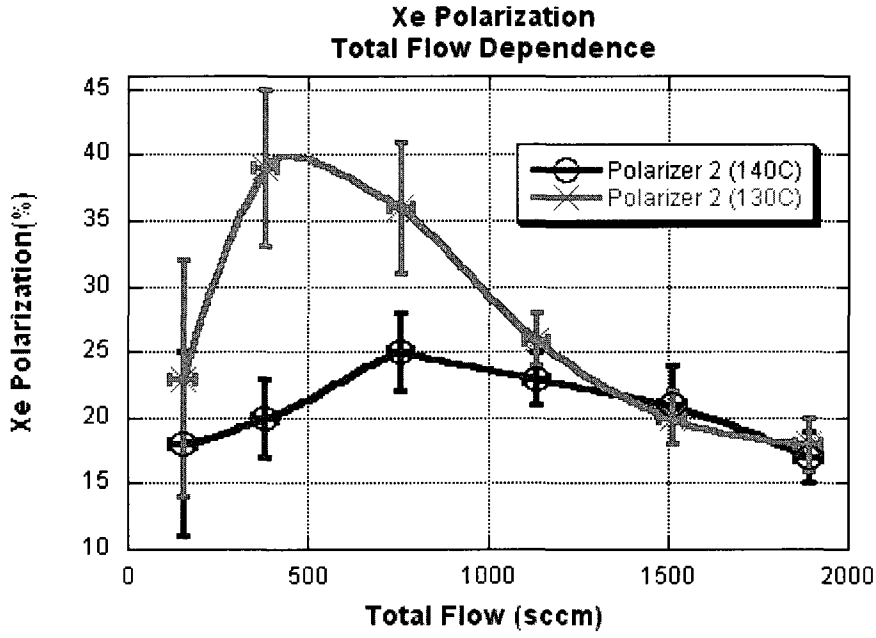

Figure 2.8. The total flow rate dependence of the ^{129}Xe polarization of Polarizer 2. The rotometers employed in Polarizer 1 made it challenging to accurately measure its total flow rate dependence. We made three measurements total flow measurements with Polarizer 1 (not shown) that seemed to indicate a similar dependence.

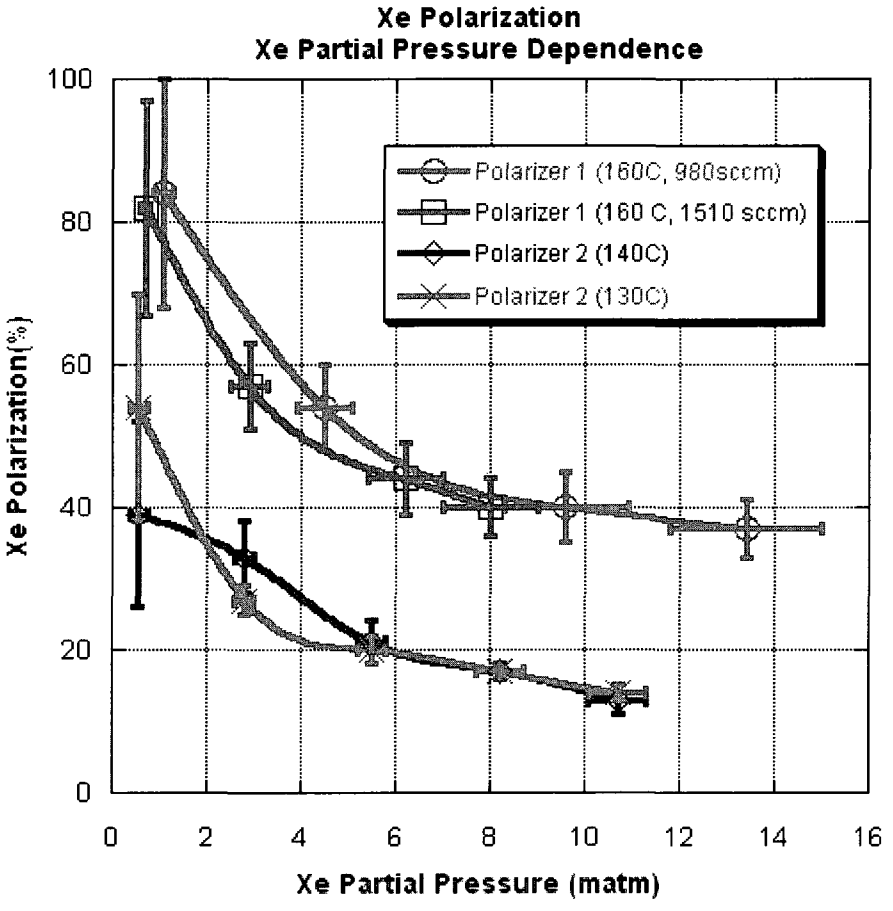

Figure 2.9. The Xe partial pressure dependence of the ^{129}Xe polarization of both Polarizer 1 and Polarizer 2. The Xe partial pressure was measured under a number of different conditions in both polarizers. Polarizer 1's measurements were made at 160 °C at two total flow rates: 980 sccm and 1510 sccm. The pressure was held at the standard operating pressure of 0.83 atm. Polarizer 2's measurements were made at the standard operating pressure and total flow, but the two temperature were used: 130 °C and 140 °C.

polarizations due to the greater laser power. The highest polarization, 84 ± 16% , was recorded in Polarizer 1 at a Xe partial pressure of 1.1 ± 0.2 mbar.

We varied the Xe partial pressure by decreasing the Xe flow rate. The flow rates of the buffer gases were not changed. Technically, the total flow rate of the gas mixture changed. However, the flow rate contribution due to the Xe was small enough that the change in total flow rate was less than 1%, and the composition change due to this change in flow rate should not significantly alter the results.

The large error bars on the ^{129}Xe polarization for very low Xe partial pressure were due to systematic errors in the metering of the Xe flow rate. The accuracy of the mass flow controllers on Polarizer 2 were only guaranteed to 1.5% full scale, and the rotometers on Polarizer 1 had a similar constraint. The flow rate of the Xe, and thus the Xe partial pressure, was not well known for very low Xe partial pressures, and this error propagated strongly in the ^{129}Xe polarization calculations.

The Xe partial pressure dependences can be understood by Rb-Xe spin destruction mechanisms. Xe has a large cross Section for Rb spin destruction. By increasing the Xe pressure, either by increasing the total pressure of the gas mixture or increasing the concentration of Xe in the mixture, one increases the Rb-Xe spin destruction rate causing the Rb polarization to suffer. This, in turn, decreases the ^{129}Xe polarization.

2.4.4 Pressure Dependence

The ^{129}Xe polarization does not depend strongly on the total pressure of the gas in the optical pumping region in the pressure regime we probed. We varied the total gas pressure by a factor of four, from ≈0.3 atm to ≈1.2 atm and observed very little change in the ^{129}Xe polarization (see Figure 2.10). Perhaps, there is a slight decrease in polarization at the highest pressure, but the experimental error associated with the point precludes making a definite statement. The numerical model presented in Chapter 4 does seem to indicate a very slight pressure dependence (see Section 4.7 for more details).

The total pressure dependence can be understood by the dependence of the Xe spin-exchange rate as a function of pressure. The molecular portion of the Xe spin-exchange rate is dependent on the lifetime of the Xe-Rb complexes. These complexes are formed and destroyed in three body interactions. At higher pressures, the number of collision per unit time increase, and this results in an increase in both the formation and break-up rates. The net result is an overall decrease in the mean lifetime of the molecules. The spin-exchange rate due to the molecular piece scale as the square of the lifetime of the molecule; so at higher pressures, the spin-exchange rate due to the molecular mechanism decreases.

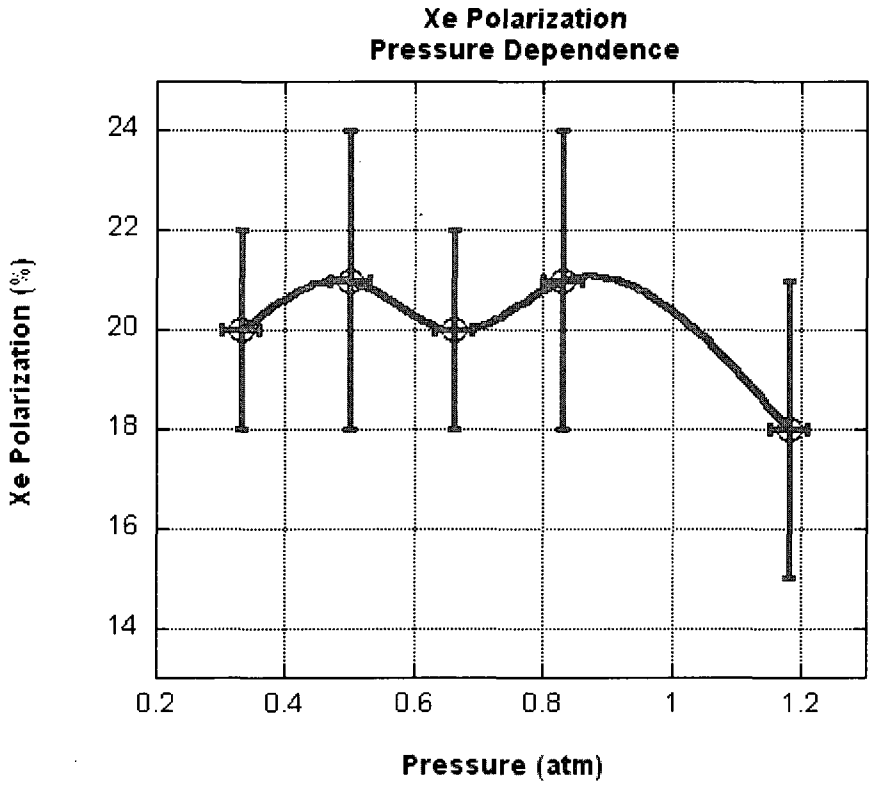

Figure 2.10. The total pressure dependence of the ^{129}Xe polarization in Polarizer 2. The measurement was taken with all the other parameters held at the standard operating conditions.

The total pressure dependence is further complicated by effects from pressure broadening of the Rb absorption line width and the pressure dependences of the Rb-Xe relaxation rate. By decreasing the total pressure, the Rb absorption line width also decrease. Thus, it is more difficult to effectively optically pump the Rb. Decreasing the pressure also results in an enhancement of the molecular component of the Xe-Rb spin-exchange rate, as this component is inversely proportional to the total pressure. However, Xe has a large cross Section for Rb spin destruction. By decreasing the total pressure, and thus the Xe partial pressure, one decreases the Xe-Rb spin destruction rate causing the Rb polarization to increase. This, in turn, increases the ^{129}Xe polarization.

Addition of all of these effects may explain the flattening of the ^{129}Xe polarization at lower pressures. Some of our simulations showed a very slight maximum in the pressure dependence, which could be interpreted as the result of the competition between the narrowing Rb line-width and changes in both the Xe-Rb spin destruction rate and the Xe spin-exchange rate.

2.5 Conclusion

I have presented two new ^{129}Xe flow-through polarizers and discussed their behavior under changes in various parameters. The behavior of the systems qualitatively agrees with our understanding of the underlying physics. In Chapter 4, we shall see that the behavior is in fair agreement with our numerical model of the system. However, there are discrepancies that point to inadequacies in our understanding.

CHAPTER 3

RUBIDIUM POLARIMETRY

3.1 Introduction

It is useful to have an understanding of the Rb polarization as a function of position in the cell. This information serves to test the validity of the model presented in Chapter 4, and it allows one to diagnose and evaluate the performance of the polarizer.

Rb polarization imaging was first presented by Will Happer's group in 1998 [42] using Optically Detected Electron Paramagnetic Resonance (ODEPR). They did this by exploiting the Rb electron transition selection rule to probe the hyperfine level populations. From the spectrum of hyperfine transition, they were able to calculate a Rb polarization. The group was also able to create a one-dimensional image of the polarization by applying gradient fields, but this feature was not used in the present work. The experimental setup that Happer presented allows one to simultaneously perform SEOP while measuring the Rb polarization. The full theory of Rb ODEPR will be further explained in the following section.

A complete description of the experimental setup is presented in Section 3.2, but an introduction to the experiment will be given here. It may be useful to refer to Figure 3.3 during this introduction. During the experiment, the optical pumping cell sits in a main magnetic field produced by the surrounding magnetic field coils. A pump beam of circularly polarized light, tuned to the appropriate D_1 transition frequency for Rb, propagates longitudinally to the main magnetic field through the sample. Transverse to the field, a less powerful probe beam propagates through the sample. The probe beam is also circularly polarized and tuned near the D_1 absorption wavelength. Helmholtz coils mounted perpendicularly to the axis of the field coils provide a Continuous Wave Radio Frequency (CW RF) field oscillating at frequency ω that will drive hyperfine transitions.

One may sweep the main magnetic field to bring various hyperfine transitions onto resonance with the applied RF field. On resonance, the atoms undergo transitions between the hyperfine sublevels (Table 3.1) during which the expectation value of the transverse spin, and thus the transverse magnetization, is nonzero. The RF power is kept weak so that the majority of Rb atomic magnetization lies longitudinally to the field. However, the

Table 3.1. The hyperfine energy levels of a ^{85}Rb atom and the associated nuclear/electronic spin wave functions. Optical pumping results in high populations in the $F = 3, m_f = -3$ sublevel. For many optical pumping situations of practical interest, the population distribution in these sublevels is described by a spin temperature (Section 3.1.1.2.)

	m_f	
$\mid \frac{5}{2}, \uparrow\rangle$	+3	
$\sqrt{\frac{5}{6}} \mid \frac{3}{2}, \uparrow\rangle + \sqrt{\frac{1}{6}} \mid \frac{5}{2}, \downarrow\rangle$	+2	
$\sqrt{\frac{2}{3}} \mid \frac{1}{2}, \uparrow\rangle + \sqrt{\frac{1}{3}} \mid \frac{3}{2}, \downarrow\rangle$	+1	
$\sqrt{\frac{1}{2}} \mid -\frac{1}{2}, \uparrow\rangle + \sqrt{\frac{1}{2}} \mid \frac{1}{2}, \downarrow\rangle$	0	$F = 3$
$\sqrt{\frac{1}{3}} \mid -\frac{3}{2}, \uparrow\rangle + \sqrt{\frac{2}{3}} \mid -\frac{1}{2}, \downarrow\rangle$	-1	
$\sqrt{\frac{1}{6}} \mid -\frac{5}{2}, \uparrow\rangle + \sqrt{\frac{5}{6}} \mid -\frac{3}{2}, \downarrow\rangle$	-2	
$\mid -\frac{5}{2}, \downarrow\rangle$	-3	

$\sqrt{\frac{1}{6}} \mid -\frac{3}{2}, \downarrow\rangle - \sqrt{\frac{5}{6}} \mid -\frac{5}{2}, \uparrow\rangle$	-2	
$\sqrt{\frac{1}{3}} \mid -\frac{1}{2}, \downarrow\rangle - \sqrt{\frac{2}{3}} \mid -\frac{3}{2}, \uparrow\rangle$	-1	
$\sqrt{\frac{1}{2}} \mid \frac{1}{2}, \downarrow\rangle - \sqrt{\frac{1}{2}} \mid -\frac{1}{2}, \uparrow\rangle$	0	$F = 2$
$\sqrt{\frac{2}{3}} \mid \frac{3}{2}, \downarrow\rangle - \sqrt{\frac{1}{3}} \mid \frac{1}{2}, \uparrow\rangle$	+1	
$\sqrt{\frac{5}{6}} \mid \frac{5}{2}, \downarrow\rangle - \sqrt{\frac{1}{6}} \mid \frac{3}{2}, \uparrow\rangle$	+2	

RF field does establish a small, transverse component oscillating at the Lamor frequency, which is also ω.

The probe beam intensity will attenuate as it passes through the Rb due to absorption by the vapor. The intensity, I as a function of path length, x through the sample is given by[42]

$$\frac{\partial I}{\partial x} = -\kappa \left(1 - 2 s_n \left\langle S_x \right\rangle\right) I. \tag{3.1}$$

In the above equation, $\kappa = [Rb]\,\sigma$, where $[Rb]$ is the number density of the Rb and σ is the absorption cross section per unpolarized Rb atom. The quantity s_n is the mean photon spin of the probe beam, ranging between 1 and -1, and the quantity $\langle S_x \rangle$ is the expectation value Rb electron spin along the direction of probe beam propagation. $\langle S_x \rangle$ is, as previously mentioned, oscillating at frequency ω, and this oscillation modulates the transmitted light intensity at the same frequency. Using a photodetector, one can detect the transmitted intensity and then demodulate the signal using a lock-in amplifier.

As one sweeps the main field, different hyperfine transitions will be brought onto resonance, and one obtains a spectrum as in Figure 3.1. Signal amplitudes are proportional to the electron spin polarization of the Rb, and one can calculate an absolute polarization by comparing the area ratios of different hyperfine peaks.

3.1.1 Theory of Optically Detected Rb EPR

The theory of the interaction of optically pumped alkali metals with an RF field was developed by Happer et al. [43, 42]. We will not consider the case of applying a magnetic imaging gradient, as Happer did. Thus, we are only interested in average polarization of the Rb across a sample rather than the Rb polarization profile along the probe beam.[1]

3.1.1.1 Liouville Space

It is useful to present the relevant theory of Rb atomic spin interaction with an RF field using the Liouville picture. The Liouville picture may be unfamiliar to some readers. This section will attempt to present a summary of the mathematical formalism involved in working in this picture.

The reader should be familiar with a Hilbert space from elementary quantum mechanics. Hilbert spaces are vector spaces spanned by normalized basis vectors that are typically labeled $\mid a\rangle$. In quantum mechanics, these vectors represent states of the system and are usually eigenvectors of an operator for the system. These vectors are generally one (or perhaps two) particle states.

---

[1] We are, however, interested in the Rb polarization profile along the long axis of the cell. This information does not require the use of magnetic field gradients

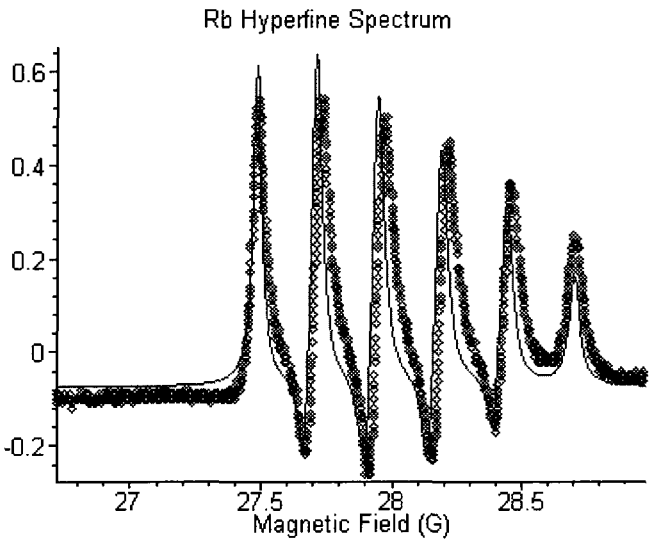

Figure 3.1. A sample of ^{85}Rb hyperfine spectrum detected using ODEPR with an approximate fit to the data. The data points are detected ^{85}Rb electron resonance lines, and the curve represents an approximate fit using the known form for ideal ^{85}Rb line shapes. The simulation assumes an RF field frequency of 13.1 MHz. As the field is swept, different hyperfine transition (all obeying the selection rule $\Delta m = 1$) are brought onto resonance. For the above data, ^{85}Rb atoms in the F=3 state are resonant 180° out of phase with the atoms in the F=2 state. This, however, is only true for the case when the probe beam and the axis of the RF coils are parallel. For our measurements used to determine the polarization, the probe beam and the axis of the RF coils were perpendicular resulting in all the hyperfine absorption peaks having the same phase.

To describe a multiparticle system with different populations described by different state vectors, a so-called mixed ensemble, one introduces the density operator ρ. This and a related object, the density matrix, contain information on all possible states of the system and the occupation of those states for a given mixed ensemble. The density operator is defined as follows:[1]

$$\rho \equiv \sum_i w_i \mid \alpha^{(i)}\rangle\langle\alpha^{(i)} \mid \tag{3.2}$$

The w_i's are the fractional populations in the states $\mid \alpha^{(i)}\rangle$ that are, in general, linear combinations of the basis vectors. The density operator elements form the density matrix:

$$\langle a \mid \rho \mid b\rangle \equiv \sum_i w_i \langle a \mid \alpha^{(i)}\rangle\langle\alpha^{(i)} \mid b\rangle. \tag{3.3}$$

The diagonal element $\langle a \mid \rho \mid a\rangle$ represents the normalized population of state $\mid a\rangle$. The off-diagonal element $\langle a \mid \rho \mid b\rangle$, where $a \neq b$, represents superpositions of the states $\mid a\rangle$ and $\mid b\rangle$. The quantum state that this matrix element describes, $\mid \alpha(t)\rangle = c_a(t) \mid a\rangle + c_b(t) \mid b\rangle$, are states where the phase difference between the states are constant in time.

These states are termed coherent superpositions, and thus, the off-diagonal elements of the density matrix are usually said to represent quantum coherences [44].

In the Liouville space formalism, we wish to manipulate the density operator rather than the state vectors. Liouville space is a super-space of the Hilbert space, which means the Liouville space is constructed from the elements of the Hilbert space. In particular, we can construct a basis of the form $\mid a\rangle\langle b \mid$. With this basis in mind, we can construct the density operator as follows:

$$\mid \rho) = \sum \rho_{ab} \mid ab) \tag{3.4}$$

where we have introduced the notation $\mid ab) = \mid a\rangle\langle b \mid$ and $\rho_{ab} = \langle a \mid \rho \mid b\rangle$. Notice that we have written the density operator in a notation similar to that of the state vectors for Hilbert space. This is to emphasize that operators are now the objects that we will be interested in manipulating.

We will define two new operations in Liouville space. The first is an inner product between two operators.

$$(A \mid B) \equiv \mathrm{Tr}\{A^\dagger B\} \tag{3.5}$$

That is, the inner product in Liouville space is simply the trace of the product of the two operators. The second operation we wish to define is the Liouville superoperator, $\hat{\mathcal{L}}$:

$$\hat{\mathcal{L}} \mid \rho) \equiv [\mathcal{H}, \rho] = \mathcal{H}\rho - \rho\mathcal{H}. \tag{3.6}$$

Physically meaningful $\mid \rho)$'s satisfies the Liouville equation:

$$\frac{\partial}{\partial t} \mid \rho) = \frac{-i}{\hbar}\hat{\mathcal{L}} \mid \rho). \tag{3.7}$$

This should be compared with the Schrödinger equation for physically meaningful state vectors $\mid \alpha\rangle$:

$$\frac{\partial}{\partial t} \mid \alpha\rangle = \frac{-i}{\hbar}\mathcal{H} \mid \alpha\rangle. \tag{3.8}$$

It is important to be able to calculate expectation values in Liouville space so that one can compute physically meaningful quantities. In the Liouville formalism, an expectation value of a Hilbert space operator Q is

$$\langle Q\rangle = \mathrm{Tr}\{Q\rho\} = (Q^\dagger \mid \rho) = (\rho \mid Q), \tag{3.9}$$

were have used the fact that $\rho = \rho^\dagger$ in the last equality. Thus, expectation values are just inner products of Hilbert space operators and the density matrix.

Finally, it is important to be able to calculate matrix elements of superoperators, such as the Liouville superoperator. That is, we would like an analogy between superoperators in Liouville space and operators in Hilbert space. We have defined the Liouville

superoperator in equation (3.6). We can generalize that definition to any superoperator by

$$\hat{Q} \mid Q_j) = \mid [Q, Q_j]) \tag{3.10}$$

and

$$(Q_j \mid \hat{Q} = ([Q^\dagger, Q_j] \mid, \tag{3.11}$$

where $\hat{Q}$ is a superoperator acting on the operator Q. It follows from definition (3.5) that the matrix elements of a superoperator are given by

$$(Q_1 \mid \hat{Q} \mid Q_2) = \mathrm{Tr}\{Q_1^\dagger [Q, Q_2]\} = \mathrm{Tr}\{Q_1^\dagger Q Q_2\} - \mathrm{Tr}\{Q_2 Q Q_1^\dagger\}. \tag{3.12}$$

The above discussion places the necessary framework of Liouville space. There exist, of course, a host of conventions, solution techniques, and nuance for which books have been written. There are a few books I have found useful to gain further understanding in the Liouville formalism. Schuller has written a short treatise on Liouville formalism in atomic spectroscopy, which contains a nice introduction to the subject with several examples in of its use in atomic physics [45]. Mehring and Weberruß have written a book on computational methods in magnetic resonance that uses both Hilbert and Liouville formalisms [44]. Finally, Appelt et al. also give a brief description of Liouville space and its use in describing optical pumping [43].

3.1.1.2 Spin Temperature and Polarization

The interpretation of the ODEPR spectra obtained in this experiment is simplified if the Rb density matrix is described by a spin-temperature. If this is the case, then we can write:

$$\rho = \mathrm{e}^{\beta F_z} \tag{3.13}$$

$$= \mathrm{e}^{\beta I_z} \mathrm{e}^{\beta S_z}, \tag{3.14}$$

where β is the spin temperature parameter.

Due to the nonthermal equilibrium of optical pumping situations, we are not guaranteed a spin temperature. However, there are several situations when a spin temperature distribution is theoretically expected. First, if alkali-alkali spin-exchange is the most rapid process, it can be shown that entropy is maximized for a spin temperature distribution [46]. However, Appelt et al. [43] showed that a spin temperature distribution prevails under more general conditions. They showed a spin temperature exists if all the interaction with the Rb atoms are sudden with respect to the nuclear polarization.

Sudden processes affect only the electron spin because they are of such short duration that the nuclear spin polarization only changes after the collision, when the nucleus and

electron recouple via the hyperfine interaction. Conversely, slow processes are of such extent that they can effect both nuclear and electron spins. Another way to state the difference is sudden processes are short enough that $\Delta F = 0, \pm 1$ transitions occur and slow processes only allow $\Delta F = 0$ transitions.

Appelt et al. [43] derived the following expression for the time dependence of ρ:

$$\begin{aligned}\frac{\partial \rho}{\partial t} = D\nabla^2\rho + \frac{1}{i\hbar}\left[\mathcal{H}_g', \rho\right] + \sum_j \frac{1}{T_{ex,ij}}\left[\varphi\left(1 + 4\langle \mathbf{S}_j\rangle \cdot \mathbf{S}\right) - \rho\right] + \frac{1}{T_{SD}}\left[\varphi - \rho\right] \\ + R\left[\varphi\left(1 + 2\mathbf{s}\cdot\mathbf{S}\right) - \rho\right] + \frac{4}{T_{SE}}\langle \mathbf{K}\rangle \cdot \mathbf{S}\varphi + \frac{1}{[I]^2 T_{FD}}[\mathbf{F}\cdot\mathbf{F} - \mathbf{F}\cdot\mathbf{F}\rho] \\ + \frac{1}{[I]^2 T_{FE}} \times \langle \mathbf{K}\rangle \cdot (\{\mathbf{F}, \rho\} - 2i\mathbf{F}\times\rho\mathbf{F}).\end{aligned} \tag{3.15}$$

Here, $D\nabla^2\rho$ describes effects due to diffusion of the vapor, $\mathcal{H}_g'$ is the Hamiltonian describing the atom in the absence of external interactions, the $\frac{1}{T_{ex,ij}}$ describes the spin-exchange of the alkali isotope i with isotope j, the $\frac{1}{T_{SD}}$ term describes sudden relaxation interactions (also called S-damping), the $\frac{4}{T_{SE}}$ term describes the sudden spin-exchange with noble gas nuclei $\langle K\rangle$ (also called S-exchange), the $\frac{1}{[I]^2 T_{FD}}$ term describes slow relaxation interactions (also called F-damping), and the $\frac{1}{[I]^2 T_{FE}}$ term describes slow spin-exchange with noble gas nuclei (also called F-exchange). Appelt et al. rewrote equation (3.15) as

$$\begin{aligned}\frac{\partial \rho}{\partial t} = D\nabla^2\rho + \frac{1}{i\hbar}\left[\mathcal{H}_g', \rho\right] + R'(S_z\rho S_z - \frac{3}{4}\rho + \frac{1}{2}[S_+\rho S_- + S_-\rho S_+]) \\ + R's_z'(\frac{1}{2}\{S_z, \rho\} + \frac{1}{2}[S_+\rho S_- - S_-\rho S_+]) + \frac{1}{T_{ex,ii}}[\langle S_+\rangle(\frac{1}{2}\{S_-, \rho\} + S_-\rho S_z - S_z\rho S_-) \\ + \langle S_-\rangle(\frac{1}{2}\{S_+, \rho\} + S_+\rho S_z - S_z\rho S_+)] + \frac{1}{[I]^2 T_{FD}}(F_z\rho F_z - \mathbf{F}\cdot\mathbf{F}\rho + \frac{1}{2}[F_+\rho F_- - F_-\rho F_+]) \\ + \frac{2\langle K_z\rangle}{[I]^2 T_{FE}}(\frac{1}{2}\{F_z, \rho\} + \frac{1}{2}[F_+\rho F_- - F_-\rho F_+]).\end{aligned} \tag{3.16}$$

Here, they defined the effective pumping rate as

$$R' = \frac{1}{T_{ex}} + \frac{1}{T_{SD}} + R \tag{3.17}$$

and the effective photon spin by

$$R's_z' = \sum \frac{2\langle S_{jz}\rangle}{T_{ex,ij}} + \frac{2\langle K_z\rangle}{T_{SE}} + Rs_z. \tag{3.18}$$

In equation (3.17), electron-electron spin-exchange rate with all isotopes is

$$\frac{1}{T_{ex}} = \sum_j \frac{1}{T_{ex,ij}}. \tag{3.19}$$

If one neglects all terms except those proportional to R' in equation (3.16) and solves the equation in the steady state condition (set $\frac{\partial \rho}{\partial t} = 0$), then the solution is the spin temperature distribution of equations (3.13) and (3.14).

Physically, the requirement of dominant sudden interactions can be understood by appreciating the selection rule allowed by sudden interactions, $\Delta F = 0, \pm 1$. If this rule holds, then the hyperfine sublevels are free to mix and we have a single population. Statistical mechanics tells us that if the total number of particles is conserved ($\sum N_i = N$) and the total spin angular momentum is conserved ($\sum N_i (F_z)_i = N\langle Fz \rangle$), then the distribution of the population, the N_i's, are given by a Boltzman factor. However, if we look at the other extreme, when the interactions are dominated by slow processes, then $\Delta F = 0$ and the hyperfine levels do not mix. If this is the case, the hyperfine levels are two separate populations and will establish a spin temperature individually. That is

$$\rho = \frac{e^{F_z^a \beta_a}}{Z_a} + \frac{e^{F_z^b \beta_b}}{Z_b}, \tag{3.20}$$

where F_z^a and F_z^b are the total angular momentum operators that act only on the $I - \frac{1}{2}$ and $I + \frac{1}{2}$ hyperfine levels, respectively, and the β's are the respective spin temperature parameters. In general, β_a and β_b need not be the same. However, even if they are the same, the spin system will not be defined by a spin temperature in the sense that it will not fulfill equation (3.13). (I should like to note, starting with this instance, we will use the convention that $a = I + \frac{1}{2}$ and $b = I - \frac{1}{2}$.)

For example, consider the case when the hyperfine sublevels of a ^{85}Rb population are described by $\beta_a = \beta_b = \infty$ after optical pumping. Assume that the populations of the hyperfine sublevels were equal before optical pumping began, that is, $\beta_a = \beta_b = 0$. If slow processes dominated, then the hyperfine sublevel populations are still equal after the optical pumping has driven β_a and β_b to infinity. The distribution will result in the level $F = 3, m_z = -3$ and $F = 2, m_z = -2$ being equally populated, which is not a spin temperature. Figure 3.2 graphically illustrates a similar case.

The astute reader may be concerned that the system of interest does not establish a spin temperature. The polarizers run at low pressure specifically so that terms proportional to $\frac{1}{T_{FE}}$, the spin-exchange rate due to long-lived van der Waals molecules, is large. However, even under our conditions this term, which the model of Chapter 4 estimate is tenths of Hz's, is much smaller than either the optical pumping rate or alkali spin-exchange rate, which is estimated to range from 100's of kHz's to 10's of Hz's.

3.1.1.3 RF Resonances

When the Rb atoms are subjected to an oscillating magnetic field, given by $2H_1 \cos(\omega t)$, the atomic magnetization will precess into the plane transverse to the main field. If the oscillating magnetic field is weak enough, the atomic magnetization will not precess to a large angle in a time shorter than the characteristic longitudinal relaxation time, T_1. If this is the case, the transverse atomic magnetization will reach some small, steady state

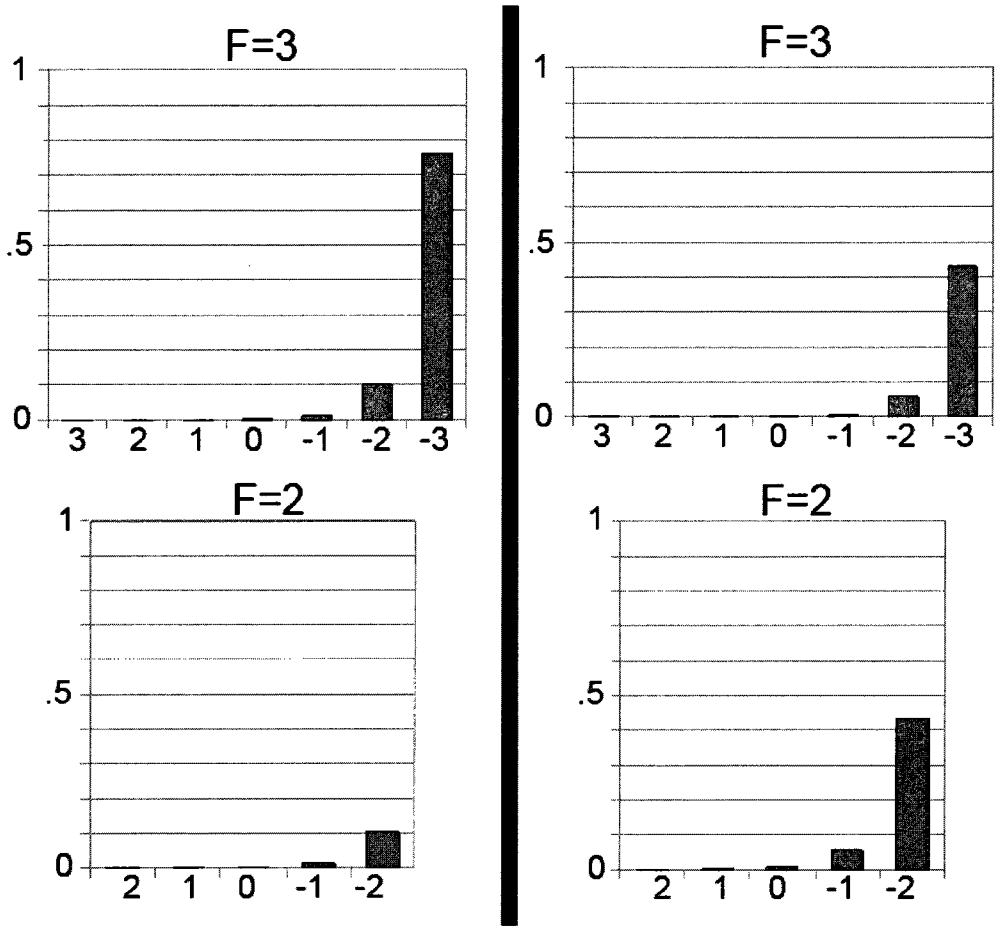

Figure 3.2. The normalized populations of ^{85}Rb with sudden and slow processes dominating. The graph on the left show the normalized populations if the $F = 3$ and $F = 2$ sublevels are allowed to mix to produce a final spin temperature population. The graph on the right shows the populations if the populations are not allowed to mix. Both graphs assume the populations of the sublevels were initially equal, and the βs in all of the cases are equal.

value. One can work out this result classically by using the Bloch equations in the limit as H_1 goes to zero.[2]

In order to relate the intensity of the hyperfine resonances to the polarization, we need to determine the expectation value of the system while subjected to the oscillating magnetic field. Appelt et al. [43] does this, and we will follow their approach.

The interaction of the oscillating field with the atoms is

$$\mathcal{H}_{\text{rf}} = 2\gamma S_x H_1 \cos(\omega t), \tag{3.21}$$

[2]Slichter works this out on pages 35-36 of the Third Edition of Principles of Magnetic Resonance[47].

where γ is the effect gyromagnetic ratio of the hyperfine transition and S_x spin operator in the x-direction. This Hamiltonian should be added to all of the other interactions listed in equation (3.16).

We can expand the steady-state density matrix as a Fourier series

$$\rho = \sum_n \rho^{(n)} e^{in\omega t} \tag{3.22}$$

The $\rho^{(n)}$'s are proportional to H_1 to lowest order. Taking only the first order terms and terms linear in H_1 from (3.22), we substitute into the modified equation (3.16) and obtain

$$\sum_{n=\pm 1} in\omega e^{in\omega t} \langle f, m \mid \rho^{(n)} \mid f, m+1 \rangle = \frac{2}{i\hbar}\gamma H_1 \cos(\omega t) \langle f, m \mid [S_x, \rho^{(0)}] \mid f, m+1 \rangle - \Lambda. \tag{3.23}$$

Here Λ is the remaining portion of the Hamiltonian from equation (3.16), neglecting diffusion, and we have taken only matrix elements of hyperfine level that are coupled due to the oscillating field, i.e. $\mid f, m \rangle$ and $\mid f, m-1 \rangle$. Λ is proportional to $e^{i\omega nt}$ due to our substitution.

It is now convenient to use the Liouville space to analyze the behavior of this system. We define the Liouville basis

$$\mid f, \bar{m}) \equiv \mid f, m \rangle \langle f, m-1 \mid \tag{3.24}$$

and

$$\bar{m} = \frac{2m-1}{2}. \tag{3.25}$$

With these definitions, we can equate coefficients of $e^{in\omega t}$ and write

$$(\Lambda + in\omega) \mid \rho^{(n)}) = \mid \sigma), \tag{3.26}$$

where $(f, \bar{m} \mid \sigma) = \frac{2}{i\hbar}\gamma H_1 \cos(\omega t) \langle f, m \mid [S_x, \rho^{(0)}] \mid f, m+1 \rangle$.

If we assume that the zeroth order density matrix $\rho^{(0)}$ is given by equation (3.13), then we can write

$$(f, \bar{m} \mid \sigma) = \frac{i\gamma H_1 \mathcal{P}_{\mathrm{Rb}} Q_{\bar{m}} (f, \bar{m} \mid S_+)}{2\hbar} \tag{3.27}$$

with the matrix element of the raising operator given as

$$(f, \bar{m} \mid S_+) = \frac{(-1)^{a-f}}{2[I]} \sqrt{[f]^2 - 4\bar{m}^2}. \tag{3.28}$$

Here, the bracket notation means $[I] = 2I + 1$, and $Q_{\bar{m}}$ is given by

$$Q_{\bar{m}} = \frac{2\mathcal{P}_{\mathrm{Rb}}(1+\mathcal{P}_{\mathrm{Rb}})^{I+\bar{m}}(1-\mathcal{P}_{\mathrm{Rb}})^{I-\bar{m}}}{(1+\mathcal{P}_{\mathrm{Rb}})^{[I]} - (1-\mathcal{P}_{\mathrm{Rb}})^{[I]}}, \tag{3.29}$$

and $\mathcal{P}_{\mathrm{Rb}}$ is the Rb polarization.

The matrix elements $(f, \bar{m} \mid \Lambda \mid f', \bar{m}')$ can be broken into real and imaginary parts. In the limit that the imaginary part dominates the character of the matrix, $\mid f, \bar{m})$ is the eigenbasis and the matrix element take on simple physical interpretations. The real part corresponds to the damping rates, $\gamma_{f,\bar{m}}$, of the coherences between hyperfine sublevels m and $m-1$, i.e. the longitudinal relaxation rate of the atomic spin to it equilibrium value for a particular hyperfine transition. The imaginary part corresponds to the resonant frequencies, $\omega_{f,\bar{m}}$ of the hyperfine coherences. With this understanding, the condition that the imaginary part of $(f, \bar{m} \mid \Lambda \mid f', \bar{m}')$ dominate the character of the matrix is equivalent to saying that the difference in the hyperfine resonances frequencies are much greater than the damping rates.

Given the condition discussed above, we can write equation (3.26) as

$$(f, \bar{m} \mid \rho^{(n)}) = (f, \bar{m} \mid \sigma)(i\omega_{f,\bar{m}} + \gamma_{f,\bar{m}} + in\omega)^{-1}, \tag{3.30}$$

where we have used, $(f, \bar{m} \mid \Lambda = (i\omega_{f,\bar{m}} + \gamma_{f,\bar{m}})(f, \bar{m} \mid$.

We are interested in the transverse component of the electron spin, as it is this that interacts with the probe beam. The RF modulated transverse component can be written as the expectation value of the electron spin-lowering operator,

$$\begin{aligned} \langle S_- \rangle &= \mathrm{Tr}(S_+)^\dagger \rho \\ &= \sum (S_+ \mid f, \bar{m})(f, \bar{m} \mid \rho) \\ &= \sum \frac{(S_+ \mid f, \bar{m})(f, \bar{m} \mid \sigma)}{i\omega_{f,\bar{m}} + \gamma_{f,\bar{m}} + i\omega}. \end{aligned} \tag{3.31}$$

Here, we have taken the sum only over the $\rho^{(n)}$'s with $n = \pm 1$, as prescribed in equation (3.23). Substituting equations (3.28) and (3.27) into equation (3.31), we get

$$\langle S_- \rangle_{f,\bar{m}} = \frac{([f]^2 - 4\bar{m}^2)\gamma H_1 \mathcal{P}_{\mathrm{Rb}} Q_{\bar{m}}}{8[I]^2 \hbar} \left(\frac{i\gamma_{f,\bar{m}} + (\omega_{f,\bar{m}} - \omega)}{\gamma_{f,\bar{m}}^2 + (\omega_{f,\bar{m}} - \omega)} \right), \tag{3.32}$$

where we have let $\omega \to -\omega$ and have rationalized the denominator. We see that we have two components to the oscillating signal, an in phase part equal to $\Im(\langle S_- \rangle_{f,m})$ and an out of phase part equal to $\Re(\langle S_- \rangle_{f,m})$. For our experiments, we will be interested in the in phase part, the so-called absorptive part, of the oscillation.

3.1.1.4 Affects on a Probe Beam

We will follow Baranga et al. [42] in deriving an expression for the interaction of the light with the electron spin. Equation (3.1) describes the attenuation of the light. If we

integrate this equation over the path length, L, of the light through the sample, we obtain the transmitted intensity expression

$$I_L = \mathrm{e}^{-\kappa L} I_0 \exp\left(2\kappa s_n \int_{-L/2}^{L/2} \langle S_- \rangle\right) \mathrm{e}^{i\omega t}, \tag{3.33}$$

where we have substituted our notation from Section 3.1.1.3 in for the transverse electron spin and have called the initial intensity incident of the sample I_0. If we keep the driving RF sufficiently small so that $|2\kappa L\langle S_n\rangle| << 1$, then we can expand the second exponential function to the first two terms of its power series:

$$I_L = \mathrm{e}^{-\kappa L} I_0 + \mathrm{e}^{-\kappa L} I_0 2\kappa s_n \int_{-L/2}^{L/2} \langle S_- \rangle \mathrm{e}^{i\omega t}. \tag{3.34}$$

If we process the transmitted light intensity signal with a lock-in amplifier referenced to the driving RF frequency ω, the first term will vanish, and the output voltage, V, from the lock-in amplifier will be

$$V = \xi \mathrm{e}^{-\kappa L} I_0 2\kappa s_n \int_{-L/2}^{L/2} \langle S_- \rangle, \tag{3.35}$$

where ξ encompasses the gains and losses due to processing the signal. We adjust the phase of the lock-in amplifier reference so that we only observe the in-phase component in equation (3.32). The voltage output of the lock-in amplifier is then

$$V_{f,\bar{m}} = \xi \mathrm{e}^{-\kappa L} I_0 2\kappa s_n \int_{-L/2}^{L/2} \frac{([f]^2 - 4\bar{m}^2)\gamma H_1 \mathcal{P}_{\mathrm{Rb}} Q_{\bar{m}}}{8[I]^2 \hbar} \left(\frac{\gamma_{f,\bar{m}}}{\gamma_{f,\bar{m}}^2 + (\omega_{f,\bar{m}-\omega})}\right) \tag{3.36}$$

If we assume $\mathcal{P}_{\mathrm{Rb}}$ is a relatively constant value over the optical path of the beam, then we can replace it with the bulk averaged polarization, $\overline{\mathcal{P}_{\mathrm{Rb}}}$, and integrate equation (3.36) explicitly and obtain

$$V_{f,\bar{m}} = \xi \mathrm{e}^{-\kappa L} I_0 2\kappa s_n \frac{([f]^2 - 4\bar{m}^2)\gamma H_1 \overline{\mathcal{P}_{\mathrm{Rb}}} Q_{\bar{m}} L}{8[I]^2 \hbar} \left(\frac{\gamma_{f,\bar{m}}}{\gamma_{f,\bar{m}}^2 + (\omega_{f,\bar{m}-\omega})}\right). \tag{3.37}$$

In our experiments, we held ω constant and swept the main field, H_0, to bring the hyperfine transitions, $\omega_{f,\bar{m}}$, onto resonances. To usually better than 1% accuracy, the differential relationship between the hyperfine frequencies and the main field is [42]

$$\left|\frac{\partial \omega_{f,\bar{m}}}{\partial H_0}\right| \approx \frac{\gamma}{\hbar[I]} \tag{3.38}$$

To find the area under the hyperfine resonance peaks, we need to integrate equation (3.37) over the field:

$$
\begin{aligned}
A_{f,\bar{m}} &= \int_{-\infty}^{\infty} V_{f,\bar{m}} dH_0 \\
&= \frac{\hbar[I]}{\gamma} \int_{-\infty}^{\infty} V_{f,\bar{m}} d\omega_{f,\bar{m}} \\
&= \xi e^{-\kappa L} I_0 2\kappa s_n \frac{([f]^2 - 4\bar{m}^2) H_1 \overline{\mathcal{P}_{Rb}} Q_{\bar{m}} L}{8[I]} \int_{-\infty}^{\infty} \frac{\gamma_{f,\bar{m}}}{\gamma_{f,\bar{m}}^2 + (\omega_{f,\bar{m}-\omega})} d\omega_{f,\bar{m}} \\
&= \pi G \frac{([f]^2 - 4\bar{m}^2) \overline{\mathcal{P}_{\mathrm{Rb}}} Q_{\bar{m}} L}{8[I]},
\end{aligned}
\tag{3.39}
$$

where $G = \xi e^{-\kappa L} I_0 2\kappa s_n H_1$. In the next section, we will describe how this equation is used to calculate the average polarization $\overline{\mathcal{P}_{\mathrm{Rb}}}$ across the sample.

3.2 Experimental Setup

Figure 3.3 shows a schematic of the apparatus used to detect the ^{85}Rb resonance. A pair of coils in a Helmholtz configuration provided an RF field to excite transitions between the hyperfine levels. A probe beam of circularly polarized light, tuned ≈0.2 nm off of the Rb D_1 transition wavelength, propagated through a secant of the optical pumping cell. When on resonance, the Rb electrons modulated the intensity of the probe beam. The main magnetic field was swept to bring the ^{85}Rb hyperfine levels onto resonance. We optimized the sweep rate by varying the sweep rate and assuring the optical absorption line shape did not change.

A fast-response photodiode (Edumund Optics 54-520) detected the probe beam, and a home-built lock-in amplifier, referenced to the frequency of the exciting RF, demodulated the signal. During the experiment, the Helmholtz coils were oriented such that all the Rb resonances had the same phase with respect to each other. However, we did measure some spectra with the Helmholtz coils oriented such that the $F = 3$ and $F = 2$ sublevels differed in phase by 180°, but none of the data we analyzed was taken in this manner because of an artifact described in more detail in Section 3.3.5. The artifact was such that it was difficult to differentiate between it and the absorption signal when the sublevels absorption peaks differed in phase by 180°.

A digital oscilloscope processed the lock-in amplifier signal, which we downloaded for analysis.

We attached a Golay coil to the system to help shim out magnetic field gradients. We later determined that much of the magnetic field gradient was due to the 2 kG permanent magnet on the polarizer for use with cryogenic experiments. Even after we removed this major source of field inhomogeneities, we keep the Golay coil to shim out smaller gradients.

The laser diode and photodiode were attached to an apparatus that allowed them to move up and down along the axis of the cell. The Golay coil and RF coils were attached

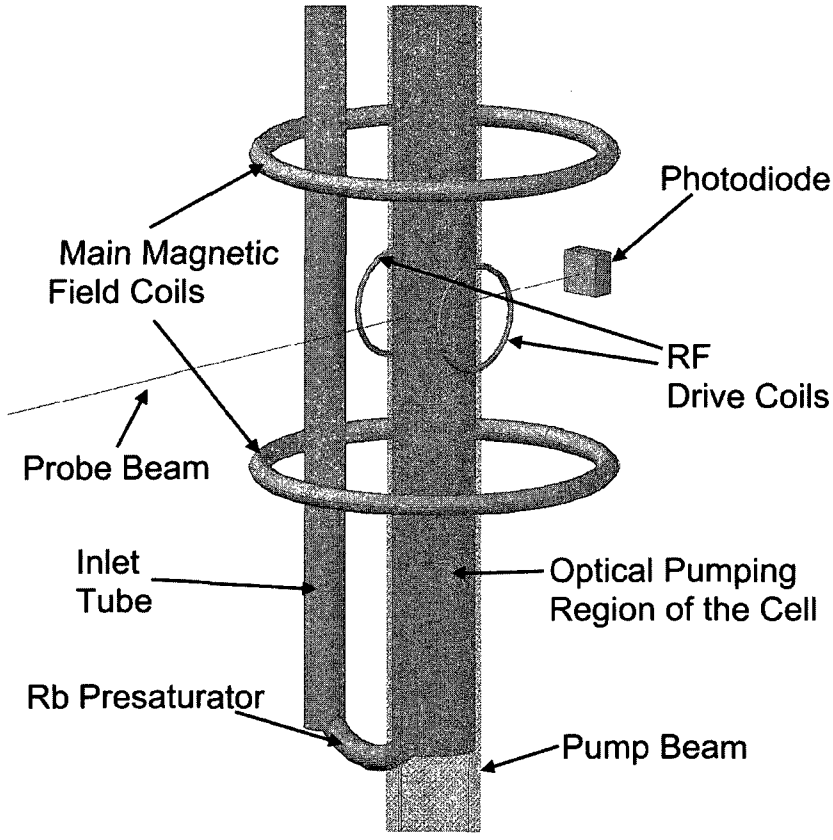

Figure 3.3. The experimental setup for the Rb polarimetry measurement required both RF and optical excitation of the ^{85}Rb electrons. A pair of untuned, 8 cm diam. drive-coils with 25 windings per coil provided the RF field using a drive power between -5 and -15 dBm at 13.1 MHz. We tuned the 80 mW probe laser by a combination of temperature control of the emitter junction and a small external Littrow cavity. The main magnetic field (provided by the polarizing coils) was shimmed in the region of interest by a Golay coil [48](not shown) attached directly to the outside of the cell. The field was swept at a rate of 2.26 G/s over the range of $\approx$ 27-28 G to generate the ^{85}Rb hyperfine spectra, like that shown in Figure 3.4, from which the Rb polarization was determined [see Eq. (3.41)-(3.43)]. The entire ODEPR apparatus (probe laser and photodiode) was attached to a mobile assembly so that $\mathcal{P}_{\mathrm{Rb}}$ could be probed at different vertical positions along the axis of the cell. The probe beam was directed through a narrow window that ran the entire length of the oven on both sides. The other components (RF and Golay coils) where attached directly to the cell and had to be moved to different positions by hand.

directly to the cell and thus had to be moved by hand.

The main magnetic field sweep rate and scale were determined by the positions of the ^{85}Rb absorption peaks. After calibration and baseline correction of the signal, we numerically integrated the first, second, and third absorption peaks: $A_{3,-5/2}$, $A_{2,-3/2}$, and $A_{3,-3/2}$, respectively (see Figure 3.4). In the figure, $A_{3,-5/2}$ and $A_{3,-3/2}$ are due to transitions in the $F = 3$ manifold and $A_{2,-3/2}$ is due to a transition in the $F = 2$ manifold.

Setting $I = \frac{5}{2}$ for ^{85}Rb and using equation (3.39), we have

$$A_{3,\bar{m}} = \frac{\pi G}{8[I]}([3]^2 - 4\bar{m}^2)\overline{\mathcal{P}_{Rb}}Q_{\bar{m}}L, \tag{3.40}$$

$$A_{2,\bar{m}} = \frac{\pi G}{8[I]}([2]^2 - 4\bar{m}^2)\overline{\mathcal{P}_{Rb}}Q_{\bar{m}}L. \tag{3.41}$$

We determined Rb polarization by taking the ratio of the areas of the peaks and using the following equations:

$$\overline{\mathcal{P}_{Rb}} = \frac{7r_1 - 3}{7r_1 + 3} \tag{3.42}$$

$$\overline{\mathcal{P}_{Rb}} = \frac{5r_2 - 3}{5r_2 + 3} \tag{3.43}$$

where $r_1 = \frac{A_{3,-5/2}}{A_{2,-3/2}+A_{3,-3/2}}$ and $r_2 = \frac{A_{3,-5/2}}{A_{3,-3/2}}$ [42, 49]. We evaluated the ^{85}Rb polarization using both expressions and checked that they reasonably agreed. This assured the

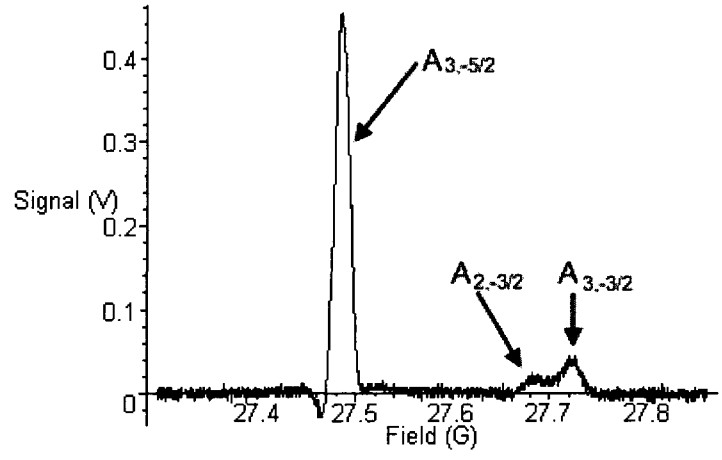

Figure 3.4. A sample of ^{85}Rb ODEPR spectrum. This sample contains an anomalous dip in signal downfield of the first absorption peak. The feature is not an artifact of incorrectly setting the phase relation between the reference and signal for the lock-in amplifier as it is impossible to find a phase relationship that yields a completely absorptive peak. Note the second and third transitions upfield are not well resolved and have the same phase relation.

accuracy of the technique and that the Rb population's distribution was described well by a spin temperature distribution.

3.3 Rb Polarimetry Results and Discussion

3.3.1 Temperature Dependence

We measured the Rb polarization as a function of temperature under the conditions described in Section 2.4.1 (see Figure 3.5). At low temperatures, we maintain very high Rb polarization deep in the optical pumping cell. However, as we increased the temperature, the Rb polarization dropped off deeper in the optical pumping cell, and at the highest temperature, the polarization at the top of the heated region of the optical pumping cell was depressed.

These measurements are consistent with the picture described in Section 2.4.1 to explain the ^{129}Xe temperature dependence. As the temperature increases, the [Rb] also increases and the optical transparency of the vapor decreases. More light is absorbed at the top of the heated region of the optical pumping cell leaving fewer photons available

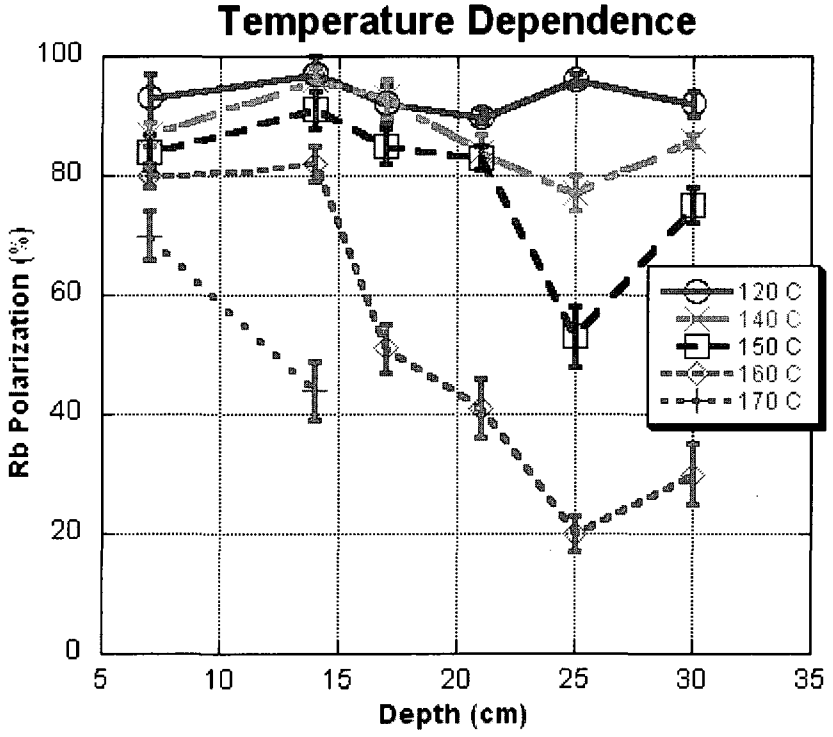

Figure 3.5. The Rb polarization temperature dependence as a function of depth in the optical pumping cell. The x-axis is referenced to the top of the oven. Although the cell extends 50 cm into the oven, we were only able to measure to 30 cm depth. Build up of Rb on the side of the optical pumping cell wall at lower depths impeded the propagation of the probe beam and prevented us from taking measurements in that region.

to optically pump the Rb lower in the optical pumping cell. As the light attenuates, the bulk averaged Rb polarization decreases causing the optical transparency to decrease even further, and the light is more quickly attenuated. In the extreme case, only a small layer of Rb would become polarized and absorb all of the light in the process, and all of the layers below it would be only thermally polarized.

We shall see in Section 4.7 that, although the Rb polarimetry followed the predicted trend qualitatively, it does not compare well with calculated results. The implications of this are discussed later.

3.3.2 Total Flow Rate Dependence

We measured the total flow rate dependence of the Rb polarization as a function of depth under the same condition described in Section 2.4.2 (see Figure 3.6). The appearance of a slight total flow dependence on the Rb polarization was unexpected. The polarization appears to decrease with increasing flow rate. We believe that this is a fluid dynamical affect caused by the Rb vapor being pushed into the unheated region of

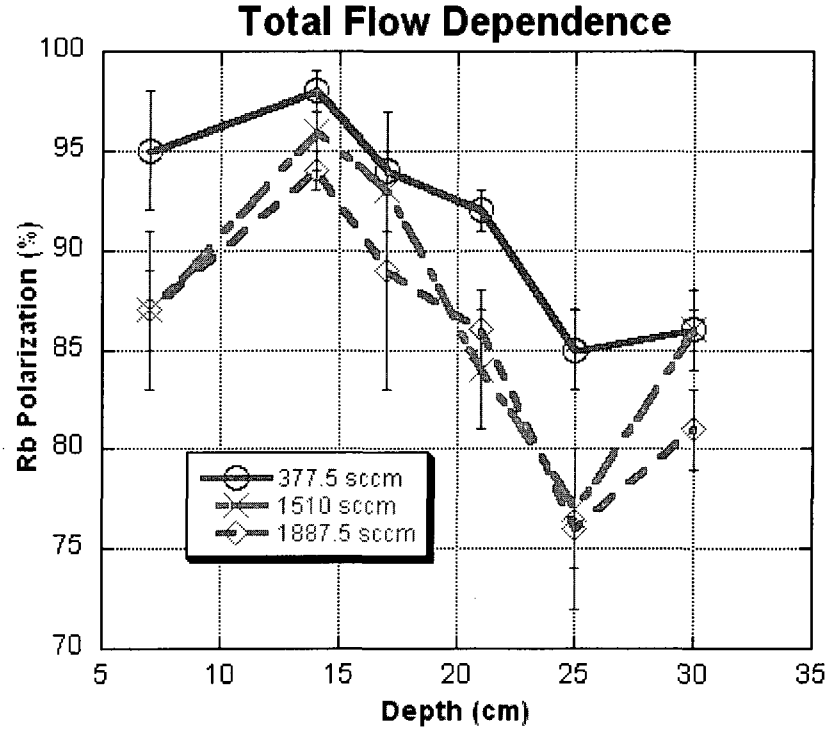

Figure 3.6. The Rb polarization total flow rate dependence as a function of depth in the optical pumping cell. The graph layout is identical to that of Figure 3.5. There appears to be a slight dependence on the total flow rate through the optical pumping cell. Higher flow rates appear to give rise to lower polarizations of Rb.

the optical pumping cell. This would effectively increase the [Rb] in the unheated portion of the cell and, thus, decrease the available pumping light in the heated region. Higher flow rates may push more Rb vapor into the unheated portion of the cell producing the observed lower polarization.

3.3.3 [Xe] Dependence

The [Xe] dependence of the Rb polarization is shown in Figure 3.7. As predicted, the Rb polarization suffers as [Xe] concentration increases, and this is due to the strong relaxing interaction between Xe and Rb. The Rb polarization is more quickly destroyed resulting in lower Rb polarizations. The lower polarization higher in the optical pumping cell results in less optical transparency and more light absorption. Thus, there is less light available to lower layers in the cell, and the Rb polarization decreases.

The mechanism should be differentiated from the temperature dependence, although the affects are similar. At higher temperatures, there are insufficient photons available to maintain the Rb polarization. At higher [Xe], the Rb polarization is more quickly destroyed by interacting with an abundance of Xe. In the extreme case of high [Xe], the

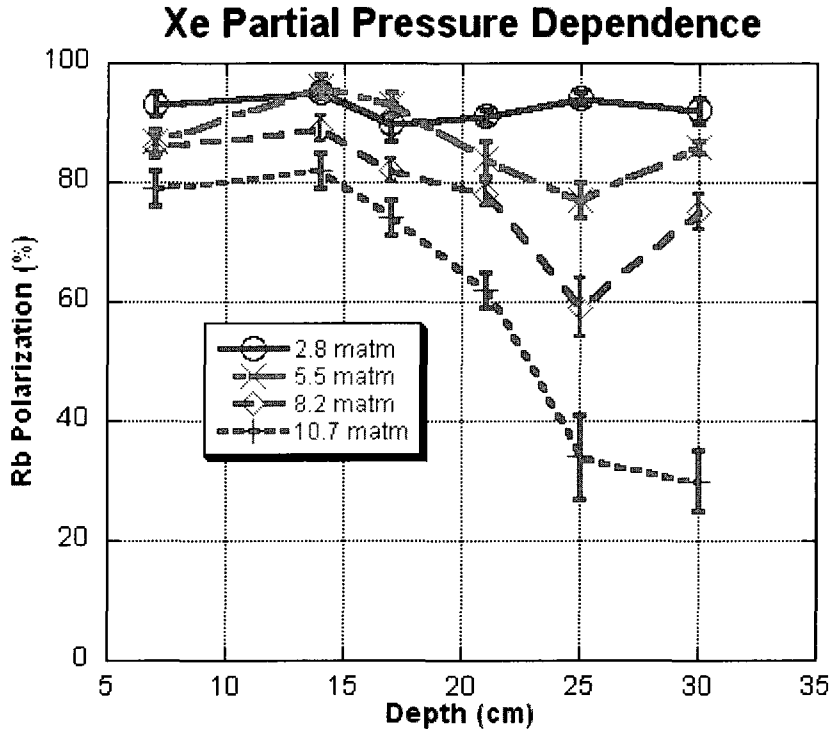

Figure 3.7. The Rb polarization Xe concentration dependence as a function of depth in the optical pumping cell. The graph layout is identical to that of Figure 3.5. There is a steady decline in the Rb polarization as the Xe partial pressure increases.

light cannot generate any Rb polarization in the cell, while in the extreme cases of high temperature, there will always be some very small layer of Rb polarization.

3.3.4 Pressure Dependence

As with the ^{129}Xe polarization, the Rb polarization shows very little dependence on the total gas pressure in the optical pumping cell (see Figure 3.8). None of the pressure effects suggested in Section 2.4.4 are evident in the polarimetry. One would expect an increase in pressure to increase Rb relaxation due to an increase Xe partial pressure. This would result in a decrease in the Rb polarization. However, an increase in pressure should also broaden the Rb absorption line resulting in more effective optical pumping of the Rb. This would have the effect of increasing the Rb polarization at the top of the cell, but a lower polarization deeper in the cell due to a stronger absorption of light in higher layers. Neither of these effects are seen which suggests that either they are slight or, to some degree, cancel each other out. Measurements of the dependence Rb polarization on [Xe] would seem to indicate that its effect is significant. Then, it is likely that the effects cancel each other out resulting in a flat response in the Rb polarization as a function of pressure.

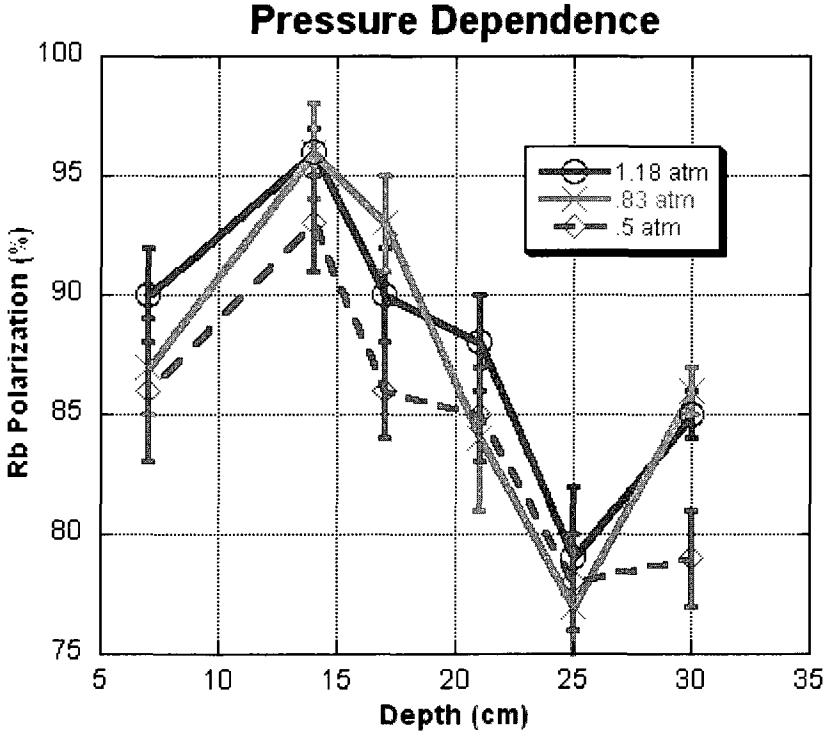

Figure 3.8. The Rb polarization total pressure dependence as a function of depth in the optical pumping cell. The graph layout is identical to that of Figure 3.5.

3.3.5 Unexplained Effects

In the course of the experiment, we made several observations for which we have not yet formulated explanations. The first unexplained effect was in the ^{85}Rb ODEPR spectra, and the second observation was in the resulting ^{85}Rb polarization profile.

We observed a negative absorption peak or peaks in the ^{85}Rb ODEPR spectra whose presence we cannot explain (see Figure 3.4 and Figure 3.9). The features were usually observed around the strongest ^{85}Rb resonance peak, which corresponds to a transition between the F=3, m=-3 and F=3, m=-2 states. However, they were occasionally observed around the third absorption peak, which was the transition between F=3, m=-2 and F=3, m=-1 states. We adjusted a number of parameters in the experiment in an attempt to determine the cause of the effect, and we found a number of them that seemed to affect the shape or size of the features. The features appeared to be independent of main magnetic field sweep rate, probe laser polarization (i.e. the helicity of the light), and probe laser power. They were occasionally dependent on the pump laser and probe laser tuning (i.e. the frequency at which we forced the lasers to operate), the total gas pressure in the optical pumping cell, main magnetic field inhomogeneities, and Xe concentration. However, adjustment of these parameters could not completely eliminate the features from all spectra.

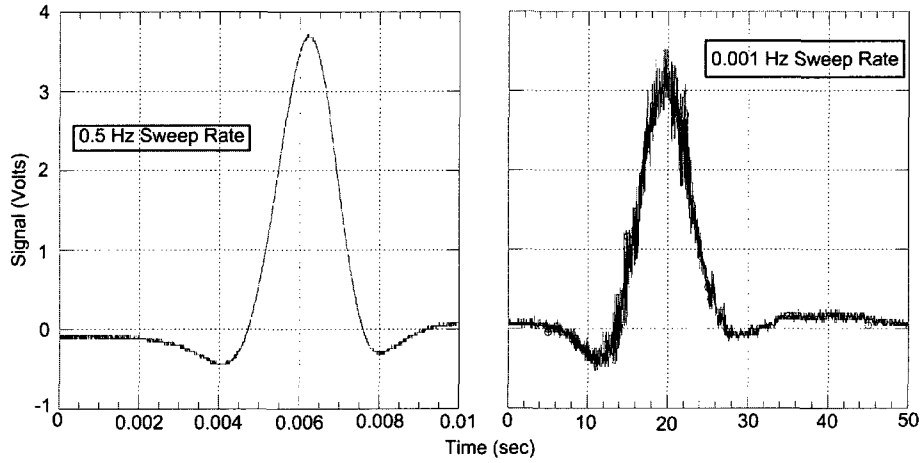

Figure 3.9. Two traces of the F=3, m=-3 to F=3, m=-2 resonance peak taken with a .001 Hz and .5 Hz sweep rates. Here, the sweep rate refers to the rate at which the entire field range ($\approx$ 2 G) was swept. Calibration of the field was not possible in these scans because of the lack of other absorption peaks in the spectra. Clearly, the negative absorption peaks are unaffected by a two order of magnitude change is main magnetic field sweep rate. Other parameters in the experiments seemed to affect the features. Shimming of the field to provide a very homogenous magnetic field seemed to eliminate the features from all the of the spectra except those obtained at a depth of 30 cm.

Perhaps the most surprising discovery was that the features depended on the pump laser beam propagation direction. This seemed to be due to different line shapes originating from different parts of the optical pumping cell. We were able to observe these different contributions by blocking a portion of the pumping beam and recording a ^{85}Rb spectrum.

We thoroughly tested the electronics to eliminate signal defects due to capacitance or electronic frequency response. We tested the frequency response of the lock-in amplifier by injecting a short pulse from an NMR spectrometer set to the same frequency as the reference for the amplifier. We observed that the lock-in amplifier correctly demodulated the pulse and did not seem to shape it. We attempted to eliminate any problems that may have been due to the photodiode by upgrading the normal response photodiode (Edmund Optics H53-372) with a high-speed response photodiode (Edumund Optics 54-520). We further upgraded the design of the photodiode electronics to impendence match the circuit with the lock-in amplifier (see Figure 3.10). This did not eliminate the features.

We observed a depression in the Rb polarization profile that we were also unable to

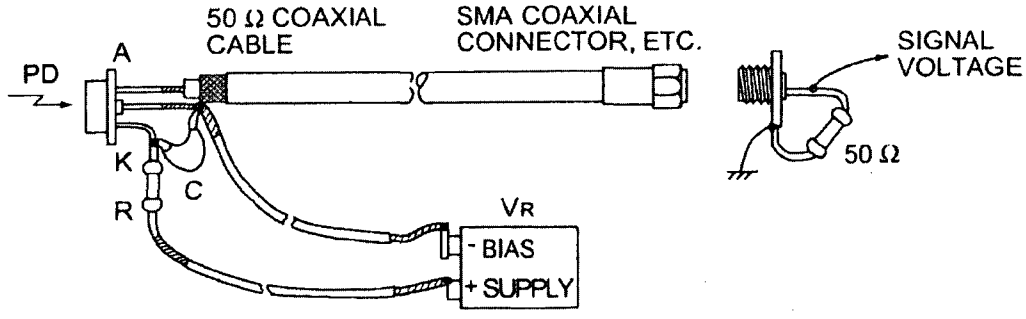

Figure 3.10. The wiring diagram used with the Edmund Optics 54-520 photodiode to monitor the modulation of the absorption of the probe beam. The circuit is impedance matched to 50Ω. The design and figure are courtesy of Hamamatsu Photonics.

explain. There are two depressions that appear in the polarization profiles (although they are most clearly seen in Figures 3.8 and 3.6). The first depression at 7 cm depth is likely due to an excess of Rb metal condensed on the walls in the water-cooled region. Appelt et al. noted a similar depression near excess Rb and ascribed it to an enhanced evaporation of the Rb [50]. The depression at 25 cm cannot be similarly explained. Visual inspection of the area does not reveal excess plated Rb relative to areas near it. It is possible that there exists some turbulent flow that conspires to lower the Rb polarization in this area. Unfortunately, a qualitative theory has yet to be formulated to account for this effect.

3.4 Conclusion

I have presented measurements of the Rb polarization profile in Polarizer 2. Many of the measurements agree qualitatively with the theory, although there were some surprises. In particular, we noted a dependence on the total flow rate of the gas mixture and a lack of dependence on the total pressure. The total flow rate dependence may be due to fluid dynamical effects, and the lack of total pressure dependence is probably caused by cancellation of two competing effects.

I further noted unexplained features in the ^{85}Rb ODEPR spectra and the Rb polarization profile. The ODEPR spectra contain negative absorption peaks surrounding the resonant peaks that we could not explain or adequately characterize. The polarization profile contains an unexpected depression.

Future research should attempt to further characterize the system and explain these unexpected features. Additional studies should include in situ ^{129}Xe polarimetry, Rb polarization imagining along a cross section of the optical pumping cell, and investigation into the [Rb] in the optical pumping cell as a function of position.

CHAPTER 4

MODEL OF A ^{129}XE POLARIZER FLOW-THROUGH SYSTEM

4.1 Introduction

The principles of production of hyperpolarized Xe using a flow-through system are conceptually very simple. However, both the Xe and the Rb undergo interactions other than those outlined in Chapter 1, which can make prediction of the actual behavior of the system complex. We constructed a numerical model of the flow-through system to handle these complex interactions and to guide our understanding of the system behavior so we could optimize it.

The model was originally developed by Iulian Ruset and outlined in his thesis [11]. It was later revised and adapted by us. There are three main differences between the Ruset model and ours. First, the Ruset model is implemented using a Microsoft Excel Spreadsheet, and our model is written in Maple code (see Appendix B). Second, the Ruset model uses less common techniques to numerically approximate integrals and differential equations in the model; while our model uses the more common Euler method for approximating differential equations and the trapezoid method for approximating integrals. Finally, although the underlying equations for spin-exchange optical pumping and calculations for various spin-exchange and relaxation rates are mainly the same, we have employed a more complicated expression for the spin-exchange rate between Rb and Xe in our model.

The model is one-dimensional, that is, it assumes that laser intensity, polarization, number densities, spin-exchange, and relaxation rates are all independent of spatial position in the plane transverse to the direction of the propagation of the laser beam. One quantity, the Xe flow velocity, is two-dimensional, taking into account the finite viscosity of the fluid and the drag of the walls of the cell. However, the quantity derived from the Xe polarization is later averaged over the transverse plane to return a bulk-averaged quantity that varies only in the axial direction.

The model outputs the axial distribution of the optical pumping rates $\gamma_{opt}(z)$, Rb polarization $\mathcal{P}_{\mathrm{Rb}}$, and ^{129}Xe polarizations $\mathcal{P}_{\mathrm{Xe}}$, and it calculates the spectral line shape $\psi(\nu, z)$ of the pump laser beam as it passes through the cell. There are limitations

to the model, including the fact that many important rates and relaxation times have been measured only at high pressures or for specific gas compositions. At best, these can be crudely extrapolated to the empirically determined conditions that maximize the polarizer's efficiency. Finally, the model does not account for complex heating and fluid dynamical effects such as convection and turbulence [51], which may lead to inhomogeneities in the transverse plane and significantly affect performance.

In his thesis, Ruset gave an excellent and detailed description of all of the underlying physics present in the model. So as not to plagiarize or unnecessarily repeat information, I'll refer the interested reader to his thesis[11]. In this chapter, I will instead present a description of the implementation of the model, commenting on the relevant physics as appropriate. You can find a complete reproduction of the Maple code we used in Appendix B.

The model is implemented in three steps that will be described in more detail later. The first step approximates solutions to the differential equation for the absorption of the laser as it transverses the cell. The second step calculates the polarization of the rubidium as a function of axial position in the optical pumping cell. Finally, in the third step the Xe polarization is calculated, also as a function of axial position in the pumping cell.

The model has several variable inputs. The total pressure and flow rates are used to compute relaxation, spin-exchange rates, and the rubidium absorption line width. The oven temperature is used to calculate the rubidium number density. The incident laser power allows us to calculate the initial photon flux into the cell.

4.2 Optical Absorption

The pump laser absorption is described by the following differential equation [34]:

$$\frac{\partial \psi(\nu)}{\partial z} = -\lambda_{\sigma_-}^{-1}\psi(\nu), \tag{4.1}$$

where ψ is the photon flux density, z is the axial position variable, and $\lambda_{\sigma_-}^{-1}$ is the mean length a circularly polarized photon will travel before being absorbed by a Rb atom.

The length λ_{σ_-} is the mean distance a left-hand circularly polarized photon will travel before being absorbed by a Rb atom. It is a function of frequency, Rb number density and polarization. This length is given by [34]:

$$\lambda_{\sigma_-}^{-1} = 2[\mathrm{Rb}]\sigma_s(\nu)\rho_{+1/2}, \tag{4.2}$$

where [Rb] is the Rb number density, σ_s is the cross section associated with an unpolarized rubidium atom absorbing a photon, and $\rho_{+1/2}$ is the probability of finding the rubidium atom in the $+\frac{1}{2}$ spin state.

We calculate [Rb] by using assuming thermal equilibrium and using the vapor pressure curves determined by Killian [52]. The temperature of the optical pumping region is modeled by a constant temperature, T_0, in the heated region of the cell and by $T_1+(T_0-T_1)e^{\frac{z-L}{L_c}}$ in the unheated region of the cell. Here, T_1 is room temperature, z is the axial position, L is the heated length of the cell, and L_c is a length that characterizes how quickly the temperature falls from the heated temperature to room temperature. This profile is based on Newton's law of cooling, which predicts an exponential relaxation of temperature in time. This exponential decay in time can be transformed into a exponential decay in position for a moving fluid.

Both ψ and σ_s are in general functions of optical frequency ν. For ψ, we choose a Gaussian distribution to approximate the initial spectral profile. The initial photon flux density is estimated from the total power output of the laser. For all of the simulations presented here, the power was taken to be 30 W. This approximately corresponds to the laser power we measured to be incident on the polarizing cell in Polarizer 2 for the measurements described in Chapters 2 and 3. We set the width of the Gaussian to correspond to the typical spectral width of our narrowed lasers, 0.3 nm.

The alkali absorption profile, σ_s, has a Lorentzian line shape given by:

$$\sigma_s = \frac{(\delta_\sigma/2)^2}{(\nu-\nu_0)^2+(\delta_\sigma/2)^2}\sigma_0. \tag{4.3}$$

In the above equation, σ_0 sets the maximum absorption cross-section, which Wagshul et al. reported to be $\approx 10^{-13}$ cm^2[34]. We used the sum rule to calculate the pressure dependent value of σ_0 [53]. We use the sum rule,

$$\int_0^\infty \sigma_s(\nu)d\nu = \pi r_e c f, \tag{4.4}$$

with the integral of equation (4.3),

$$\int_0^\infty \sigma_s(\nu)d\nu = \frac{\pi}{2}\sigma_0\delta_\sigma. \tag{4.5}$$

In equation (4.4), r_e is the classical radius of an electron, c is the speed of light, and f is the oscillator strength of the D_1 transition. Evaluating the right hand side of equation (4.4) and setting it equal to the right hand side of equation (4.5), one finds:

$$\sigma_0 = \frac{\sim 5.7\times 10^{-3}}{\delta_\sigma}\text{cm}^2. \tag{4.6}$$

The width, δ_σ, is dominated by pressure broadening due to buffer gases. The contributions to the line width due to various gases have been measured by Romalis et al.[35], and the contributions are all about 18 GHz/amg.[1] The natural line width and the width

[1]The unit *amg* may be unfamiliar to some readers. It refers to an amagat, which is defined by the ratio of the density of the gas to that of an ideal gas at 1 atm and 0 °C

due to Doppler broadening are measured in MHzs [33] and GHzs [54], respectively, and they are neglected.

In our model, we calculated σ_0 by determining δ_σ for our standard gas concentrations.[2] We determined $\sigma_0 = 0.38 \times 10^{-12}\,\mathrm{cm}^2$. For different pressure, we allowed δ_σ to vary, but not σ_0.

It can be shown that in steady state [34]:

$$\rho_{-1/2} - \rho_{+1/2} = \frac{\gamma_{opt}(z)}{\gamma_{opt}(z) + \Gamma_{SD}(z)}. \tag{4.7}$$

In the above equation, $\gamma_{opt}(z)$ is the optical pumping rate and $\Gamma_{SD}(z)$ is the rubidium spin destruction rate. Recall from equation (2.1) that the optical pumping rate is given by $\gamma_{opt}(z) = \int_0^\infty \psi(\nu, z)\sigma_s(\nu)d\nu$, and the spin destruction rate is tabulated from various terms described in the literature [11, 55, 42, 56].

Using the fact that $\rho_{+1/2} + \rho_{-1/2} = 1$, we can solve for $\rho_{+1/2}$. Using this result, we can write the equation for laser absorption as

$$\frac{\partial\psi(\nu, z)}{\partial z} = -[\mathrm{Rb}]\sigma_s(\nu)\frac{\Gamma_{SD}(z)}{\gamma_{opt}(z) + \Gamma_{SD}(z)}\psi(\nu). \tag{4.8}$$

This differential equation can be discretized and solved using numerical techniques. In our model, this is solved by using Euler's method. The Ruset model uses an exponential approximation to the solution. Both methods yield comparable results.

From these equations, the numerical model predicts two quantities. First, it predicts the frequency dependent photon flux $\psi(\nu, z)$ as a function of axial position in the optical pumping region. Second, it calculates the optical pumping rate $\gamma_{opt}(z)$, and it is used in the next section of the model.

4.3 Rubidium Polarization

After approximating the photon flux profile in the cell, it becomes a simple matter to extract Rb and Xe polarization. The Rb polarization is calculated by the following expression:[34]

$$\overline{\mathcal{P}_{Rb}(z)} = \frac{\gamma_{opt}(z)}{\gamma_{opt}(z) + \Gamma_{SD}(z)} \tag{4.9}$$

where $\overline{\mathcal{P}_{Rb}(z)}$ denotes the transverse bulk averaged polarization of the Rb.

The term $\Gamma_{SD}(z)$ is the aforementioned spin destruction rate for Rb, of which there are three components. The first, and perhaps least understood, is Rb-Rb spin destruction. Up until 1998, it was thought that Rb-Rb spin destruction was dominated by binary

[2]This "standard gas concentration" came about after we'd built and tested the polarizer. So while, we built the model first, we finalized it later. The standard conditions were Xe: 0.005 amg, N_2: 0.27 amg, and He: 0.54 amg.

interactions because of the relative insensitivity of the relaxation rate with respect to total gas pressure [53]. Kadlecek et al. [57] observed a substantial (factor of 3) reduction in the Rb-Rb spin relaxation rate for modest fields of a few kG and an anomalously high relaxation rate for total gas pressure below 100 torr. Both of these observations are inconsistent with a simple binary collision theory [38, 53, 58]. Since then, a number of spin relaxation mechanisms, such as alkali metal dimers [59], have been described to account for different behaviors in different regimes and are summarized in Kadlecek's thesis [60]. Thankfully, these complexities do not concern the current model and are brought up only to impress upon the reader the limitation of the model and the possibility of extending the model to other, possibly interesting, regimes.

For this specific work, we used the value determined by Baranga et al. [38] for the linear dependence of the Rb spin destruction rate on the [Rb], that is

$$\Gamma_{SD}^{\mathrm{Rb-Rb}} = \kappa_{SD}^{\mathrm{Rb-Rb}}[\mathrm{Rb}]. \tag{4.10}$$

Baranga et al. determined the value of $\kappa_{SD}^{\mathrm{Rb-Rb}}$ to be $(3.9 \pm 0.4) \times 10^{-14}$ cm^{3}s^{-1} while studying the optical pumping of ^{3}He in an N_2 buffer gas at $\approx$30 G field. The experimental conditions under which they determined this value are close enough to our own conditions that additional corrections should not be necessary.

Inert buffer gases in the optical pumping gas mixture also give rise to Rb spin destruction. These are thought to be due to binary collision with an interaction time of $\approx$ 1 ps and mediated by the spin rotation interaction $\gamma \mathbf{N} \cdot \mathbf{S}$. Walter et al. [56] have measured the Rb spin destruction cross sections due to N_2 and ^{3}He to be

$$\Gamma_{SD}^{\mathrm{N_2}} = (170 \pm 11)\left(1 + \frac{T - 90\,^{\circ}C}{194.36\,^{\circ}C}\right)[\mathrm{N_2}]\,\mathrm{s}^{-1} \tag{4.11}$$

and

$$\Gamma_{SD}^{\mathrm{He}} = (24.6 \pm 1.0)\left(1 + \frac{T - 90\,^{\circ}C}{96.4\,^{\circ}C}\right)[\mathrm{He}]\,\mathrm{s}^{-1}, \tag{4.12}$$

where $[N_2]$ and [He] are the number densities of buffer gases in amagats. We assume that the isotopic differences between ^{3}He and ^{4}He do not seriously contribute to Rb spin destruction rate. Thus, we do not apply any corrections to equation (4.12) for the buffer gas mixture in our model, which presumes predominately ^{4}He.

The final contributions to the Rb spin destruction rate are those due to interactions with Xe, and these are the dominant Rb spin destruction rates in the problem. While the preceding mechanisms give rise to relaxation rates measured in Hz to tens of Hz's, Xe-Rb spin destruction rates are measured in kHz. The spin destruction rates used in our model are based on measurements by Nelson et al. [55] and a modification suggested by Ruset in his thesis [11].

There are two mechanisms for Rb-Xe spin destruction: binary collisions and molecular relaxation. Binary collisions between Xe and Rb are similar to the relaxation mechanism described above for other buffer gases and is dependent only on [Xe]. Nelson et al. reported the Rb spin destruction cross section due to Xe at 150 °C to be $(2.44 \pm 0.02) \times 10^5 \text{amg}^{-1}\text{s}^{-1}$[55]. Nelson et al. also measured the cross section at 80 °C and demonstrated a slight temperature dependence in the quantity. However, with only two points from which to extrapolate, we did not include any temperature dependence of this cross section in our model.

The molecular relaxation component is more complicated and can be broken up into different regimes. Molecular formation and breakup rates increase as the total gas pressure increases. There are two different characteristic time scales involved when considering molecular relaxation: the characteristic hyperfine precession period of the Rb electron about the nuclear spin and the precession period of the Rb electron about the angular momentum of the colliding pair. The hyperfine interaction, described by $A\mathbf{I} \cdot \mathbf{S}$, is shorter than the second, spin rotation interaction, described by $\gamma \mathbf{N} \cdot \mathbf{S}$.

These time scales break the molecular relaxation rates into three regimes. In the first, "very short lifetime" regime, the total gas pressure is sufficiently high that the molecular lifetime is short compared with both time scales. These short interactions allow transitions such that $\Delta F = 0, \pm 1$, where F is the alkali total angular momentum quantum number for the electron/nucleus pair. The second regime, the so called "short lifetime" regime, the molecular lifetime is short compared with spin rotation interaction, but long compared to the hyperfine interaction. Because of long time of the interaction compared with the hyperfine interaction, only $\Delta F = 0$ transitions may occur. In the last, "long lifetime" regime, the molecular lifetime is long compared with both the spin rotation interaction and the hyperfine interaction. Again, only transitions with $\Delta F = 0$ are allowed. For our experiments, the molecular lifetimes were usually short.[3]

Nelson et al. characterized all of these interactions by a single, pressure independent rate, Γ_{vdW}. This rate can be thought of as the contribution due to Rb-Xe van der Waals molecules in the "very short lifetime" regime or the relaxation rate of a fictitious, 0 nuclear spin alkali isotope in the "short lifetime" regime. Corrections for other regimes are given by Nelson for natural abundance Rb [10]:

$$\Gamma_{vdW}^{cor} = (0.2526 f_{0,85} + 0.1049 f_{0,87} + 0.4665 f_{1,85} + 0.1749 f_{1,87})\, \Gamma_{vdW}.^4 \qquad (4.13)$$

[3]Although our Xe-Rb molecular lifetimes were long enough such that $\Delta F = 0$, it does not follow that all the Rb interactions were this long. There are other indications that sudden interactions dominated the Rb interactions as described in Sections 3.1.1.2 and 3.1.1.4.

[4]I've removed the paramagnetic coefficient that Nelson had to use for his measurements in this equation.

The $f_{1,i}$'s are the fraction of molecules in the "very short lifetime" regime, and $1 - f_{0,i}$'s represent the fraction of Rb-Xe molecules in the "short lifetime" regime. The i's denote the different isotopes of Rb. The coefficient in front of the terms are a combination of terms describing the abundance of each isotope and the differences in the hyperfine interaction due to nuclear spins.[5]

In our model, we have ignored the complications of different regimes and made the assumption of being in the "very short" limit, that is the spin destruction rate due to Xe-Rb molecules is given simply by Γ_{vdW}. In this limit, the spin destruction rate is the fastest, and this represents a worst-case spin destruction rate. This assumption is probably incorrect to some degree and may explain some of the discrepancies that will be discussed later.

Nelson et al. measured Γ_{vdW} under the very specific gas composition conditions of 1% Xe, 1% N_2, and balance He. Although Γ_{vdW} is density independent, it is dependent on gas composition. To account for this, we follow Ruset's suggestion to extrapolate Γ_{vdW} to different gas compositions [11]. He approximated the Rb-Xe van der Waals molecular relaxation rate as:

$$\Gamma_{vdW} = \frac{6469}{f_{Xe} + 1.1 f_{N_2} + 3.2 f_{He}} \tag{4.14}$$

where the f_G's are the volumetric fractions of the constituent gases. The coefficients in front of the volumetric fractions are estimated by comparing the van der Waals specific spin-exchange rates from equation (1.4). Specifically, the coefficient of f_{N_2} is given by $\frac{\gamma_{N_2}}{\gamma_{Xe}}$ and the one in front of f_{He} is given by $\frac{\gamma_{He}}{\gamma_{Xe}}$. One should regard this extrapolation as a very crude estimate.

We estimated the total Rb spin destruction rate by summing the contributions of all of the terms described above.

4.4 ^{129}Xe Polarization

The expression for the Xe polarization is slightly more involved. Since the Xe is flowing axially through the cell, the total flow velocity must be taken into account when

---

This coefficient, related to the slow down factor, among other things describes the influence of the nuclear polarization on the relaxation of the electron polarization. It is particularly important when measuring Rb relaxation rates, because it turns out that due to the strong coupling of the nucleus and the electron, highly polarized Rb atoms will relax faster than lower polarized Rb atoms. Nelson made his measurement by monitoring the decay of very low polarized Rb. The slow down factor had to be taken into account in these measurements. However, Wagshul and Chupp [53] showed that the final achievable Rb polarization does not depend on the slow down factor. Since we are interested in only the ultimate Rb polarization, we do not consider it here.

[5]See Nelson's thesis[10], equation 5.20-5.27. I should note, this is a very cursory explanation of these molecular interactions. There is a lot of very detailed theory behind all of this that I am sweeping under the rug. The interested reader should look at Chapter 5 of Nelson's thesis in more detail.

approximating the Xe polarization. The time dependence of the polarization of the Xe is given by

$$\frac{\partial \mathcal{P}_{Xe}}{\partial t} = \gamma_{SE}(\overline{\mathcal{P}_{Rb}} - \mathcal{P}_{Xe}) - \Gamma_{Xe}\mathcal{P}_{Xe}. \tag{4.15}$$

In the above equation, Γ_{Xe} is the spin destruction rate of the ^{129}Xe polarization, which is dependent on total gas pressure and composition [61, 11]. The quantity γ_{SE} is the spin-exchange rate between ^{129}Xe and Rb and depends on total gas pressure and composition. For the model to fit the data, our implementation of the model incorporates temperature dependence in the spin-exchange rate. This temperature dependence was reported by Nelson [10], and we use the expression that he determined:

$$\gamma_{SE} = \left(\frac{\mathcal{K}\alpha}{2\hbar x} \frac{[G]_0}{[G]_1} \frac{[G]_1}{[G]} \left\{ 0.358 + \frac{0.648\eta_{85}}{1 + \left(\frac{[G]_1}{[G]}\right)^2} + \frac{0.625\eta_{87}}{1 + \left(\frac{2.25[G]_1}{[G]}\right)^2} \right\} + \langle \sigma_{SE} v \rangle \right) [Rb] \tag{4.16}$$

where $\mathcal{K}$ is the chemical equilibrium coefficient for Rb-Xe molecules; α is the coupling coefficient between the Rb electron and the Xe nuclear spins; the Rabi field parameter $x = \frac{\gamma N}{\alpha}$ (where γ is the coupling coefficient for the interaction between the Rb electron spin and the molecular tumbling angular momentum N); $[G]_0$ and $[G]_1$ are characteristic gas densities that mark the transition between short and long lived molecules and short and very short molecules [10], respectively; $[G]$ is the total gas density; η_{85} and η_{87} are the relative abundances of the two isotopes of Rb; and $\langle \sigma_{SE} v \rangle$ is the velocity averaged spin-exchange cross section. If we use equation (1.4) to attempt to fit the data, we find that the model predicts a temperature maximum to occur around 500 °C, instead of the 140-160 °C where they are actually observed. We extrapolated a strong temperature dependence in $[G]_1$ by fitting the ^{129}Xe spin-exchange $[G]_1$ temperature data reported by Nelson to a power law. The values Nelson reported for $[G]_1$ at various temperatures are shown in Table 4.1. Fitting these points to a power law using the exponent and the leading coefficient as the fit variables, we find the following relationship:

$$[G]_1 = (1.92 \pm 0.09) \text{ amg} \left(\frac{T + 273\ ^\circ C}{413\ ^\circ C} \right)^{(-6\pm1)}. \tag{4.17}$$

We also included the $T^{-\frac{3}{2}}$ dependence of $\mathcal{K}$ and the $T^{\frac{1}{2}}$ dependence of $\langle \sigma_{SE} v \rangle$ assumed by Nelson in his thesis [10]. Specifically, we extract the relationships

Table 4.1. The temperature dependent characteristic density data extracted by Nelson from Rb-^{129}Xe spin-exchange data [10]. We took this data and fit it to a power law to extract equation (4.17).

	120 °C	130 °C	140 °C	150 °C
$[G]_1$ (amagats)	2.42 ± 0.35	2.36 ± 0.34	1.96 ± 0.28	1.57 ± 0.22

$$\frac{\mathcal{K}\alpha}{2\hbar x}\frac{[G]_0}{[G]_1} = (1.16 \pm .016) \times 10^{-15}\ \mathrm{cm}^3/\mathrm{s}\left(\frac{T + 272.15\ ^\circ C}{20 + 272.15\ ^\circ C}\right)^{\frac{-3}{2}}, \tag{4.18}$$

$$\langle \sigma_{SE} v \rangle = (2.2 \pm 2.5) \times 10^{-17}\ \mathrm{cm}^3/\mathrm{s}\left(\frac{T + 272.15\ ^\circ C}{20 + 272.15\ ^\circ C}\right)^{\frac{1}{2}}. \tag{4.19}$$

Notice that equation (4.16) does not contain information about specific gas composition like equation (1.4). Nelson's gas composition was 1% Xe, 1% N_2, and balance He. Our gas composition contained a higher concentration of N_2 that may decrease the actual spin-exchange rate.

In Ruset's thesis [11], equation (1.4) was used instead of equation (4.16). They observed a discrepancies between the behavior of their system and the model, and they note that the model's predictions were probably incorrect above 160 °C because of the failure to include temperature dependence in either spin-exchange or optical pumping rates.

By using the chain rule, we can write

$$\frac{\partial \mathcal{P}_{Xe}}{\partial z} = \frac{\partial \mathcal{P}_{Xe}}{\partial t}\frac{\partial t}{\partial z} = \frac{1}{v_l}[\gamma_{SE}(\overline{\mathcal{P}_{Rb}} - \mathcal{P}_{Xe}) - \Gamma_{Xe}\mathcal{P}_{Xe}] \tag{4.20}$$

where v_l is the linear velocity of the Xe gas flowing through the cell. Following Ruset [11], we can approximate the radial distribution of the v_l as from the Hagen-Poiseuille equation, $v_l(r) = v_{max}\left[1 - \left(\frac{r}{R}\right)^2\right]$. Here, v_{max} is the maximum velocity of the gas at the center of the cell, r is the radial distance from the center of the cell, and R is the radius of the cell. We have assumed a "no slip" condition at the wall, that is, $v_l(R) = 0$. The maximum linear velocity is related to the total standard flow velocity, $\mathcal{F}$ by $v_{max} = \frac{2\mathcal{F}}{A[G]}$, where A is the cross sectional area of the optical pumping cell.

The axial solution to equation (4.20) is solved numerically using Euler's Method for a set of equally spaced points r across the cell in the transverse plane. These solutions are then averaged to approximate the bulk average ^{129}Xe polarization. The step size in the axial direction z is again 1 mm, and in the radial direction it is 0.4 mm.

4.5 Analytical Model

In addition to the numerical model, we developed a simple analytical model to help understand some of the behavior of the system. To develop this model, we assume an optical pumping region split into a heated and unheated region with no transition region (see Figure 4.1). The evolution of the polarization of the ^{129}Xe in the heated region was determined by both spin-exchange and spin-destruction rates. In the unheated region, only spin-destruction determined the evolution of the polarization.

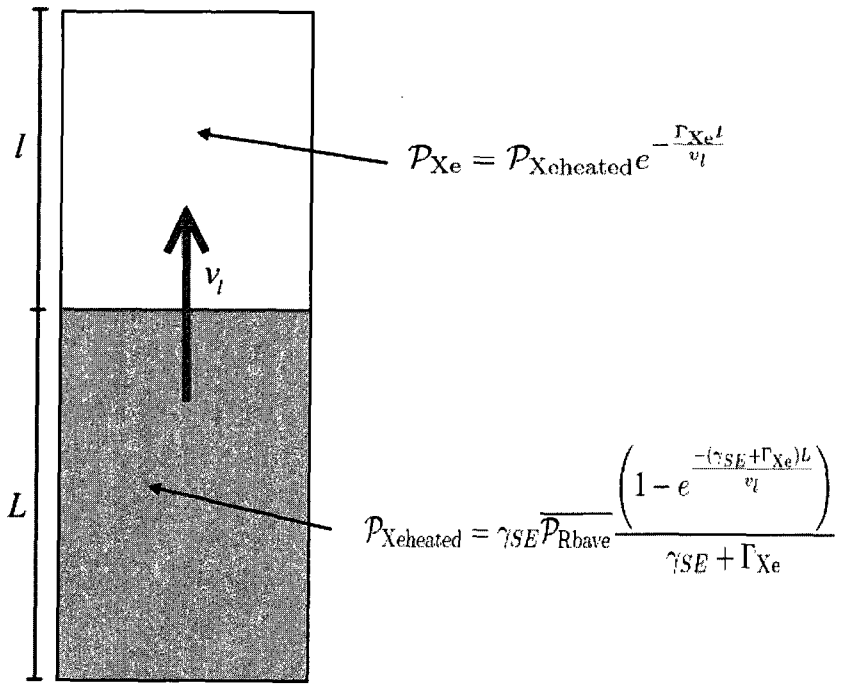

Figure 4.1. The analytical model uses a simplified system to approximate the physics in the flow-through polarizer. Above is a graphic illustrating the simplified system. The bottom portion of the system is governed by equation (4.21), and equation (4.22). The gas mixture propagates with linear velocity v_l from the bottom, heated portion to the upper, unheated portion of the system.

The expression for the polarization of the ^{129}Xe at the end of the heated region is given by:

$$\mathcal{P}_{\mathrm{Xeheated}} = \gamma_{SE} \overline{\mathcal{P}_{\mathrm{Rbave}}} \frac{\left(1 - e^{\frac{-(\gamma_{SE}+\Gamma_{\mathrm{Xe}})L}{v_l}}\right)}{\gamma_{SE} + \Gamma_{\mathrm{Xe}}}, \tag{4.21}$$

where $\overline{\mathcal{P}_{\mathrm{Rbave}}}$ is the assumed uniform Rb polarization in the heated region and L is the total length of the heated region. While traveling through the unheated length, l, of the cell, the acquired polarization, $\mathcal{P}_{\mathrm{Xeheated}}$, will relax by:

$$\mathcal{P}_{\mathrm{Xe}} = \mathcal{P}_{\mathrm{Xeheated}} e^{-\frac{\Gamma_{\mathrm{Xe}} l}{v_l}}. \tag{4.22}$$

Combining equations (4.21) and (4.22), we derive:

$$\mathcal{P}_{\mathrm{Xe}} = \frac{\gamma_{SE} \overline{\mathcal{P}_{\mathrm{Rbave}}}}{\gamma_{SE} + \Gamma_{\mathrm{Xe}}} \left(1 - e^{\frac{-(\gamma_{SE}+\Gamma_{\mathrm{Xe}})L}{v_l}}\right) e^{-\frac{\Gamma_{\mathrm{Xe}} l}{v_l}} \tag{4.23}$$

for the output ^{129}Xe polarization. Unlike the numerical model, we assume linear velocity is uniform across the cell and write $v_l = \frac{\mathcal{F}}{A[G]}$. Substituting this expression in, taking the

derivative of equation (4.23), and setting it equal to zero to solve for $\mathcal{F}$, we obtain an equation for the flow velocity at which maximum polarization occurs:

$$\mathcal{F}_{max} = -\frac{(\gamma_{SE} + \Gamma_{Xe})LA[g]}{\ln\left(\frac{\Gamma_{Xe}l}{L\gamma_{SE}+L\Gamma_{Xe}+\Gamma_{Xe}l}\right)}. \tag{4.24}$$

This relationship helped provide qualitative understanding of the flow dependence of the ^{129}Xe polarization.

We can further attempt to estimate $\overline{\mathcal{P}_{\mathrm{Rbave}}}$ and obtain a complete analytical expression for $\mathcal{P}_{\mathrm{Xe}}$. Recall equation (4.8). Part of the difficulty in solving this equation analytically arises from $\gamma_{opt}(z) = \int_0^\infty \psi(\nu, z)\sigma_s(\nu)d\nu$, and the fact that the functional form $\psi(\nu, z)$ changes as the light travels through the optical pumping region. If we assume that $\psi(\nu, z)$ is given by a Gaussian throughout the optical pumping region, we can integrate to get an expression for γ_{opt}.

Assume the functional form for $\psi(\nu, z)$ is

$$\psi(\nu, z) = \frac{2\Psi(z)\sqrt{\ln 2}}{\sqrt{\pi}\delta_\lambda} e^{\left(\frac{-4(\nu-\nu_0)\ln 2}{\delta_\lambda}\right)}, \tag{4.25}$$

and the functional form for $\sigma_s(\nu)$ is given by equation (4.3). Here, δ_λ is the width of the spectral line and $\Psi(z) = \int_0^\infty \psi(\nu, z)d\nu$, the total photon flux. Integrating these two equations over all ν and using equation (4.4), we find the following relationship between photon flux and optical pumping rate:

$$\gamma_{opt}(z) = \int_0^\infty \psi(\nu, z)\sigma_s(\nu)d\nu \tag{4.26}$$

$$= \frac{r_e c f \sqrt{\pi \ln 2}\,\mathrm{w}(\delta_\lambda, \delta_\sigma)}{\delta_\lambda}\Psi(z), \tag{4.27}$$

where

$$\mathrm{w}(\delta_\lambda, \delta_\sigma) = \mathrm{e}^{\ln 2\left(\frac{\delta_\sigma}{\delta_\lambda}\right)^2}\left(1 - \mathrm{erf}\left(\sqrt{\ln 2}\frac{\delta_\sigma}{\delta_\lambda}\right)\right). \tag{4.28}$$

We can integrate equation (4.8) to obtain an expression with γ_{opt} and $\Psi(z)$:

$$\int \frac{\partial\psi(\nu, z)}{\partial z}d\nu = -[Rb]\frac{\Gamma_{SD}}{\gamma_{opt}(z) + \Gamma_{SD}}\int \psi(\nu, z)\sigma_s\, d\nu \tag{4.29}$$

$$\frac{\partial\Psi(z)}{\partial z} = -[Rb]\gamma_{opt}\frac{\Gamma_{SD}}{\gamma_{opt}(z) + \Gamma_{SD}}. \tag{4.30}$$

Then, use equation (4.27), to put equation (4.30) completely in terms γ_{opt}:

$$\frac{\partial\gamma_{opt}}{\partial z} = -\epsilon[\mathrm{Rb}]\gamma_{opt}\frac{\Gamma_{SD}}{\gamma_{opt}(z) + \Gamma_{SD}}, \tag{4.31}$$

where we've absorbed all the constant terms of (4.27) into ϵ.

We can easily solve equation (4.31) to find the implicit relationship

$$\Gamma_{SD} \ln\left(\frac{\gamma_{opt}}{\gamma_C}\right) + \gamma_{opt} = \epsilon\Gamma_{SD}[\mathrm{Rb}]z, \tag{4.32}$$

where γ_C is a constant determined by the initial photon flux into the optical pumping region. The derivation of equation (4.32) was inspired by Appelt et al. [50].

Using equation (4.9), we can write (4.32) in terms of $\mathcal{P}_{Rb}$:

$$\Gamma_{SD} \ln\left(\frac{\Gamma_{SD}\mathcal{P}_{\mathrm{Rb}}}{(1-\mathcal{P}_{\mathrm{Rb}})\gamma_C}\right) + \frac{\mathcal{P}_{\mathrm{Rb}}}{1-\mathcal{P}_{\mathrm{Rb}}} = \epsilon[\mathrm{Rb}]z. \tag{4.33}$$

One can solve (4.33) for $\mathcal{P}_{\mathrm{Rb}}$ using the special Lambert-W function, W:

$$\mathcal{P}_{Rb} = \frac{\mathrm{W}\left(\frac{\gamma_C e^{-\epsilon[Rb]z}}{\Gamma_{SD}}\right)}{\mathrm{W}\left(\frac{\gamma_C e^{-\epsilon[Rb]z}}{\Gamma_{SD}}\right) - 1} \tag{4.34}$$

To find γ_C, we need to fit the condition $\mathcal{P}_{Rb} = \frac{\gamma_0}{\gamma_0+\Gamma_{SD}}$ at $z = 0$, where γ_0 is the initial optical pumping rate at the top of the heated portion of the cell. It is given by $\frac{\epsilon P_l}{Ah\nu_0}$, where P_l is the initial laser power incident on the optical pumping cell and, h is Plank's constant. Fitting the condition, we find

$$\gamma_C = \gamma_0 e^{\left(\frac{\gamma_0}{\Gamma_{SD}}\right)}. \tag{4.35}$$

We now average equation (4.34) over the heated length of the cell to obtain an expression for $\mathcal{P}_{\mathrm{Rbave}}$:

$$\mathcal{P}_{\mathrm{Rbave}} = \frac{\int_0^\infty \mathcal{P}_{\mathrm{Rb}} dz}{L} \tag{4.36}$$

$$= -\frac{\mathrm{W}\left(\gamma_0 e^{\left(\frac{\gamma_0}{\Gamma_{SD}}\right)} e^{-\epsilon[\mathrm{Rb}]L}\right) - \mathrm{W}\left(\frac{\gamma_0 e^{\left(\frac{\gamma_0}{\Gamma_{SD}}\right)}}{\Gamma_{SD}}\right)}{\epsilon[\mathrm{Rb}]L}. \tag{4.37}$$

One can substitute (4.37) back into equation (4.23) to obtain an analytical expression for the final ^{129}Xe polarization. One may analyze this expression to obtain equations for the temperature, pressure, and Xe partial pressure dependence of the polarizer.

4.6 Unaddressed Effects

There are some physical effects that are known to exist in SEOP setups that were not included in this model. I will present three such effects here. With the exception of the laser heating effect presented in Section 4.6.2, we believe that these effects are negligible.

4.6.1 Rb Nuclear Slow-Down

Polarization and relaxation of Rb is a non-exponential process owed to the strong hyperfine interaction. During optical pumping, the Rb polarization will grow slowly at

low polarization and quickly at high polarizations. That is, the rate of build up of Rb electron spin polarization is dependent on the polarization of the Rb. This phenomenon is the same in relaxation, that is, a highly polarized Rb sample will relax more quickly than a Rb sample at low polarization. Although the time-scale of the polarization and relaxation is not important for calculating the final polarization of the Rb [53], the non-exponential nature of the rates are important for measuring spin destruction rates. It is useful to have a good understanding of this phenomenon when deciphering literature reporting Rb spin destruction rates.

This phenomenon, called Rb nuclear slow-down, can be understood by noting that optical pumping ultimately causes transition between hyperfine levels. At the small magnetic fields used for optical pumping, the hyperfine interaction is strong enough that neither the individual spin eigenkets are good approximations to the wave function of the system. Instead, the total angular momentum eigenket best describes the system. However, most the interaction the atom experiences are communicated through the electron spin, and after these interactions, the Rb electron will recouple with the nucleus and the atom will find itself in a superposition of hyperfine states, changing the expectation value of the total azimuthal spin angular momentum, $\langle F_z \rangle$. The differential equation that describes the the rate change of $\langle F_z \rangle$ is, thus, a function of both $\langle F_z \rangle$ and the electron spin expectation value $\langle S_z \rangle$.

These two expectation values are related, and that relationship can be expressed explicitly if the system is in a spin temperature. This relationship between $\langle F_z \rangle$ and $\langle S_z \rangle$ is called the slow down factor and is defined as [53]:

$$S = \frac{\langle F_z \rangle}{\langle S_z \rangle}. \tag{4.38}$$

This quantity is dependent on the polarization (and, thus, the spin temperature[6]) of the alkali. The expectation values for ^{85}Rb are related to the spin temperature β by

$$\langle F_z(^{85}\mathrm{Rb}) \rangle = \frac{(6\sinh(3\beta) + 8\sinh(2\beta) + 4\sinh(\beta))}{\sum_{F,m} \exp(\beta m)} \tag{4.39}$$

and

$$\langle S_z(^{85}\mathrm{Rb}) \rangle = \frac{\sinh(3\beta)}{\sum_{F,m} \exp(\beta m)}, \tag{4.40}$$

where the sums span the total angular momentum, $F = 3, 2$, and the associated azimuthal angular momentum, m. The expression for ^{87}Rb are similar:

$$\langle F_z(^{87}\mathrm{Rb}) \rangle = \frac{(4\sinh(2\beta) + 4\sinh(\beta))}{\sum_{F,m} \exp(\beta m)} \tag{4.41}$$

[6]The relationship between the polarization and the spin temperature is $\mathcal{P}_{\mathrm{Rb}} = \tanh\left(\frac{\beta}{2}\right)$ [43].

and

$$\langle S_z(^{87}\mathrm{Rb})\rangle = \frac{\sinh(2\beta)}{\sum_{F,m}\exp(\beta m)}, \tag{4.42}$$

where now $F = 1, 2$.

This slow-down factor effects the Rb polarization by slowing the build up of electron polarization. The expression that describes this build up is [53]

$$\mathcal{P}_{\mathrm{Rb}}(t) = \frac{\gamma_{opt}}{\gamma_{opt} + \Gamma_{SD}}\left(1 - \mathrm{e}^{-\left(\frac{\gamma_{opt}+\Gamma_{SD}}{S}\right)t}\right). \tag{4.43}$$

Note that the slow down factor does not affect the ultimate Rb polarization.

The slow down factor is frequently expressed in terms of the "paramagnetic constant". In Happer et al. [62], the authors liken spin-exchange optical pumping to an RC network. In the model, charge represents the spin angular momentum and voltage represents spin polarization. The storage of spin angular momentum in the Rb atoms and the noble gas nuclei are represented by charge being stored on capacitors. The authors note that the capacitance is proportional to the quantity $\langle \hat{K}^2 - K_z^2\rangle$, where K represents the spin operator of either the alkali or noble gas. For spin $\frac{1}{2}$, this quantity is a constant, $\frac{1}{2}$. For spin $> \frac{1}{2}$, this quantity is polarization dependent. The authors compare the spin $\frac{1}{2}$ to an "air-gap" capacitor and spin $> \frac{1}{2}$ to a capacitor with a dielectric material between the plates. They define the "paramagnetic constant" as

$$\epsilon(K, \beta) = 2\langle \hat{K}^2 - K_z^2\rangle. \tag{4.44}$$

In the limit of very high polarization, they find

$$\epsilon(K, \infty) = 2K, \tag{4.45}$$

and in the limit of very low polarization,

$$\epsilon(K, 0) = \frac{4}{3}K(K+1). \tag{4.46}$$

The nuclear slow-down factor and ϵ are related by

$$S = 1 + \epsilon(K, \beta). \tag{4.47}$$

4.6.2 Laser Heating Affects

High-powered diode laser arrays used for optical pumping deposit large amounts of energy into the system. Much of the absorbed optical energy is converted into thermal energy that can drive strong temperature gradients and convection in optical pumping systems. The energy conversion occurs when N_2 collides with excited Rb and nonradiatively relaxes it. The N_2 absorbs the energy into vibrational and rotational modes of

the molecule, and then thermalizes with the sample through collisions with other buffer gases.

Walter et al. [63] have done studies of energy transport in ^{3}He optical pumping cells using Raman scattering and found that for laser powers of more than a few watts, convection intensely affects the temperature gradients and energy transport in the cell. They also found that the internal gas temperature can be 100's °C higher than the cell wall temperature. They measured a gas temperature in the center of the optical pumping cell as high as ≈350 °C for 15 W of absorbed light.

The group observed a linear dependence of the gas temperature as a function of laser absorption until the laser absorption reached ≈4 W. At this point, the dependence deviated below the predict line, and the deviation became more pronounced for increasing laser absorption. They interpreted this deviation to be the onset of convective energy transport in the cell.

Fink et al. [51] have included convection and laser heating in their spin-exchange optical pumping simulations. Their simulations indicate that convection can cause both transverse and longitudinal flow depending the degree of optical absorption in the cell. For situations where the laser penetrates the entire cell and the resulting ^{129}Xe polarization is relatively uniform, the dominate convection currents appear to rotate around the axis of the cell. When the laser does not seem to penetrate the whole cell and, thus, there exist strong ^{129}Xe polarization gradients in the cell, the circulation appears to be along the axis of the cell. It should be noted, however, that Fink et al. simulated a Driehuys like polarizer. To date, I am not aware of any simulation for polarizers like that described by Ruset et al.[15] that includes laser heating or convection.

4.6.3 Skew Light Affects

When the optical pumping light propagates at an angle to the applied external field, the polarization of the Rb will suffer. The optical pumping light defines the azimuthal axis for the electron spins, and if this is at an angle to the external field, the polarized spins will precess around that field resulting in a lower time averaged polarization. The Rb will never achieve full polarization and is less transparent to incident light, thus increasing the attenuation of the light through the sample.

Chann et al. [64] demonstrated that the attenuation of light propagation through an optical pumping sample at angle θ to the external field is

$$\frac{\partial \Psi}{\partial \xi} = -[Rb]\gamma_{opt}\frac{\gamma_{opt}\sin^2(\theta) + \Gamma_{SD}}{\gamma_{opt}(z) + \Gamma_{SD}}, \tag{4.48}$$

where ξ is the direction along which the light propagates. The increase in light absorption increases as $\sin^2(\theta)$, and small deviations of the parallelity of the light and magnetic field

can seriously affect the bulk average alkali polarization.

It should be noted that equation (4.48) reduces to equation (4.30) when $\theta = 0$.

4.7 Model Results and Discussion

The trends in the numerical model and the experimental results agree well for most parameters (see Figure 4.2 and Figure 4.3). We were able to reproduce the observed maxima for both the temperature and total flow rate Xe polarization dependencies. The model well predicted the relatively flat pressure dependence with a possible slight fall off at larger polarization observed in the ^{129}Xe polarization.

We attempted to fit the model to the observed ^{129}Xe polarizations produced by Polarizer 2 by varying the parameters. In order to reproduce the observed temperature maximum, we had to include the temperature dependences of spin-exchange, which was not included in Ruset's original model[11]. We also had to adjust the ^{129}Xe spin destruction rate so that the total flow maximum fit the observed maximum (see equation (4.24)). With these modifications, the model trends reproduced the observed trends. However, the actual predicted polarization numbers were higher than those observed by up to a factor of two. In order to accurately predict the observed polarization, we had to multiply the spin-exchange cross section by a factor of 0.6, that is, decrease the spin-exchange rate by 40%. This discrepancy appears to be reasonable within the error of the temperature dependent spin-exchange rate extracted from the information provided by Nelson and may also be due to differences in gas composition.

One may suggest that a more reasonable explanation for the discrepancy between observed ^{129}Xe polarization numbers and those predicted by the model is due to an overestimate of the incident photon flux on the optical pumping cell. Indeed, we found that lowering the photon flux by a factor of two did result in a better agreement between the predicted and measured polarizations. Lowering the photon flux also produced better fits of the slopes in the temperature dependence. Unfortunately, assuming a lower photon flux substantially decreases the model's predictions of the Rb polarizations. Our measurements of the Rb polarizations indicate that our photon flux estimate was reasonable.

There are two major discrepancies between the observed and modeled ^{129}Xe polarization data. The temperature dependence before the maximum appears to fall off slower than modeled, and the observed Xe partial pressure dependence does not follow the predicted curve for very low Xe partial pressures.

Like ^{129}Xe, the predicted and observed ^{85}Rb polarizations somewhat agree, but there are four major discrepancies of interest.

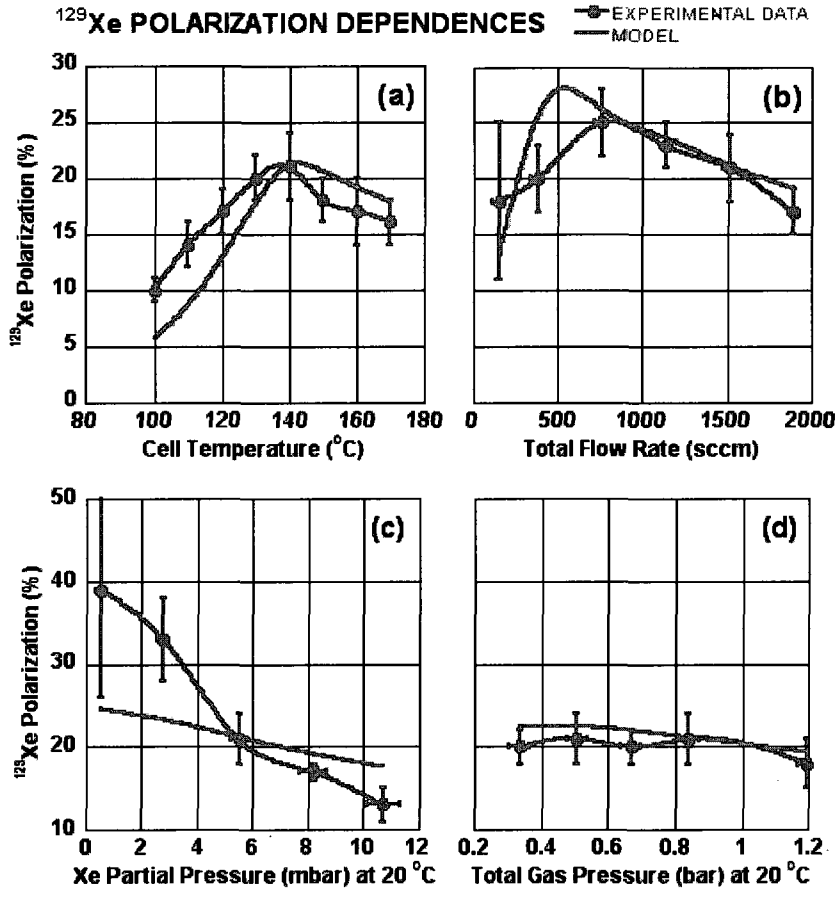

Figure 4.2. Comparison of experimental data on output $\mathcal{P}_{\mathrm{Xe}}$ to our numerical model as a function of: (a) cell temperature, (b) total gas flow rate, (c) Xe partial pressure, and (d) total gas pressure. All pressures are referenced to 20 °C. Unless the parameter was varied, the standard operating conditions under which the data were taken were as follows: gas mixture flows: He:N_2:Xe = 1000:500:10 sccm, total gas pressure: 0.83 bar, oven temperature: 140 °C. The model curves reflect an adjustment of the spin-exchange rate by a factor of 0.6 to better match the lower observed ^{129}Xe polarization.

First, the measured ^{85}Rb polarization falls off too slowly as a function of temperature (Fig. 4.3.a). This could easily be explained by an incorrect estimate of the Rb number density based on the temperature. The number density estimates were made based on the vapor pressure curves reported by Killian [52]. Deviations from these values have been observed from heating due to the laser [49, 65] and may be further complicated by convection and turbulence. It is also possible that the Rb mixing region is not adequate to fully saturate the gas mixture to the Rb equilibrium vapor pressure. This may also explain the slight discrepancies in the ^{129}Xe polarizations as a function of temperature at lower temperatures.

Second, the ^{85}Rb polarization decreases faster than predicted for the highest Xe concentrations (Fig. 4.3.b). This may be due to an incorrect estimate of the Xe-Rb molecular spin destruction rate. This rate is dependent on gas composition and, to date, has only been measured for a single composition [55]. It can only be poorly extrapolated from this measurement to other gas compositions, and this simple extrapolation used for the numerical model may be inadequate. This may also be the partial explanation for the discrepancy in the Xe partial pressure dependence between the observed and modeled ^{129}Xe polarizations.

Third, the ^{85}Rb polarizations showed a slight but noticeable dependence on total flow rate (Fig. 4.3.d). The numerical model predicted no Rb polarization dependence on the total flow rate of the gas mixture through the optical pumping cell. We observed that slower flow rates gave rise to a slightly higher ^{85}Rb polarization. This may be due to rapidly moving gas pushing the Rb vapor higher in the optical pumping cell and absorbing light above the heated volume of the cell. We have observed macroscopic Rb droplets circulating in the unheated portion of the cell. It may be that these droplets are indicative of higher Rb number densities in the unheated portion of the cell than we estimated.

Fourth, we note two depressions in the ^{85}Rb polarization profile. We consistently observe these depressions at the very top of the heated volume, 7 cm depth, and half way into the heated volume, 25 cm depth. The depression at 7 cm is likely due to an excess of Rb metal condensed on the walls in the water cooled volume. Appelt et. al [50] noted a similar depression near excess Rb and ascribed it to an enhanced evaporation of the Rb. The depression at 25 cm cannot be similarly explained. Visual inspection of the area does not reveal excess plated Rb relative to areas near it. Unfortunately, a qualitative theory has yet to be formulated to account for this effect. We intend to study other optical pumping cells to determine if this effect is unique to the current cell.

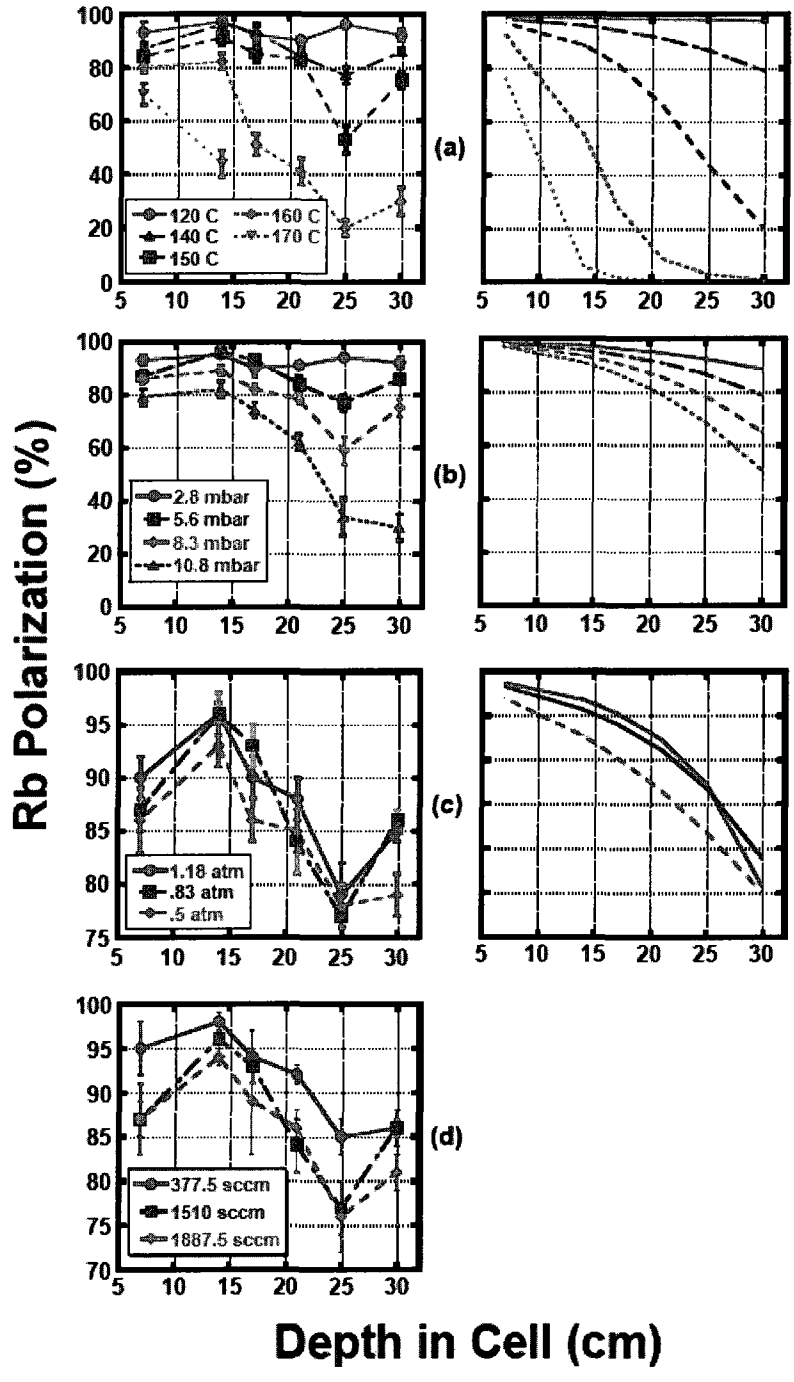

Figure 4.3. Comparison of experimental data to our numerical model for Rb polarization vs. cell depth below the top of the oven. The varied parameters are: (a) cell temperature, (b) Xe partial pressure, (c) total gas pressure, (d) total gas flow rate. The standard operating conditions are identical to those described in Fig. 4.2.

4.8 Conclusion

The model does an excellent job of predicting the Rb and ^{129}Xe polarization in the flow-though polarizer. In order to accurately reproduce the trends in the model, the temperature dependence of the spin-exchange term had to be incorporated. Because the predicted polarization numbers were higher than the observed value, we also had to reduce the spin-exchange rate by 40% in order to reproduce the the polarization numbers with fair agreement. This lower-than-predicted result was not due to low Rb polarization number, because those measurement were either agreed with or were higher than the prediction of the model.

The few areas were the model does not agree well with the measured ^{129}Xe polarization point towards incorrect assumptions regarding the [Rb] and the Xe-Rb spin destruction rate. Comparison with the ^{85}Rb polarization measurements seem to confirm these conclusions.

Measurements of the Rb number density, ^{129}Xe polarization profile, and transverse Rb polarization profile will provide further insight into the inadequacies of the model and provide useful information to better optimize the optical pumping cell.

CHAPTER 5

XENON-PROTEIN INTERACTIONS IN BOVINE PANCREATIC TRYPSIN INHIBITOR

5.1 Introduction

We have, thus far, examined the details of the performance of a novel ^{129}Xe flow-through polarizer and analyzed the performance to better understand the relevant physics of the system. We will now briefly explore an application of this polarizer to make advances in a field of biology to illustrate the utility of this system. In the following experiment, I will describe measuring the chemical shift of ^{129}Xe in Bovine Pancreatic Trypsin Inhibitor (BPTI) to infer information about the structure and conformation of the protein and some of its mutants. The first studies of Xe binding to protein were done by Schoenborn et al. [66, 67], who examined Xe binding to myoglobin and hemoglobin using x-ray crystallography. The first NMR studies of Xe binding to protein solutions were performed by Tilton and Kuntz in 1982 also using myoglobin and hemoglobin [68]. More recently, hyperpolarized ^{129}Xe has been used to enhance the NMR sensitivity to proteins [24] and amino acids [69]. Lowery et al. demonstrated that laser polarized ^{129}Xe was sensitive to the conformation of a chemotaxis protein [25].

Xe is known to bind to proteins both specifically and nonspecifically. Specific binding occurs at hydrophobic cavities and is mediated by Debye and London forces [70]. Binding to these sites may be inhibited by the conformation of the protein (the particular spacial arrangement of the constituent amino acids), thus Xe can be used to probe some of the conformations of proteins. One can observe a change in the NMR frequency of the Xe upon binding to these sites.

Nonspecific binding is not associated with any particular location on the protein and is usually comparatively weaker. These interactions will also affect the NMR frequency in a non-negligible way, and for precise measurements of the relevant quantities, these interactions need to be considered. It should be noted that unlike the previous experiments described in this thesis, the Xe in the following experiments was dissolved in a protein/buffer solution. Unless explicitly stated otherwise, all reactions take place in solution and all quantities are understood to be the dissolved phase quantities.

5.1.1 Bovine Pancreatic Trypsin Inhibitor

BPTI represents a very interesting protein system to investigate using ^{129}Xe. In their review of the protein, Ascenzi et al. [71] outline the importance of BPTI. It is a good test system for answering biological questions as it is a thoroughly studied protein, and much structural and dynamical information is known. In addition to trypsin, it inhibits a number of important enzymes such as chymotrypsin and elastase-like serine-proteases. Finally, BPTI has been demonstrated to be useful in a clinical setting associated with hyperfibrinolysis.

In the present work, we will examine the behavior of BPTI found in its natural state (wild type) and several modified structures (mutants). Previous work has provided some structural and dynamical information about the wild type and mutant proteins [72, 73, 74, 75, 76, 77, 78]. The wild type structure does not appear to have any sites that are usually associated with Xe binding. However, the mutants in the present study have been shown to contain cavities of the type that are associated with Xe binding [79]. Of the three mutants studied, one mutant, Y35G, is flexible and undergoes conformational changes [77]. The conformational changes occur on the order of microseconds and involve the region that binds to trypsin. When bound to trypsin, x-ray crystallography has shown that the mutant rigidifies into a conformation resembling the wild type and the other mutants [80]. However, it is not known what fraction of the mutant exists in this conformation when the protein is unbound.

5.1.2 Xenon Chemical Exchange

As mentioned previously, Xe is known to interact with many proteins and this interaction can be studied using NMR. Cherubini and Bifone describe the particulars of this interaction in their review article [70]. Strong interactions between the Xe and the protein occur when the Xe binds to hydrophobic cavities (spacial voids in the structure of the protein). Xe binds to the proteins due to the large polarizability of its electron cloud.

Xe can also bind to protein nonspecifically. In this case, there is no specific hydrophobic cavity to which the Xe binds. Rather, the Xe comes into close contact with some area of the protein and forms a very weak van der Waals bond.

The temporary nature of these bonds, both specific and nonspecific, lead to chemical exchange between bound and unbound state Xe atoms, which can be expressed as follows:

$$\mathrm{Xe} + \mathrm{Protein} \underset{k_r}{\overset{k_f}{\rightleftharpoons}} \mathrm{XeProtein}, \tag{5.1}$$

where k_f and k_r are the forward and reverse reaction rates. The affinity or association constant, is related to the reaction rates by

$$\mathcal{K}_a = \frac{k_f}{k_r} = \frac{[\text{XeProtein}]}{[\text{Xe}][\text{Protein}]}, \tag{5.2}$$

where the bracketed quantities are understood to be the equilibrium concentrations. This quantity is related to how strongly the Xe in bound to a site in the protein. Hydrophobic cavity affinities for Xe are typically measured in 10's M^{-1}. Nonspecific binding affinities are much smaller. The theory of the effects of chemical exchange in NMR experiments is well studied, and in the following discussion of the topic, I will follow a modification of the review of Bain [81]. In order to derive a set of equations that describe the effects of chemical exchange, we must first make an assumption on the relationship between the concentration of a species and the magnetization due to that species. We assume

$$\vec{M^C} = \vec{m}[C], \tag{5.3}$$

where $\vec{M^C}$ is the bulk magnetization due to species C, and $\vec{m}$ is the magnetic movement of the species. It follows that the time derivative of the bulk magnetization is

$$\frac{\partial \vec{M^C}}{\partial t} = [C]\frac{\partial \vec{m}}{\partial t} + \vec{m}\frac{\partial [C]}{\partial t}. \tag{5.4}$$

For pulsed NMR experiments, we are interested in the evolution of the magnetization in the plane transverse to the applied field. Bloch's equations for the plane perpendicular to an applied field are [47]

$$\frac{\partial m_x}{\partial t} = \gamma m_y H_z - \frac{m_x}{T_2} \tag{5.5}$$

and

$$\frac{\partial m_y}{\partial t} = -\gamma m_x H_z - \frac{m_y}{T_2}, \tag{5.6}$$

where γ is the gyromagnetic ratio, H_z is the applied magnetic field, and T_2 is the transverse relaxation time. Using equation (5.4), we can write

$$\frac{\partial M_x^C}{\partial t} = [C](\gamma m_y H_z - \frac{m_x}{T_2}) + m_x\frac{\partial [C]}{\partial t} \tag{5.7}$$

and

$$\frac{\partial M_y^C}{\partial t} = [C](-\gamma m_x H_z - \frac{m_y}{T_2}) + m_y\frac{\partial [C]}{\partial t}. \tag{5.8}$$

Generally, one defines the quantity $M^C = M_x^C + iM_y^C$ and rewrites equations (5.7) and (5.8) into one equation:

$$\frac{\partial M^C}{\partial t} = \left[-i\gamma M^C H_z - \frac{M^C}{T_2}\right] + (m_x + im_y)\frac{\partial [C]}{\partial t}. \tag{5.9}$$

To progress further, we need to consider the particulars of the chemical exchange reaction of interest. The time derivative of concentrations of the 2 solution-phase Xe species are related to the forward and reverse reaction rates by

$$\frac{\partial [\text{Xe}]}{\partial t} = -k_f[\text{Xe}][\text{Protein}] + k_r[\text{XeProtein}] \tag{5.10}$$

and

$$\frac{\partial[\text{XeProtein}]}{\partial t} = k_f[\text{Xe}][\text{Protein}] - k_r[\text{XeProtein}]. \tag{5.11}$$

Using equation (5.9) with equation (5.10), we derive

$$\frac{\partial M^{\text{Xe}}}{\partial t} = (-i\omega_0 M^{\text{Xe}} - \frac{M^{\text{Xe}}}{T_2}) - M^{\text{Xe}} k_f[\text{Protein}] + k_r M^{\text{XeProtein}}, \tag{5.12}$$

where we have used equation (5.3) to write $M^{\text{Xe}} = (m_x + im_y)[\text{Xe}]$ and $M^{\text{XeProtein}} = (m_x + im_y)[\text{XeProtein}]$, and we have also used $\omega_0 = \gamma H_z$. Similarly, we can write

$$\frac{\partial M^{\text{XeProtein}}}{\partial t} = \left[-i(\omega_0 + \delta)M^{\text{XeProtein}} - \frac{M^{\text{XeProtein}}}{T_2}\right] + M^{\text{Xe}} k_f[\text{Protein}] - k_r M^{\text{XeProtein}}, \tag{5.13}$$

where we have assume that Xe bound to the protein precesses at a frequency that differs from the unbound species by δ. Equation (5.12) and (5.13) are the base equations for understanding the behavior of our system. If one solves these coupled differential equations and Fourier transforms the solutions, one obtains a theoretical NMR spectrum.

Numerical analysis of these equations reveals several important features. First, if $k_f, k_r << \delta$ then we observe two separate resonant peaks in the NMR spectrum. This is called the slow exchange region because it occurs when the exchange between the sits is slow on the NMR time scale. As we increase k_f and k_r, the two peaks merge into a single, broad resonant peak. If we further increase the reaction rates so that $k_f, k_r >> \delta$, which is called the fast exchange region, the single peak will narrow.

Second, in the fast exchange region, if we increase [Protein], the resonant peak will shift closer to the resonant frequency of the bound species, $\omega_0 + \delta$. Conversely, if we reduce [Protein], the resonant peak will shift toward the resonant frequency of the unbound species, ω_0. Physically, concentrating the protein drives the equilibrium further to the bound state species. Thus, a greater fraction of the NMR response comes from the bound state species.

Finally, in the limit of small $\mathcal{K}_a$ and low [Protein], the degree of the shift of the fast exchange resonant line away ω_0 is linearly related to [Protein]. My numerical analysis shows that the slope of that linear relationship is dependent on k_f, k_r, and δ. Others have shown that the slope (usually denoted α) is given by $\alpha = \mathcal{K}_a\delta$ [71]. Previous studies suggest that typical δ's are 1-10's ppm away from ω_0 [82, 24, 25].

Although this relationship is linear in the limit of low [Protein], one can observe deviations from linearity at higher [Protein]. I will derive the relationship between observed chemical shift δ_{obs} in terms of the total protein concentration $[\text{Protein}]_{\text{tot}}$ and

the dissolved Xe concentration [Xe]. [1] The following derivation assumes the existence of only a single, specific binding site.

Following Rubin et al. [24], we write

$$\delta_{\text{obs}} = \delta \frac{[\text{XeProtein}]}{[\text{Xe}]_{\text{tot}}} \tag{5.14}$$

$$= \delta \frac{[\text{XeProtein}]}{[\text{XeProtein}] + [\text{Xe}]}, \tag{5.15}$$

where $[\text{Xe}]_{\text{tot}} = [\text{XeProtein}] + [\text{Xe}]$ is the total Xe concentration in solution.

We can then use (5.2) and write

$$[\text{XeProtein}] = \mathcal{K}_a[\text{Xe}][\text{Protein}] \tag{5.16}$$

$$= \mathcal{K}_a[\text{Xe}]([\text{Protein}]_{\text{tot}} - [\text{XeProtein}]) \tag{5.17}$$

Solving equation (5.17) for [XeProtein] and substituting into Eq. (5.15), we obtain

$$\delta_{\text{obs}} = \frac{\delta \mathcal{K}_a[\text{Protein}]_{\text{tot}}}{1 + \mathcal{K}_a([\text{Xe}] + [\text{Protein}]_{\text{tot}})} \tag{5.18}$$

Eq. (5.18) describes the observed chemical shift of the ^{129}Xe resonance in terms of the two concentrations we can measure, [Xe] and $[\text{Protein}]_{\text{tot}}$. We can measure $[\text{Protein}]_{\text{tot}}$ using the absorption properties of BPTI in solution, and we can measure [Xe] using Henry's law for solubility of Xe. The ability to make the [Xe] measurement using Henry's law assumes a dilute mixture of BPTI. If either [Xe] or $[\text{Protein}]_{\text{tot}}$ become too concentrated, Henry's law is no longer valid because Xe in the gas phase is no longer in equilibrium with just water. The equilibrium coefficients of gas phase Xe exchanging with Xe bound to BPTI become important in the limit of very high protein concentrations.

In the limit that $\mathcal{K}_a[\text{Xe}] << \mathcal{K}_a[\text{Protein}]_{\text{tot}}$, Eq. (5.18) reduces to

$$\delta_{\text{obs}} = \delta \frac{\mathcal{K}_a[\text{Protein}]}{\mathcal{K}_a[\text{Protein}] + 1}. \tag{5.19}$$

For all of the experiments described here, we are at least in this limit because of the extremely small Xe concentrations used.

Clearly, in the limit of $\mathcal{K}_a[\text{Protein}] << 1$, Eq. (5.19) describes a linear relationship between the protein concentration and the observed chemical shift. However, at higher protein concentrations, the chemical shift behavior will saturate such that it is never larger than δ. If we do not observe this saturation behavior, we can put lower bounds on δ and upper bounds on $\mathcal{K}_a$.

To handle multiple binding sites and nonspecific binding, one can rewrite Eq. (5.15) as

[1] I have to acknowledge Zayd Ma at this point for being the impetus for this calculation.

$$\delta_{\text{obs}} = \sum_i \delta_i \frac{[\text{XeProtein}]_i}{[\text{Xe}] + \sum_j [\text{XeProtein}]_j}, \tag{5.20}$$

where i, j index the specific binding sites and the nonspecific binding sites, and δ_i is the chemical shift associated with the binding at each site i. Association constants $\mathcal{K}_a(i) = \frac{[\text{XeProtein}]_i}{[\text{Xe}][\text{Protein}]}$ need to be defined for each binding site. The nonspecific binding sites can be approximated as a single specific binding site with an effective association constant and chemical shift.

5.2 Experimental Setup

The polarizer was run in continuous flow-through mode during the course of the relevant experiments, and it delivered very small concentrations of highly polarized ^{129}Xe to the protein samples. To the best of my knowledge, this type of experiment has never been attempted with Xe concentrations as low as those used in the present experiment.

We made a brief attempt to accumulate a large quantity ($\approx$1 L) of pure, hyperpolarized Xe for this experiment by cryogenically freezing the Xe after polarization. We revolitalized the Xe after 2 hours of accumulation and admitted the gas into an NMR tube sealed with a septum. After introducing the hyperpolarized Xe, we agitated the cell to mix the Xe into the protein solution already in the cell. We then placed the NMR tube in the probe and acquired a spectrum. However, the sensitivity proved to be less than that of a low concentration, continuous flow experiment because of the ability to average the Free Induction Decays (FIDs)in a continuous flow experiment. We also found that the chemical shift was very inconsistent using the above described method, probably because the sample temperature did not equilibrate with the probe temperature.

5.2.1 Polarizer Setup

We found that it was advantageous to run the polarizer under conditions that had not been previously explored for this experiment. Thus, we do not know the precise polarization of the ^{129}Xe. We used a relatively rich mixture of Xe with a gas mixture ratio of N_2:Xe of 500:10 sccm. No Helium was used because of its propensity to evaporate the protein solution.

We used an oven operating temperature of 140 °C because it had been established as an ideal operating temperature in the previously described characterization (Figure 2.7). We did not reoptimize the temperature for the new flow conditions and gas composition because the ^{129}Xe polarization was adequate for the experiments.

Further, we replaced the optical pumping cell for the protein experiments. All of the previous characterizations of Polarizer 2 were done using the cell designated GGPC3. For

the protein experiments, a new cell designated GGPC4 was used.

Finally, the pressure inside the optical pumping cell was not regulated by the pressure regulator. Instead, the system pressure was set by the resistance of the Non-Bubbling Xe Delivery Device (refer to Section 5.2.2). For all the described experiments, the pressure in the cell was measured to be between 3 and 4 psig (1.04 atm to 1.11 atm)[2]. This corresponds to the Xe partial pressure of 0.021 to .022 atm. Assuming the usually quoted linear solubility of Xe with respect to pressure of 4.37 mM/atm [82], the Xe concentration for these experiments was between 92 μM and 96 μM.

5.2.2 Non-Bubbling Xe Delivery Device

To observe the Xe interaction with BPTI using NMR, the Xe needs to be dissolved into the protein solution. In order to obtain high resolution NMR spectra, there can be no bubbles in the solution during data acquisition. Bubbles cause changes in the magnetic susceptibility and thus inhomogeneities in the magnetic field. Some groups have dissolved Xe into solution by bubbling the Xe in the liquid and stopping the Xe bubbling just before data acquisition [83]. In the case of protein solutions, this is less effective because the solutions tends to form standing foams that can take minutes to dissipate, during which time the ^{129}Xe will relax.

In order to make ^{129}Xe measurements in BPTI solution, we built a Non-Bubbling Xe Delivery Device (NBXeDD) like that described by Baumer et al. [84]. The device employed a custom built NMR tube that contained a microporous membrane bundle. The NMR tube was built from a standard 10 mm, thin-walled NMR tube from Wilmad. An open bottomed bowl was attached to the top of the NMR tube to accommodate the necessary fitting to connect the membranes to the polarizer and maintain a reasonable seal of the NMR tube (see Figure 5.1).

The microporous membrane bundle was constructed using 60 CELGARD® X30-240 fibers. These fibers had an OD of 300 μm, an ID of 240 μm, and an average pore size of 0.03 μm. The bundle was split in half so that 30 fibers serve as a gas inlet and 30 as a gas outlet. At the bottom, these bundles were epoxied into a 1/4" PFA tube that was completely sealed on the opposite end. The PFA tube allowed the bundle to reverse direction without bending the membrane bundle. At the top of the inlet and outlet bundles, the membranes were epoxied to #12 Teflon® spaghetti tubes, and the spaghetti tubes passed through a two hole rubber stopper. The rubber stopper sealed the top of the NMR tube to prevent exchange of air and allow for higher than atmospheric pressures in the NMR tube. Two short lengths of either 1/4" Polyflow® or Tygon® tubing shimmed

[2]The absolute pressure at the University of Utah is about 12.3 psia.

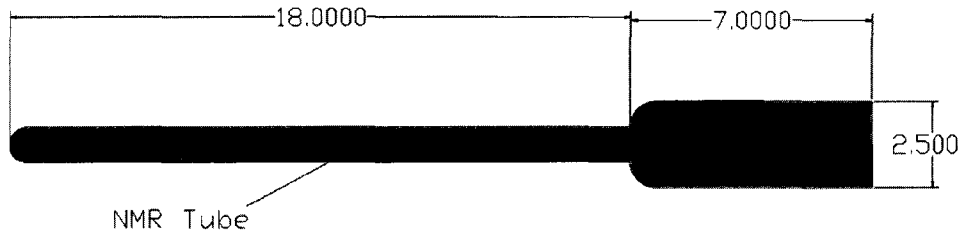

Figure 5.1. A schematic of the modified NMR tube used to house the Non-Bubbling Xe Delivery Device. The modified tube used a standard, 10 mm NMR tube from Wilmad connected to a bowl. The bowl accommodated the rubber stopper used to seal the modified tube. All dimensions in the schematic are in cm.

the holes in the rubber stopper to provide a good seal around the spaghetti tubes. A picture of the entire device is in Figure 5.2.

Several other connections linked the NBXeDD to the polarizer. An ≈1 m length of 1/4" Tygon® tubing was inserted into one of the holes in the rubber stopper. We found the Tygon® tubing to rubber connection sealed sufficiently and did not need further reinforcement. The Tygon® provided a flexible link between the NBXeDD and the other connecting tubing. The Tygon® was connected to ≈10 m of 1/4" stiff PFA tubing via a 1/4"-1/4" UltraTorr brass vacuum fitting. The PFA tubing connected to the polarizer.

During the experiment, hyperpolarized ^{129}Xe constantly flowed to the NBXeDD. This constant flow completely refreshed the hyperpolarized ^{129}Xe in solution on a time scale of 10's of seconds. We believe that the continuous flow also prevented contaminate gas, such as O_2, from entering the solution and reducing the ^{129}Xe relaxation time.

5.2.3 NMR Facilities

The NMR facilities in the Department of Physics and Astronomy were not adequate to obtain the high resolution (better than 1 ppm) required to differentiate between the bound and unbound ^{129}Xe species. Thus, we used the faculties at the David Grant NMR facility housed in the Department of Chemistry to measure the shift. Specifically, we used a 500 MHz Varian system with a BB-500 10 mm probe. The stability of the reference frequency in the spectrometer were important for the experiment, and it had a stability of better than 0.2 ppm drift per day. All ^{129}Xe spectrum were referenced to the transmitter excitation frequency (138.2819581 MHz).

In order to maintain field stability, the spectrometer employed a feedback loop locked

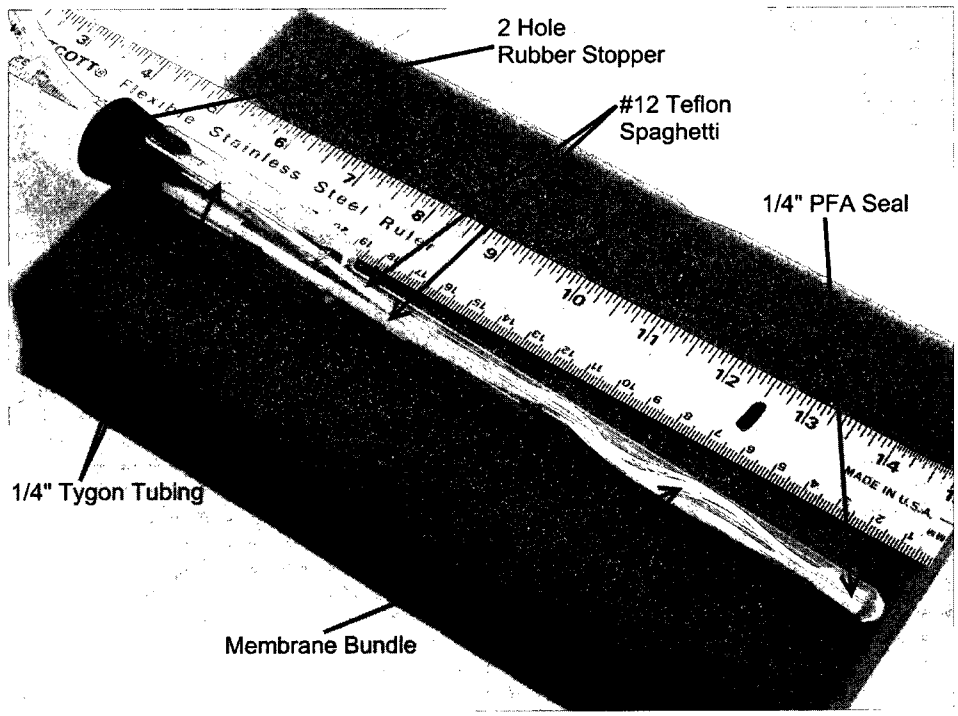

Figure 5.2. A picture of the Non-Bubbling Xe Delivery Device. The gas mixture enters through tube on Tygon® tubing on the right. The mixture passes through the rubber stopper in the #12 Teflon® tube and then flows into the CELGARD® membrane tubes. In the membrane tubes, the Xe gas mixture exchanged with gas in the solution without forming any bubbles. The gas reversed direction at the bottom of the bundle in the 1/4" PFA tube. It traveled back up through the second membrane bundle, into the Teflon tubing, and out of the NMR tube. The Tygon® tubing around the Teflon® tubing at the rubber stopper provided a good seal to prevent gas from leaking out of the NMR tube through the holes in the stopper.

to the NMR resonance of deuterium. The loop attempted to maintain zero phase difference between the spectrometers reference and the deuterium NMR signal. The loop adjusted the current through a set of zero order shim coils to maintain the lock.

The probe could be temperature controlled, and we kept the sample at $\approx$2 °C for the experiment with a fluctuation of only 0.1 °C. We operated at a reduced temperature because we found that the constant gas flow into and over the protein solution would promote the vaporization of the solution. The lower temperature reduced the rate of vaporization of the solution.

5.3 Experimental Method

All of the proteins used in this experiment were dissolved in a 25 mM phosphate buffer solution with 20% D_2O. The D_2O provided the deuterium to which the spectrometer could lock. The phosphate buffer maintained the pH of the solution at 6.7 because we found that changes in the pH affected the chemical shift properties of ^{129}Xe and the properties of the protein. After dissolution, we processed the protein solution using gel-permeation chromatograph to remove the low molecular weight impurities in the solution.

Before each experiment, we cleaned both the NMR tube and the membrane bundle. Both the tube and the bundle were rinsed with DI water three times and then the NMR tube was dried with N_2. The rinsing prevented contamination of the next sample from previous samples and the through drying assured that the concentration of the sample did not change when it was introduced into the NMR tube.

Each sample was carefully equilibrated with the gas mixture and the temperature to assure reproducibility of the chemical shift. After the sample was introduced to the NBXeDD, we flowed N_2 from the polarizer at 500 sccm into the NBXeDD to check that there was no bubble formation and to displace the air in solution. Next, for 10 minutes a mixture of Xe and N_2 flowed into the NBXeDD to saturate the solution with hyperpolarized ^{129}Xe. During the gas saturation process (with either N_2 or N_2 and Xe), the NBXeDD was in the chilled probe for 15 to 20 minutes to allow the solution temperature to drop to the temperature of the probe.

The typical pulse sequence consisted of 100 averages spaced by 10 seconds. The 10 second delay between averages allowed the solution time to refresh with hyperpolarized ^{129}Xe. After 100 averages, the typical signal to noise ratio was 80-150.

A phosphate buffer solution with no protein was first measured to establish a baseline for the chemical shift. Next, we measured the chemical shift of the ^{129}Xe due to the highest concentration protein solution. After the measurement, a small part (typically 100-1000 μL) was removed for concentration analysis after the experiment. Then, we diluted the solution with a premixture of phosphate buffer and 20% D_2O to produce the

next sample concentration. After measuring the chemical shift due to this new sample, we repeated the procedure until the protein concentration reached the lowest interesting concentration, typically about 0.1 mM.

We found it necessary to carefully control the buffer/D_2O solution used in the experiment because small changes in the solution could result in different shifts. Approximately 100 mL of 25 mM phosphate buffer/ 20% D_2O solution was prepared in which we dissolved a particular variant of BPTI. This same solution was used throughout the experiment on a particular variant of BPTI, for the baseline measurement and for any subsequent dilutions of the variant of BPTI.

Protein concentrations were determined after the ^{129}Xe chemical shift measurement using the absorption properties of the protein at 280 nm. Some of the samples were diluted 10 fold to bring the absorption onto the dynamic range of the optical spectrometer. The absorption coefficients used for the various BPTI species are as follows: 5.405 mM^{-1} for wild type BPTI[85] and F45S, 4.054 mM^{-1} for the Y23A mutant and the Y35G mutant.

The data was analyzed in two steps. First, the raw data referenced to the spectrometer transmit frequency was fit to a line (see Figure 5.3). The y-intercept of these lines were taken to be the chemical shift at zero protein concentration. Second, this zero concentration shift was subtracted from the data, and the data were replotted. The zero concentration shifts were slightly different for the different BPTI variants, perhaps because of slight differences in the buffer solution composition used for each variant.

5.4 Results and Discussion

We observe a chemical shift in the ^{129}Xe NMR frequency in the presence of different types of BPTI. Typical line width of the individual chemical shift measurements were 0.1-0.2 ppm full width at half maximum, and typical signal to noise ratios were 80-150 (Figure 5.4). However, the reproducibility of the chemical shift measurements limited the error to only 20 ppb, which we estimated by taking multiple measurements of the buffer solution without protein at various times during the experiment. This was likely limited by temperature fluctuations in the sample. We observed a temperature dependence of the ^{129}Xe chemical shift in the buffer solution corresponding to $\approx$0.13 ppm/°C. The temperature controller maintained the temperature to only 0.1 °C, which would give rise to fluctuations in the chemical shift of order tens of ppb. The origin of this temperature dependence was likely in part due to the clathrate formation around dissolved Xe and the interaction of ^{129}Xe with these clathrate structures, previously characterized by Seydoux [86, 70].

However, within this limitation, we were able to distinguish two distinct chemical shift behaviors in the four BPTI types (Figure 5.5). The data indicate a small concentration

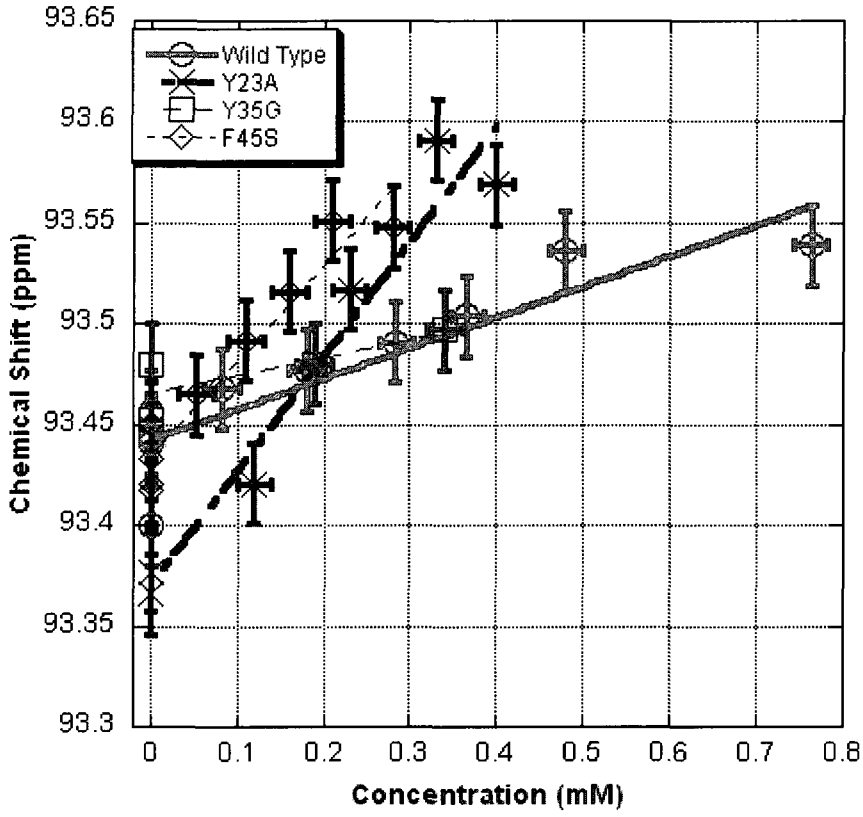

Figure 5.3. To properly determine the shift ^{129}Xe in buffer solution, we first plotted the data referenced to the external spectrometer reference frequency. The data was fit to lines, and the y-intercepts of the lines were taken to be the chemical shift at zero protein concentration. There was some variation between the different proteins, which was perhaps due to slight differences in buffer solution composition. The y-intercepts of the various BPTI types are as follows: Wild Type $\rightarrow$ 93.44 ppm; Y23A $\rightarrow$ 93.37 ppm; Y35G $\rightarrow$ 93.47 ppm; F45G $\rightarrow$ 93.43 ppm.

dependent shift in the presence of wild type BPTI and the mutant Y35G. The measured slopes of protein concentration dependence of the chemical shift α due to these two species are only 0.15 $\pm$ 0.02 ppm/mM and 0.10 $\pm$ 0.07 ppm/mM, respectively. In the case of the wild type, this small dependence is likely due to no specific binding to protein. This is consistent with previous work indicating the lack of hydrophobic binding sites in the wild type structure.

In the case of the Y35G mutant, this small dependence is consistent with a low fraction of mutant existing in a conformation that allows Xe to access its hydrophobic cavity. As previously stated, previous work demonstrated Y35G undergoes rapid motion while in solution phase. It is possible that this rapid motion sterically hinders Xe from binding to

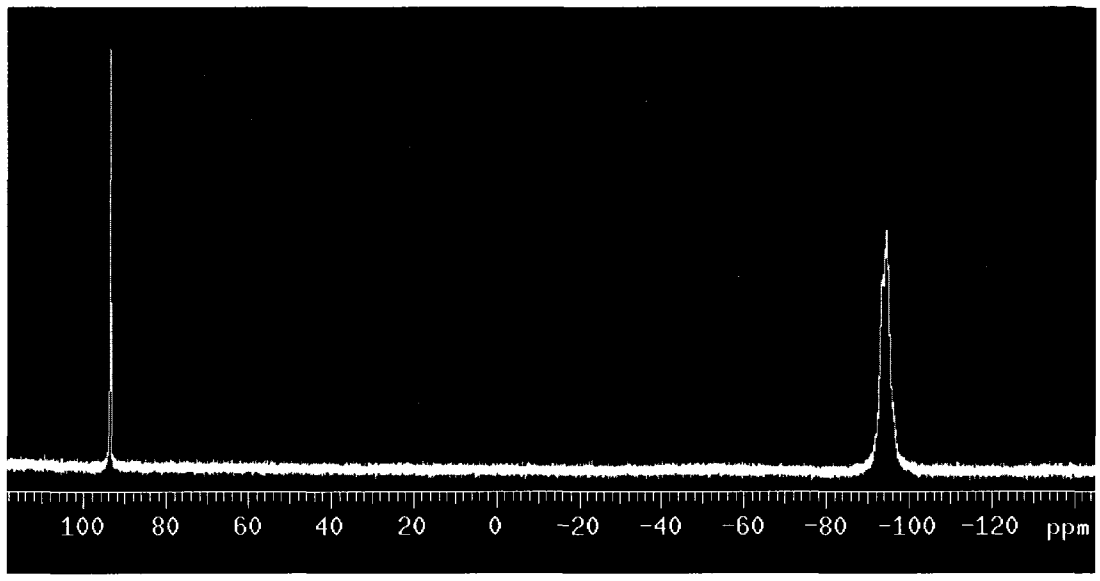

Figure 5.4. The typical ^{129}Xe spectrum in solution had a line width of between 0.1 and 0.2 ppm and a signal to noise ratio of 80-150 after 100 averages. Here, the dissolved peak is up field of the broader gas peak. The gas peak was due to the undissolved ^{129}Xe flowing through the microporous membrane tubes in the sample space. This peak is much broader because the magnet is shimmed on the D_2O line in solution, thus the field is optimized for detection of resonance in the region of the sample occupied by the solution. In this spectrum, 0 ppm corresponds to the spectrometer transmitter frequency.

a site, thus we only observe nonspecific binding of Xe to Y35G.

The data indicate a stronger concentration dependent shift for the Y23A and F45S mutants. The measured αs of these two species are 0.56 $\pm$ 0.05 ppm/mM and 0.47 $\pm$ 0.07 ppm/mM, respectively. The stronger shift supports the notion that Xe binds to the previously observed hydrophobic pockets.

Within error, we could not distinguish different behaviors in the concentration dependent chemical shift behavior of the wild type and the Y35G mutant or the Y23A and F45S mutants.

The chemical shifts do not show significant deviation from a linear relationship. Thus, we can use Eq. (5.19) to bound the δs and $\mathcal{K}_a$ associated with Xe binding to the protein and mutants. Recall that in order to be in the linear dependence regime, $\mathcal{K}_a[\text{Protein}] << 1$. By numerical analysis, we determined that chemical shift dependence curve does not significantly deviate from linearity if $\mathcal{K}_a[\text{Protein}]_{\text{max}} < \frac{1}{2}$, where $[\text{Protein}]_{\text{max}}$ is the maximum protein concentration used for a given mutant. Table 5.1 lists for each mutant the upper and lower bounds of $\mathcal{K}_a$ and δ, respectively.

The measured αs are much smaller than have been previously reported at higher

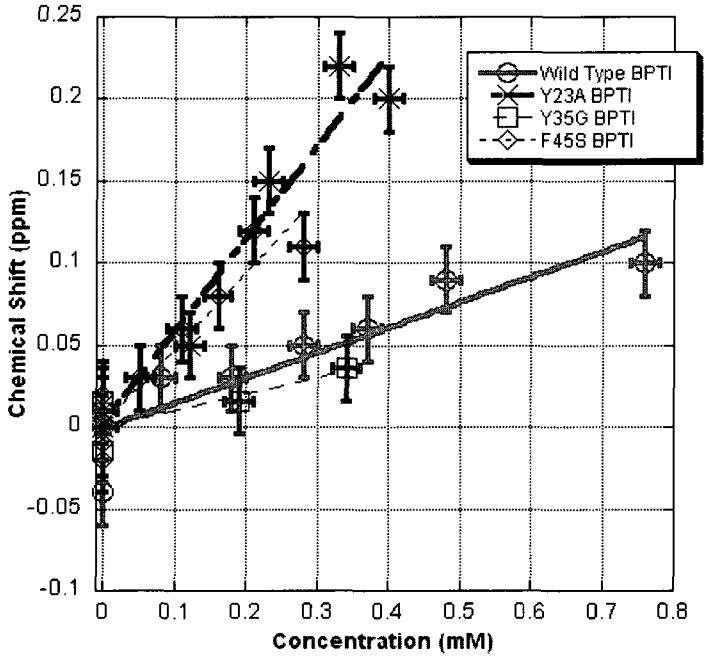

Figure 5.5. The final concentration dependent chemical shift data is referenced to the chemical shift at zero protein concentration. The figure clearly shows two distinct chemical shift behaviors. Wild type BPTI and the Y35G mutant exhibit the first, small shift behavior. The Y23A and F45S mutants display the second, larger shift behavior. However, due to the resolution of the chemical shift and the low protein concentrations, we cannot distinguish different behavior between the wild type and the Y35G or the Y23A and F45S.

Xe concentrations with myoglobin [82], maltose binding protein [24], and chemotaxis Y protein [25]. Maltose binding protein and chemotaxis Y protein had αs measured between 0.4 -2.7 ppm/mM shifts, and the linear portion of myoglobin's αs was between 2-3 ppm/mM. Typical Xe concentrations for these previous experiments were between 1 and 10 mM.

Rubin et al. [24] reported higher values of δ and lower values of $\mathcal{K}_a$ for maltose binding protein. Maltose binding protein has two specific binding sites. Rubin et al. estimated that the $\mathcal{K}_a$ for the two sites are 0.09 ± 0.04 mM^{-1} and 0.05 ± 0.01 mM^{-1}, and the associated δs were 3 ± 4 ppm and 30 ± 10 ppm, respectively. Based on this previous work, our bounds appear reasonable, but data at higher protein concentrations will result in tighter bounds that approach the actual values.

5.5 Conclusion and Future Research

We clearly observed a protein concentration dependence of the ^{129}Xe chemical shift in very low concentrations of Xe. This was possible only because of the enhanced sensitivity due to the high ^{129}Xe polarization obtained by our flow-through Xe polarizer. To the best of the author's knowledge, this is the lowest concentration of Xe ever used in this type of experiment. Low concentrations of Xe allow us to better fulfill the limits used to derive Eq. (5.19) or its linear limit. Recent numerical work using $\mathcal{K}_a$ and δ values of order measured by Ref. [24] indicate that Xe concentrations as low as 1 mM will begin to show deviations from the linear limit of Eq. (5.19), and that concentrations of 10 mM of Xe show significant deviations.

The data reveals two different behaviors in wild type mutant BPTI. Wild type and the Y35G mutant appear to only weakly interact with xenon and produce very small shift dependences in ^{129}Xe. The Y23A and F45S mutants appear to interact with Xe more strongly and give rise to larger shift dependences.

In order distinguish between the wild type and the Y35G mutant or the Y23A and the F45S mutants, one needs to either measure the ^{129}Xe chemical shift at higher concentrations of protein or reduce the error of the chemical shift measurements. By increasing the concentration of the protein, the chemical shifts should further separate and make it possible to determine the concentration dependence with greater precision. However, this requires the production of larger amounts of mutant proteins, a process that can be difficult and laborious.

Improving the resolution of the individual chemical shift measurements would increase the precision of the measurement without the need of producing large quantities of protein. However, this would require increased control temperature control of the sample.

One could possibly increase resolution of the chemical shift measurements by intro-

Table 5.1. The calculated upper and lower bounds of $\mathcal{K}_a$ and δ, respectively, the slopes (α) of the various proteins, and the maximum protein concentration used for each type of BPTI ($[\text{Protein}]_{\text{max}}$). The upper bound of $\mathcal{K}_a$ is calculated by multiplying $[\text{Protein}]_{\text{max}}$ by half. The lower bound of δ is then calculated using the slope of the chemical shift dependence and the approximation that the slope is $\alpha = \mathcal{K}_a\delta$. We believe that the trends in these bounds do not reflect the actual trends of the proteins. Rather, we believe it is more likely that all the proteins possess very similar δs of several ppm and that αs reflect the different $\mathcal{K}_a$s of the proteins.

	$[\text{Protein}]_{\text{max}}$ (mM)	α (ppm/mM)	$\mathcal{K}_a$ (mM^{-1})	δ (ppm)
Wild Type	0.8	0.15 ± 0.02	<0.66	>0.23
Y23A	0.4	0.56 ± 0.05	<1.25	>0.45
Y35G	0.34	0.10 ± 0.07	<1.47	>0.7
F45S	0.28	0.47 ± 0.07	<1.79	>0.26

ducing some reference internal to the sample that has similar temperature dependent chemical shift properties to ^{129}Xe. Perhaps, one could construct a sample with two regions. In one region, ^{129}Xe is allowed to interact with the protein; in the other region, ^{129}Xe interacts only with the buffer. This could be accomplished by separating the regions by a semipermeable membrane, such as those used to dialyze proteins. The buffer and Xe could freely pass through this membrane, but the protein could not pass through this membrane. One could simultaneously detected the resonance from ^{129}Xe in these two regions and use the signal from the ^{129}Xe in contact with only the buffer as an internal reference. Presumably, ^{129}Xe in buffer solution should have similar temperature dependent shift properties to ^{129}Xe in contact with proteins.

CHAPTER 6

CONCLUSION

In this dissertation, I have presented a characterization of a new style flow-through polarizer. We characterized the polarizer by measuring the final ^{129}Xe polarization and the in situ Rb polarization as a function of oven temperature, Xe concentration, total pressure, and total gas flow rate. By adjusting the temperature, we controlled the Rb number density and, thus, the laser absorption and Xe-Rb spin-exchange rate. Varying the Xe concentration controlled the Rb spin-destruction rate due to Xe, as did changing the total pressure. Changing the total pressure also affected the Rb line width and the molecular portion of the Xe-Rb spin-exchange rate. Adjusting the total flow rate affected the contact time between the ^{129}Xe and highly polarized Rb. We made accurate, qualitative predictions of the polarizer's behavior based on these principles.

However, when we compare the measurements to a numerical model of the system, we found discrepancies that reveal inadequacies in our understanding of the specifics of the physical mechanisms at work. These comparisons suggest that we do not entirely understand the Rb number density as a function of temperature and the Rb spin-destruction rate due to Xe. There also appear to be significant fluid dynamical affects for which our numerical model does not account.

To study the inadequacies in our model and to further optimize the polarizer, a number of further measurements should be made. A direct measurement of the Rb number density would confirm one of the above suspicions and help to improve the current model of the system. A two-dimensional mapping of the Rb polarization would aid in our understanding of the use of the available light and enable us to design more efficient optical pumping cells. Finally, an in situ measurement of the ^{129}Xe polarization would increase our understanding of the spin-exchange physics inside the optical pumping cell.

It will also become necessary to update the numerical model to handle this new information. A two-dimensional model would aid in interpreting the data from the proposed two-dimensional Rb polarization mapping, and a global fitting routine for the model would enable us to more precisely fit the model to the data.

I have also demonstrated the utility of this polarizer by conducting a brief study of Xe's interaction with BPTI. We have shown that a very low pressure of hyperpolarized

^{129}Xe can be used to study the interactions Xe with proteins, and we have discovered some interesting interactions between Xe and BPTI mutants. In particular, there is evidence that there exist hydrophobic cavities in the mutants Y23A and F45S to which Xe can bind. The data also support the theory that the majority of the solution phase mutant Y35G does not strongly bind to Xe. This, with previous data, suggests that a large fraction of Y35G is in a conformation in which the known cavity is inaccessible to the Xe.

Follow up measurements to this experiment should include a measurement of the characteristic interaction between Xe and Y35G bound to trypsin. Y35G bound to trypsin is known to be in a rigid conformation similar Y23A and F45S, thus the binding cavity should be available to Xe. Observation of a strong chemical shift dependence on the concentration of bound Y35G would be compelling evidence that steric effects are blocking Xe binding in unbound Y35G.

APPENDIX A

CENTRIFUGAL SEPARATION OF XE

A.1 Introduction

Hyperpolarized ^{129}Xe is now used for research in a variety of disciplines such as medical imagining, biological assays, and pores characterization [87, 26, 88]. It has recently been shown that large quantities of hyperpolarized ^{129}Xe can easily be produced using flow through methods. One manufacturer claims the ability to polarize 10 liters of Xe an hour [89]. Such hyperpolarization techniques require diluting Xe to a small percent of gas mixture, usually of order 1%.

Presently, the only method for separating the hyperpolarized Xe from the other buffer gases is to use cryogenic freezing. This method capitalizes on Xe's high melting temperature, 161 K at STP, compared to the other gases in the mixture. Xenon will freeze out of the gas stream and become deposited in some holding cell. The cryogenic cell is also used to store the Xe, as the relaxation time of Xe at 77 K and 2 kG is of order 2 hours [17]. The gas can be accumulated and stored for about this time before subliminating the solid and flowing the gas to an experiment.

Cryogenic separation is disadvantageous because it is a stepped method. One must accumulate Xe for some amount of time from a flow through polarizer and then divert or stop the flow when ready to subliminate the solid. It would be advantageous for a number of experiments to have the ability to separate the Xe continuously so that a steady stream of pure hyperpolarized Xe may be directed to an experiment.

Gas centrifuge separation may provide this ability. This is a process where separation is brought about by rotating the gases at high speed. Gases with higher molecular weights are pushed to the walls of the centrifuge, while lighter gases remain in the center. This is usually done in a continuous flow mode. One typically flows the gas mixture through several centrifuge stages in order to achieve desired separation. Gas centrifuges have been used to separate ^{235}U from ^{238}U for use in nuclear fission [90]. Such separations are time intensive because of the small mass separation between the two isotopes of Uranium. Gases with greater mass ratios should separate more easily using a gas centrifuge.

A.2 Simple Centrifuge Analysis

Centrifuge devices are most effective when using an axial countercurrent flow. One gains both enhanced separation and shorter equilibrium times [91].

We present a simple centrifuge model with no countercurrent flow for use in separating hyperpolarized Xe from buffer gases. Systems using axial countercurrent flow would perform better than what is presented here.

The radial partial pressures of gases in a centrifuge are given by [92]

$$p_i = p_{0i} e^{A_i r^2} \tag{A.1}$$

where, p_i is the i^{th} gas in the mixture, p_{0i} is the pressure in the center of the centrifuge, r is the radial distance from the center, and $A_i = \frac{M_i \omega}{2RT}$. It can be shown that the relationship between the center pressure and the partial pressure of the gas when not rotating is [92]

$$p_{0i} = \frac{A_i R^2}{e^{A_i R^2} - 1} p_{fi} \tag{A.2}$$

where R is the radius the centrifuge chamber.

Using these equations, we can determine the final gas fraction profiles for a given set of initial gas partial pressures. We apply this to a typical mixture of Xe in a flow-through polarizer (1% Xe, 10% N_2, 89% He). The simulated centrifuge was spinning at 50000 RPM and had a radius of 10 cm. We simulated removing the gas between 9cm and 10cm radius and injecting the mixture into another centrifuge stage with the same parameters. After a single stage, the Xe concentration is increased from 1% to about 3%. After three stages, the concentration increased to 27%, and after eight stages, the concentration has increased to 98%. Figure A.1 shows the some of the resulting pressure profiles in stages of the centrifugation process.

It is important to understand how long the gas mixture will spend in each stage of the centrifuge so that one can plan the volume of the stages and estimate losses in Xe polarization due to relaxation. The gas mixture will quickly gain angular momentum and establish a pressure gradient. Diffusion will then establish the equilibrium concentration profile.

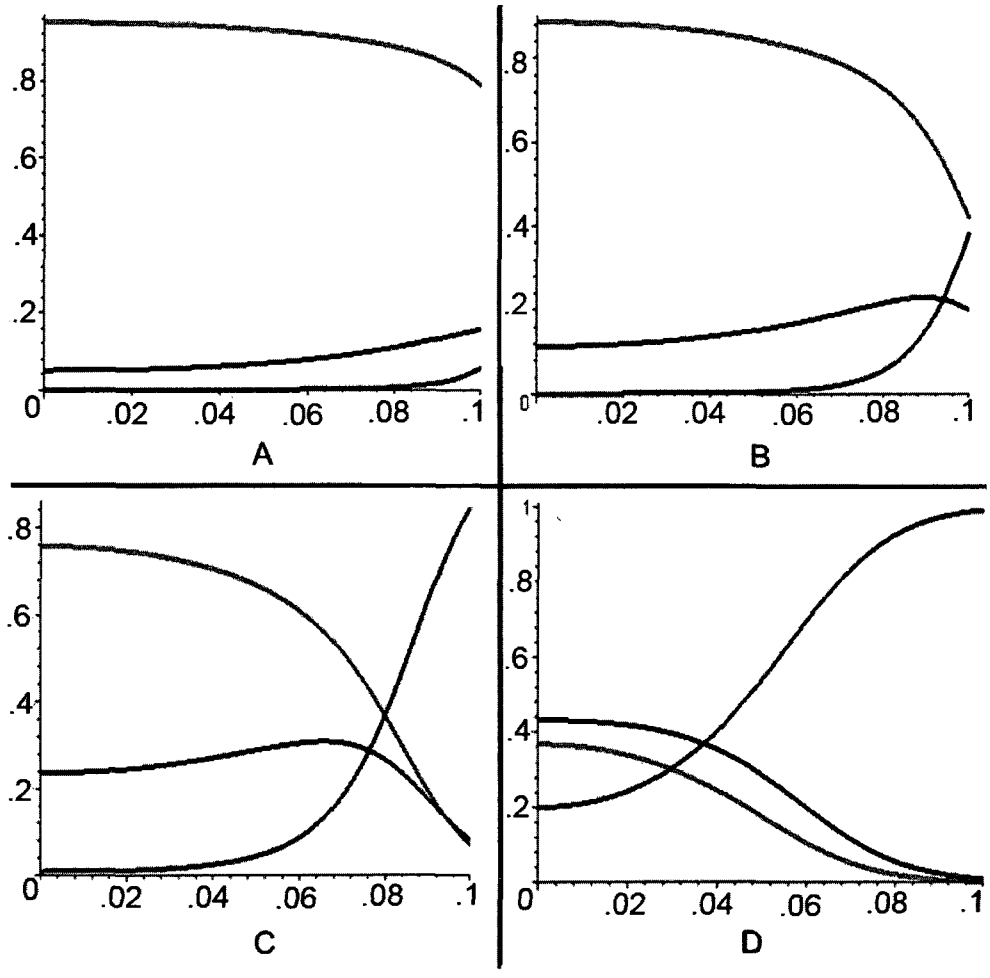

Figure A.1. The normalized gas pressure for 1 stage (A), 3 stages (B), 5 stages(C), and 8 stages (D) of centrifugation. The intial gas mixture is composed of 1% Xe, 10% N_2, and 89% He.

The diffusion equation for the heavy gas in two-component system in a cylindrical centrifuge is given by [93]

$$\frac{\partial}{\partial t}\left(\frac{Px}{RT}\right)+\frac{1}{r}\frac{\partial}{\partial r}\left\{\frac{P}{RT}D\left[\left(A_{heavy}-A_{light}\right)r^2x\left(1-x\right)-r\frac{\partial x}{\partial r}\right]\right\}=0 \qquad \text{(A.3)}$$

This is a nontrivial partial differential equation to solve, and one must resort to difficult numerical methods to approximate the solution. It is simpler to have the initial conditions be the known equilibrium profile of the rotating system and then use the nonrotating diffusion equation to determine the time it takes for the system to relax. It is reasonable to assume that these two processes take place on similar time scales.

The diffusion equation for a nonrotating system is simply

$$\frac{\partial x}{\partial t} - D\left(\frac{\partial^2 x}{\partial r^2} + \frac{1}{r}\frac{\partial x}{\partial r}\right) = 0 \tag{A.4}$$

Using Comsol FEMLAB 3.1 diffusion package, we started with the pressure profile given in equation A.1 and allowed the system to relax to equilibrium. Xe was taken to have a uniform concentration of 1% at equilibrium. Figure A.2 shows the time evolution of the concentration at the point r = 9.9 cm. It seems that the system relaxes on order of 60 seconds. This is comparable with numerical simulation done on other gases in centrifuge systems.

A.3 Conclusion

Centrifuge gas separation of hyperpolarized ^{129}Xe from flow-through systems is a feasible alternative to cryogenic separation. The above analysis indicates that one could reasonably enrich an initial 1% Xe mixture to > 90% purity in about 8 minutes. In order to realize a separator, one needs to find a material that is sufficiently strong to take the stress of high speed rotation and has long enough wall relaxation rates such that the polarized ^{129} Xe does not appreciably decay.

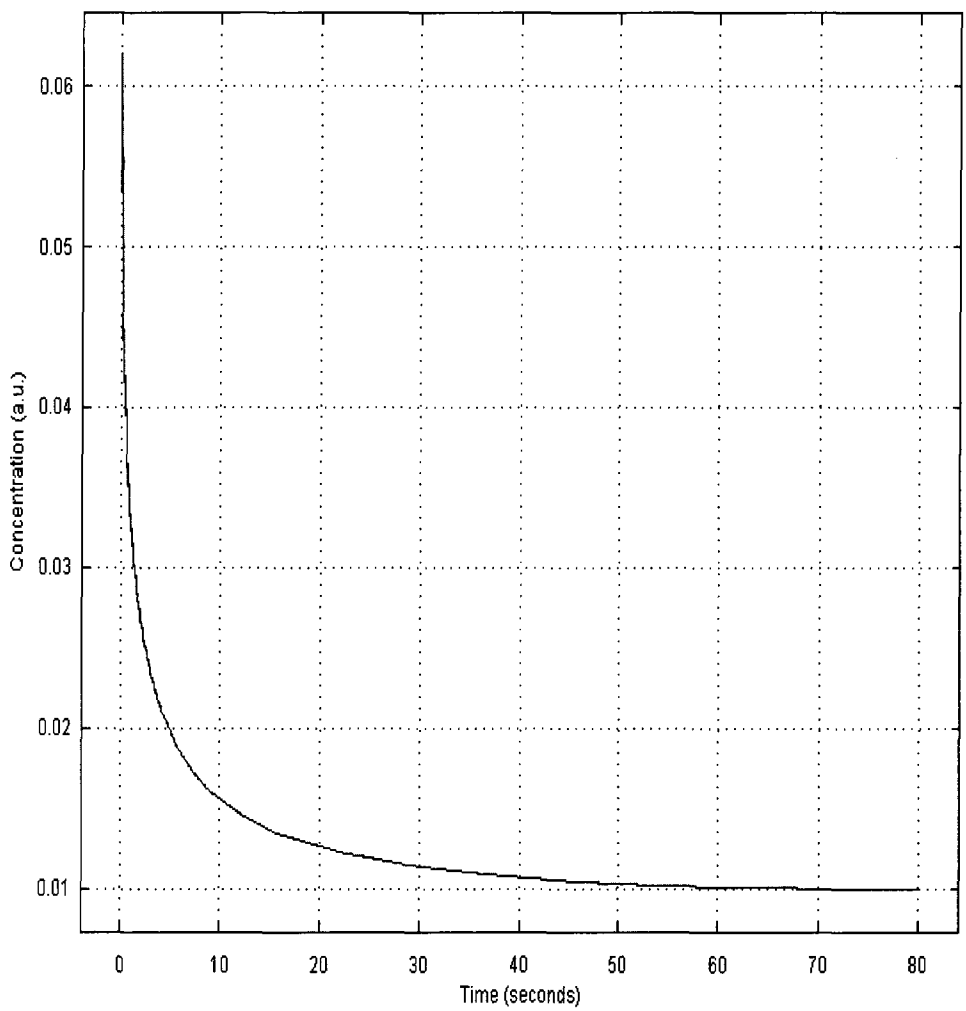

Figure A.2. The time evolution of the concentration of Xe gas in a 10 cm radius cylinder at r = 9.9 cm. The concentration profile is initially that of Xe in a centrifuge spinning at 50000 rpm.

APPENDIX B

MAPLE CODE FOR NUMERICAL MODEL

The following is the code used to calculate the theoretical numbers presented in Chapter 4. The code was implemented in Maple 6, a product of Waterloo Maple Inc.

Comments to the code are presented as either single line comments or multiline comments. Single line comments in Maple are implemented by placing a "#" before the text. Multiline comments are implemented by the following sequence: &\\\{*Comment Text*}.

The code is presented in a different font to set it apart from the rest of the text. Lines of code are marked by the ">>" symbol. Spaces have been placed in between comment blocks and major sections of code for readability.

```
>>restart;

>>with(plots):

>>Warning, the name changecoords has been redefined

>>#All values entered in cgs unless otherwise stated.
>>&\\{This is the section where we enter flow rates in sccm. We calculate the gas densities in amagat using the equation [G] = Gflow*P/Nu where Gflow is the gas flow rate, P is the total pressure, and N is the total flow rate. We also calculate the volumetric fractions. g is the total density of the gas in amagat.}
>>&\\{We define the temperature distribution T as a piecewise function that is temperature T0 for values in the oven of length L and exponentially decay to temperature T1 after leaving the oven.}

>>Xeflow:=10; #Xe gas flow rate in sccm
>>N2flow:=500; #N2 gas flow rate in sccm
>>Heflow:=1000; #He gas flow rate in sccm
>>p:=.83; #Total Pressure in cell in atm
```

>>T0:=140;# Temperature of oven in C

>>Nu:=evalf(Xeflow+N2flow+Heflow); #Total flow rate

>>Xe:=Xeflow*p/(Nu); #Xe density in amagat

>>N2:=N2flow*p/(Nu); #N2 density in amagat

>>He:=Heflow*p/(Nu); #He density in amagat

>>g:=evalf(Xe+N2+He); #Total gas density

>>fXe:=Xe/g; #Fractional density of Xe

>>fN2:=N2/g; #Fractional density of N2

>>fHe:=He/g; #Fractional density of He

>>T1:=24;#Temperature at front of oven in C

>>L:=50;# Length of cool portion of cell in cm

>>Lc:=.5;&\\{ Length over which temperature changes from oven to room in cm}

>>#T:=z->piecewise(z>L,T0,T1*exp(ln(T0/T1)/L*z)):

>>T:=z->piecewise(z>L,T0,T1+(T0-T1)*exp((z-L)/Lc));

>>l:=100: #Length of cell in cm

>>#h is Plancks constant=6.6260776e-34 J*s

>>&\\{G is the Rb D1 absorption line width = 18*He+17.8*N2+18.9*Xe GHz (Romalis et al., Phys Rev A,5(6): 4569-4578, 1997.)P is the power of the laser in Watts. nu0 is the center of the laser spectrum = (3e8)/795 GHz.}

>>&\\{FWHM is the full width at half max of laser spectrum, centered about the absorption line of Rb = 270GHz. sigma0 is the cross section of Rb on resonance=10^(-13) cm^2 (See Wagshul et al.)(Ruset uses 3.51e-13 in his model). sigmaRb is the rate constant for spin destruction due to Rb-Rb interactions (Barange et al., Phys Rev Lett, 80(13), 2801-2804, (1998)= 3.9e-14cm^3/s}

>>&\\{sigmaN2 is the rate constant for spin destruction due to Rb-N2 interaction (Walter et al., Phys Rev Lett, 88:093004, 2002)= 170*(1+(T-90)/194.3)/amagat*s where T is the temperature in C.}

>>&\\{sigmaHe is the rate constant for spin destruction due to Rb-He interactions (Walter et al., Phys Rev Lett, 88:093004,2002) = 24.6*(1+(T-90)/96.4/amagats. sigmaXe is the rate constant for spin destruction due to Rb-Xe binary collisions (Nelson and Walker, Phys Rev A, 65, 012712, 2001)=2.44/(amagat*s).}

>>&\\{GvdW is the spin destruction rate due to Rb-Xe van der Waals molecules (I.C. Ruset's Hyperpolarized 129Xe Production and Applications, PhD Thesis, Univ. New Hampshire, 2005.)=

6490/(fXe +1.1fN2+3.2fHe) /s where fXe, fN2, and fHe are the volumetric fractions of Xenon, Nitrogen, and Helium, respectively. The prefactors are to take into account fraction

of molecules with life time such that they produce S-damping. Values taken from Nelson et al., Phys Rev A,65:012712, 2002.}

>>&\\{alpha is the rate constant for spin destruction due to diffusion to the walls and quadrupole relaxation in Rb2 singlet molecules (Nelson et al., Phys. Rev. A, 65, 012712, (2001)) = 2.66 amagat/s, and the contribution to the spin destruction rate is Gdm = alpha/g. Here we calculate destruction rates based on densities and rate constants. Note that we need to convert density from amagat to particles/cm^3 for the GN2 and GXe. See above for documentation. Following Ruset's model, ignore prefactors for GvdW.}

```
>>h:=6.260766e-34:
>>G:=18e9*He+17.8e9*N2+Xe*18.9e9;
>>Centerwavelength:=794.7;
>>nu0:=3e17/Centerwavelength;
>>Width:=.3:
>>FWHM:=-3e17/(Centerwavelength+Width/2)+3e17/(Centerwavelength-Width/2);
>>P:=30; #Laser Power in Watts
>>R:=2; # radius in cm
>>A:=evalf(Pi*R^2);# Area in cm^2
>>sigma0:=4.83*10^(-13):# Cross Section in cm^2
>>#sigma0:=3.51e-13; #Bill's Sigma
>>#alpha:=2.66:
>>#G1:=1.95:
>>sigmaRb:=3.9e-14:
>>sigmaN2:=z->170*(1+(T(z)-90)/194.3):
>>sigmaHe:=z->24.6*(1+(T(z)-90)/96.4):
>>sigmaXe:=2.44e5:
>>#GvdW:=(.0234*K85+.00972*K87+.0432*J85+.0162*J87)*
6490/(fXe+1.1*fN2+3.2*fHe):
>>#K85:=(1+phi/(2*3/2+1)^2)^(-1):
>>#K87:=(1+phi/(2*5/2+1)^2)^(-1):
>>#phi:=G0/G:
>>#G0:=G1/22.5:
>>#J85:=1/(1+G1/g):
>>#J87:=1/(1+G1/g):
>>GvdW:=6469/(fXe+1.1*fN2+3.2*fHe):
>>GRb:=z->Rb(z)*sigmaRb:
>>GN2:=z->N2*sigmaN2(z):
```

```
>>GXe:=Xe*sigmaXe:
>>GHe:=z->He*sigmaHe(z):
>>#Gdm:=alpha/g:

>>&\\{C is constant necessary to have the integrated power specified, assuming normal
distribution. S is the standard deviation calculated from FWHM.}
>>S:=evalf(FWHM/(sqrt(8*ln(2))));
>>C:=
solve(int(C/(sqrt(2*Pi)*S)*exp(-(nu-nu0)^2/(2*S^2))*h*nu*A,nu=0..infinity)=P,C);

>>&\\{psii is the initial spectral profile. Assume normal distribution. Rb is the rubidium
number density distribution. This is a guess based on vapor pressures at 150 C and room
temperature. We set it up so the number density is constant in the back half of the cell
(corresponding to the time spent in the oven). We then allow the density to fall off to the
density at room temperature exponentially.}

>>psii:=evalf(C/(sqrt(2*Pi)*S)*exp(-(nu[m]-nu0)^2/(2*S^2))):
>>Rb:=z->10^(10.55-4132/(T(z)+273.15))/(1.38e-16*(T(z)+273.15)):
>>logplot(Rb(z),z=0..l);
>>plot(T(z),z=0..l);

>>&\\{sigma is the cross section for scattering of unpolarized light =G^2*sigma0/(4*(nu-
nu0)^2+G^2).}
>>&\\{Here, we also discretize psi and sigma so that the problem can be handled
numerically.}
>>&\\{Calculation of gopt, the scattering rate of photons per alkali-metal in unpolarized
vapor. gopt =int(psi*sigma[s], nu = 0 .. infinity). We are approximating using Simpson's
Rule and limits of integration nu0+/-4*FWHM.}
>>&\\{See Schaum's Outline Series "Mathematical Handbook of Formulas and Tables"
2nd Ed. p. 221 for Simpson's Rule.}
>>&\\{n is the number of points used in the integration and h is the calculated step
size.}

>>b:=nu0+4*FWHM;
>>a:=nu0-4*FWHM;
>>n:=500:
>>h1:=(b-a)/n:
>>nu[0]:=a:
```

```
>>for m from 0 to n do

>>    #nu[m]:=a+m*h1:
>>    nu[m]:=a+m*h1:
>>    psi[0,m]:=evalf(psii):
>>    sigma[m]:=(G)^2*sigma0/(4*(nu[m]-nu0)^2+(G)^2):

>>end do:

>>&\\{lambda0 is the inverse absorption length in unpolarized Rb. GSD is the total
spin destruction rate, the sum of all the individual rates.}
>>#lambda is the absorption length on the incident light

>>lambda0:=z->Rb(z)*sigma[k]:
>>GSD:=z->GRb(z)+GN2(z)+GHe(z)+GXe+GvdW:
>>lambda:=z->lambda0(z)*GSD(z)/(opt[i]+GSD(z)):

>>#Solving the diff eq diff(psi, z) = lambda*psi. Use Euler method.

>>f:=(z)->-lambda(z)*(psi[i,k]+F):
>>h2:=.1: #Step size in cm
>>itotal:=round(l/h2);

>>for i from 0 to (itotal) do

   >>opt[i]:=h1/3*(sigma[0]*psi[i,0]+2*sum(sigma[2*j-2]*psi[i,2*j-2], j=2..(n/2))+
4*sum(sigma[2*j-1]*psi[i,2*j-1], j=1..n/2)+sigma[n] *psi[i,n]):

>>    for k from 0 to n do
>>        F:=0:
>>        F1:=evalf(h2*f(i*h2)):
>>        psi[i+1,k]:=psi[i,k]+F1:
>>        if (psi[i+1,k]¡0) then
>>        psi[i+1,k]:=0:
>>        end if:

>>    end do;

>>end do;
>>s0:=seq([k+a,log10(psi[round(0/h2),k]+1)],k=0..n):
>>s1:=seq([k+a,log10(psi[round(20/h2),k]+1)],k=0..n):
```

```
>>s2:=seq([k+a,log10(psi[round(40/h2),k]+1)],k=0..n):
>>s3:=seq([k+a,log10(psi[round(60/h2),k]+1)],k=0..n):
>>s4:=seq([k+a,log10(psi[round(80/h2),k]+1)],k=0..n):
>>s5:=seq([k+a,log10(psi[round(100/h2),k]+1)],k=0..n):

>>p0:=pointplot({s0},color=red):
>>p1:=pointplot({s1},color=blue):
>>p2:=pointplot({s2},color=gold):
>>p3:=pointplot({s3},color=orange):
>>p4:=pointplot({s4},color=yellow):
>>p5:=pointplot({s5},color=green):

>>#display({p0,p1,p2,p3,p4,p5});
```

>>&\\{We now need to calculate the Rb polarization, given by PRb=opt/(opt+GSD), and the Xe polarization. The Xe polarization is given by:diff(PXe, t) = GSE*(PRb-PXe)-Gtot*PXe, where GSE is the total spin-exchange rate and Gtot is the total Xe spin destruction rate. Now, recall that the Xe is moving, so we need to rewrite this in terms of the spatial variation of the Xe and include a function of the Xe velocity. Using the chain rule, we get diff(PXe, z) = (GSE*(PRb-PXe)-Gtot*PXe)/v. We will solve this differential equation using Euler's method.}

>>&\\{The total spin destruction rate is just the molecular spin destruction rate plus the wall rate. The molecular spin destruction rate is taken from Chann et al. in PRL 2002, and the wall relaxation rate is a guess.}

>>&\\{All the spin-exchange equations are taken from Nelson's thesis (2001). The binary spin exchange rate cross section is given as sigmaSE = 2.2*10^(-17) at 20 C and Nelson says it has a temperature dependence of T^(1/2) , so I wrote down sigmaSE = 2.2*10^(-17)*(T+272.15)^(1/2)/(20+272.15)^(1/2). The van der Waals molecular rate cross-section is worked out by Nelson to be Kappa*alpha*G0*G1*(.358+.648*nu[85]/((1+G1/G)^2)+.625*nu[87]/(1+(2.25*G1/G)^2))/(2*Hbar*x*G1*G). I call Kappa*alpha*G0/(2*Hbar*X*G1) =B and Nelson found it has a value of 1.16e-15. He also claims that it has a temperature dependence of 1/T^(3/2) so I wrote down
B := 1.16*10^(-15)*(20+272.15)^(3/2)/(T+272.15)^(3/2). I know that Kappa is the Xe-Rb molecule chemical equilibrium coefficient, G0 and G1 are the characteristic gas density when the molecular life time transition from slow to fast and from fast to very fast, respectively. Hbar has the usual meaning of Plank's constant. alpha is the coupling constant between the Rb electron and Xe nuclear spins. x = gamma*N/alpha, where gamma is the coupling constant between the Rb electron spin the the molecular tumbling angular momentum, N.

nu[85] and nu[87] are the relative abundance of the two isotopes of Rb. The front coefficients I think are due to the different nuclear spin of the two isotopes. The 2.25 in front of the density term of the third term has something to do with the difference in hyperfine precession frequency between Rb85 and Rb87. Nelson works it out. G1, it turns out, has a very strong temperature dependence. Nelson recorded the value of G1 for 120 C, 130 C, 140 C, and 150 C. I plotted them and fit them to a power function. The result was that G1 = 1.92/((T+273)*(1/413))^6. This is a stronger temperature dependence than it seems Nelson actually reports, but I just took the data and plotted it. He reported something more like a 1/T^2 dependence, which he got because he referenced T=0 to the freezing point of water. I reference T=0 to 0 K.}

>>&\\{So, I actually solve for the polarization distribution of the Xe in rings around the cell. The gas velocity rate is a function of radial distance from the center of the cell. At the edge of the cell, the gas is assumed to not be moving at all. Fluid dynamics tells us that the velocity of a gas is given by v = vmax*(1-(r/R)^2), where r is the radial distance, R is the radius of the cell, and vmax = 2*Nu/(A*g) is the maximum velocity of the gas. It is related to Nu, the total flow rate, A the cross-sectional area of the cell, and g the total gas density.}

>>sigmaSE:=z->2.2e-17*(T(z)+272.15)^(1/2)*(20+272.15)^(-1/2);

>>#spin-exchange velocity-averaged cross section

>>GW:=1.3e-2:# Wall relaxation. A good guess. In /s

>>GXevdW:=6.72e-5*(1/(1+.25*He/Xe+1.05*N2/Xe)):#Xe-Xe Van der Waal relaxation from Chann et al. PRL 2002

>>Gtot:=GW+GXevdW;#Total Xe relaxation

>>gXe:=5230:# van der Waal spin-exchange due to [Xe] in /s

>>gN2:=5700:# van der Waal spin-exchange due to [N2] in /s

>>gHe:=17000:# van der Waal spin-exchnage due to [He] in /s

>>GSE:=z->Rb(z)*(sigmaSE(z)+B(z)*G1(z)/g*(.358+.648*atta85/(1+(G1(z)/g)^2)+.625*atta87/(1+(2.25*G1(z)/g)^2))); # Total spin exchange rate in /s

>>G1:=z->1.92*((T(z)+273)/413)^(-6);# characteristic density for change between very slow and slow molc regime

>>B:=z->1.16e-15*(T(z)+272.15)^(-3/2)*(20+272.15)^(3/2);# See above

>>atta87:=.2718;

>>atta85:=.7217;

>>PXe[itotal]:=0:#intialize Xe polarization

>>vmax:=evalf(2*Nu/(A*60*g));#max linear velocity of gas in cm/s

>>v:=j->vmax*(1-(r[j]/R)^2);#Poiseuille distribution of axial

```
>>veloicity as a function of radius in cm/s
>>rstep:=50;
>>rsize:=R/rstep;
>>r[0]:=0:

>>for j from 0 to rstep
>>    do

>>    r[j+1]:=r[j]+rsize:
>>    PXe[j,itotal]:=0:

>>end do:
>>for i from 0 to (itotal) do

>>    PRb[i]:=evalf(opt[i]/(opt[i]+GSD(i*h2))):

>>end do:
>>for j from 0 to (rstep-1) do

>>    q:=itotal:
>>    j;

>>    for i from 1 to (itotal) do

>>        F1:=evalf(h2/v(j)*(GSE(q*h2)*PRb[q]-PXe[j,q]*(GSE(q*h2)+Gtot))):
>>        PXe[j,q-1]:=evalf(PXe[j,q]+F1);
>>        if PXe[j,q-1]¡0 then PXe[j,q-1]:=0 end if:
>>        q:=q-1;

>>    end do;

>>end do;

>>unassign('j');

>>for i from 0 to itotal do

>>    pXe[i]:=sum(PXe[j,i],j=0..(rstep-1))/(rstep-1);

>>end do:

>>P1:=seq([i*h2,PRb[i]],i=0..round(itotal)):
>>P2:=seq([i*h2,pXe[i]],i=0..round(itotal)):
```

```
>>PP1:=pointplot({P1},color=black):
>>PP2:=pointplot({P2},color=blue):
>>Rbplot:=plot(Rb(z)/Rb(l),z=0..l):
>>display({PP1,PP2,Rbplot});
```

APPENDIX C

PROCEDURE FOR MAKING OPTICAL PUMPING CELLS

C.1 Introduction

During the course of the lifetime of the Xe polarizer, it will frequently need to have optical pumping cells, called GGPCs, either rebuilt or newly fabricated because of the tendency for the Rb to react with the coating and trace amounts of O_2 over time. In addition, the Rb will tend to coat the side wall of the cell near the cooling jacket, and this has been observed to have deleterious effects on the ability of the polarizer to produce highly polarized ^{129}Xe. In this appendix, I will describe how to both rebuild and fabricate new GGPCs. The only difference between the two procedures is that when rebuilding an old GGPC, the spent Rb must be safely removed and a new Rb Retort and Glass Wool Insertion Tube must be reattached by the resident glass blower. When fabricating a GGPC, these steps may be left out.

When fabricating a new cell, the glass blower has found the picture shown in Figure C.1 useful to properly form the expanded region near the top of the GGPC. He has also used the top of the oven as a guide to properly space the inlet tube and optical pumping regions (see Figure C.2), so the top of the oven should be lent to the glass blower when he is asked to fabricate a new cell. Full page plans for the GGPC are found in Figure C.2-C.4. A perspective model of the GGPC with the Rb Retort and the Glass Wool Insertion Tube is shown in Figure C.5, and a perspective model of the GGPC with the Rb Retort and the Glass Wool Insertion Tube pulled off is shown in Figure C.6.

If you are fabricating a new cell, make copies of Figures C.1-C.4, take them along with the top of the oven to the glass blower, and ask him to fabricate the cell. After receiving the newly fabricated cell, begin with the section C.4 and continue the procedure to the end. If you are rebuilding the cell, begin the procedure with section C.2. You will still need to make copies of Figures C.1-C.4 and take them to the glass blower when you take the old GGPC to him to have the Rb Retort and Glass Wool Insertion Tube reattached, but he will not need the top of the oven. At the time of this writing, there were four cells of this design designated GGPC1, GGPC2, GGPC3, and GPPC4. Slight differences in the cells exist such as the inlet and outlet valves used and the number of glass wool

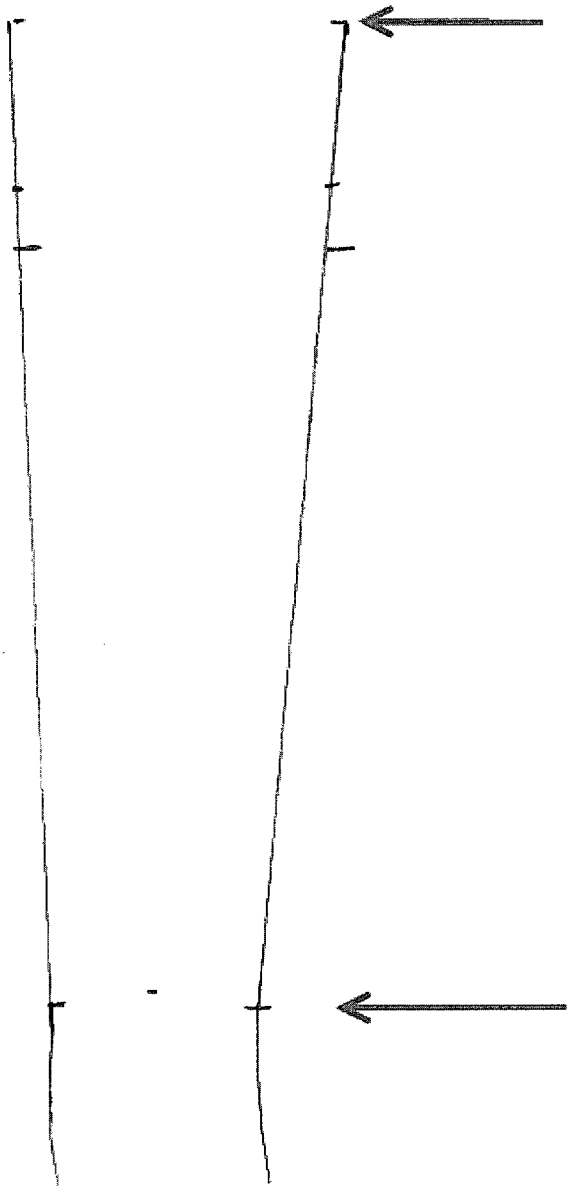

Figure C.1. A sketch of the expand region the glass blower uses to aid in GGPC fabrication. Due to publication requirement, the drawing is not to original scale. To scale correctly, the figure should be blown up so that the distance between the two arrows measures 22 cm.

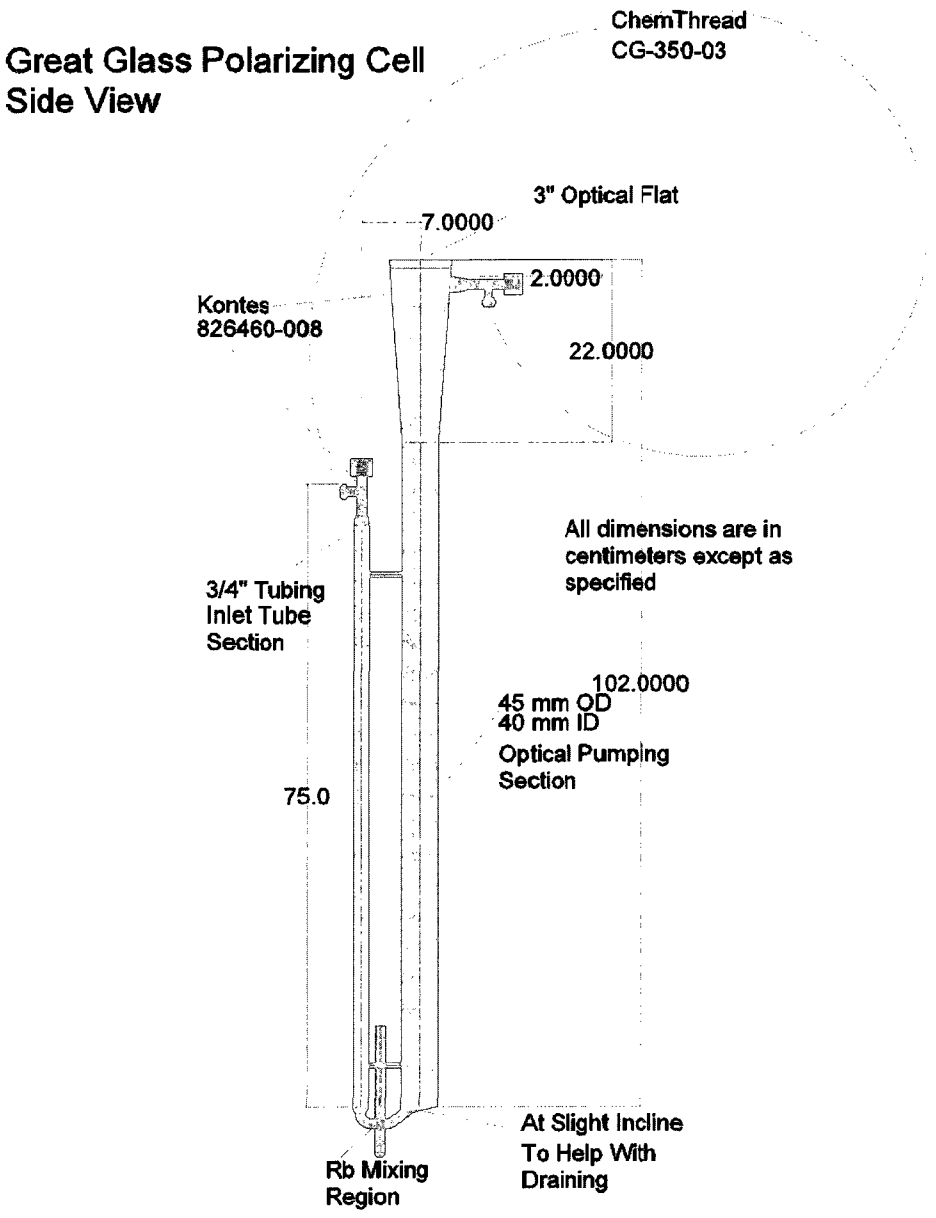

Figure C.2. The GGPC schematic side view.

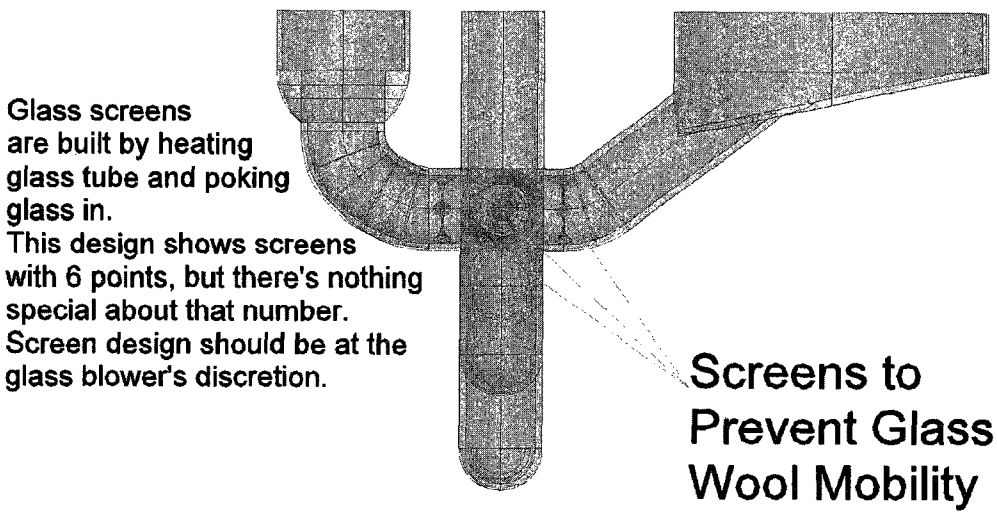

Figure C.3. An expanded view of the GGPC side view. This figure highlights the positions of the glass screens used to keep the glass wool in place. As indicated in the figure, the glass wool screens are built by heating the glass tube and poking the glass in. This design shows the screens with six points, but a fewer number or greater number can be made at the glass blower's discretion.

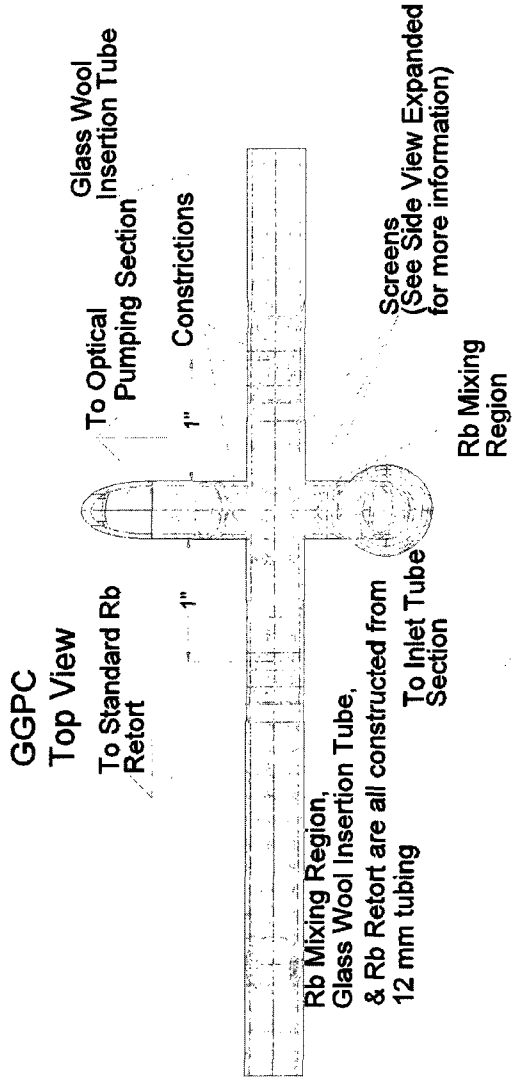

Figure C.4. A top view of the Rb mixing region. The location of the screens in the Rb mixing region and the Rb Retort are labeled. Please note that for GGPC 1, only the screen just before the Optical Pumping Section exists, and it is made out of a glass frit. For GGPC2-4, the Rb Retort and Glass Wool Insertion Tube are on the opposite side shown. In principle, the side on which the Rb Retort and Glass Wool Insertion Tube lay does not matter so long as the screen is on the Rb Retort side and not on the Glass Wool Insertion Tube side. However, this redesign should allow easier access to the Rb Retort while the cell is connected to the current configuration of the Saam Group vacuum system. For readers not in the Saam group, a decision should be made on the location of these tubes based on the equipment setup available. After the Rb Retort and Glass Wool Insertion Tube are pulled off, the GGPC is more or less symmetric in this respect.

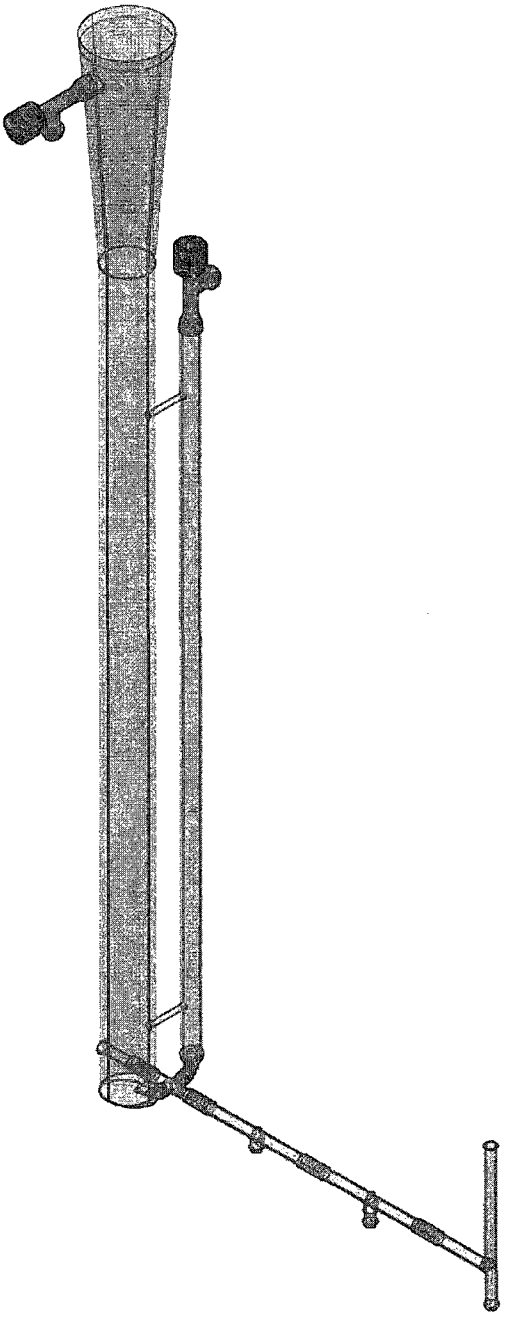

Figure C.5. A model of the GGPC with the Rb Retort and Glass Wool Insertion Tube attached. The cell should look something like this after being returned from the glass blower.

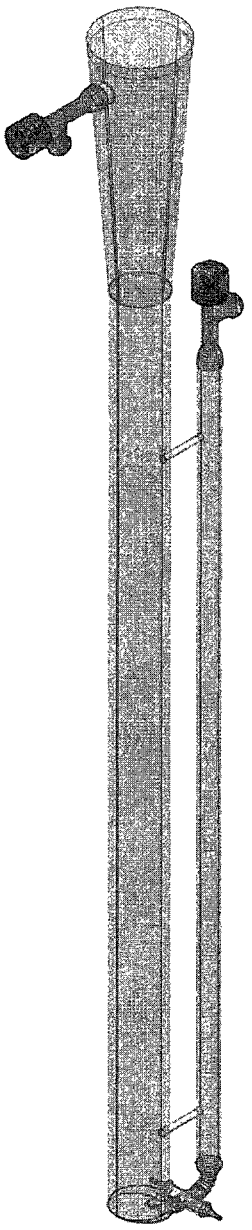

Figure C.6. A model of the cell with the Rb Retort and the Glass Wool Insertion Tube pulled off.

screens. Therefore, when rebuilding or ordering new parts for existing cells, the cell should be examined to determine its precise configuration. New cells may be made using the supplied plans.

C.2 Clean Out Old Rb

The reacted Rb must be cleaned out before the new Rb is introduced into the cell. The old Rb will be removed by reacting the Rb with water in a moist airstream. A length of $\frac{1}{2}$" tubing may be used to connect Inlet Valve (GGPCIV) via the ChemThread connection on that valve. Tubing will need to be rigid in order to provide a firm connection between the ChemThread and the tubing. Humid gas can be flowed into the cell to react with the Rb. Rubidium Hydroxide (RbOH) will form as a result of this reaction. RbOH is a caustic agent (base) and will need to be neutralized using standard techniques. Once neutralized, the product can be disposed of as a salt. After the Rb has been removed, the sealed Glass Wool Insertion Tube and Rb Retort will need to be cut to allow for a new Glass Wool Insertion Tube and Rb Retort to be attached. The old glass wool can be removed at this point.

C.3 Attach New Retort and Glass Wool

A new Rb Retort and Glass Wool Insertion Tube will need to be installed on the GGPC. Production and installation of the retort and inlet will need to be done by a qualified glass blower. Plans for the retort and inlet are provided in Figure C.2-C.4.

C.4 Clean New Glass Wool

New glass wool will need to be prepared to introduce into the rebuilt or new GGPC. The glass wool should be cleaned by soaking it in piranha solution (3:1 concentrated sulfuric acid: 30% hydrogen peroxide) for 4 hours. Afterward, the glass wool should be rinsed with deionized (DI) water to remove all traces of the piranha solution. **Acid resistant gloves and proper face protection should be worn while handling piranha solution, and all work should be done under a hood. Please refer to section C.6 for more information on using piranha solution. Piranha solution should handled only by knowledgeable individuals.**

C.5 Leak Test Cell

Upon return of the GGPC from the glass blower, the cell should immediately be helium (He) leak tested to assure that there are no glass blower errors in the work. The cell should leak tested by closing the inlet and outlet valves (GGPCIV and GGPCOV, respectively) and corking the Glass Wool Insertion Tube and the Rb Retort. Corks should

be either rubber or neoprene. A small amount of vacuum grease may be applied to the corks before insertion to provide a better seal. If vacuum grease is applied, it must be thoroughly cleaned after the leak checking.

In the Saam lab, there exists a custom glass tube for connecting GGPCOV to the vacuum system. This tube has a U-bend around which a Dewar may be placed to make a cold trap. This glass tube may be used both to evacuate the cell and to flow N_2 from the vacuum system into the cell.

C.6 Clean Cell Surface

After leak testing, the cell's interior surface will be cleaned. The Rb Retort and Glass Wool Insertion Tube need to be corked using neoprene corks. Rubber corks will dissolve in the cleaning agent and are unacceptable for this portion of the procedure. The interior surface should first be rinsed with DI water. All interior surfaces must be wetted. After rinsing, the interior surfaces should be cleaned using 100 mL piranha solution. Again, all interior surfaces must be wetted. After cleaning, the cell should be rinsed seven times with DI water. Thoroughly wash the entire interior surface to remove all traces of the piranha solution.

Care must be taken while handling the cell with piranha solution. It is advised that individuals cleaning the cell should wear appropriate acid resistant gloves, face shields, upper torso protection, and an acid resistant apron. In addition, individuals using piranha solution must wear full length pants and closed toe shoes. Cleaning of the cell should be done in a hood with the sash closed as far as possible while still allowing access to the cell.

The cell must never be completely sealed during washing with piranha solution. Piranha solution can evolve gas upon reaction with organic residue which may pressurize the cell and cause an explosion. Therefore, every effort must be taken to provide proper ventilation of the cell during cleaning. Fresh piranha solution is very warm, possibly higher than 100 °C. Therefore, glass surfaces in contact with piranha solution may become warm to the touch.

Handling piranha solution should be done with another knowledgeable individual. Under no circumstances should cleaning the cell be attempted alone.

Readers are encouraged to refamiliarize themselves with proper handling of piranha solution before attempting this procedure. Be aware that this section is not meant to replace other guidelines for proper handling of piranha solution and is by no means an exhaustive guide on safe use or handling of piranha solution.

C.7 Dry Cell Surface

After cleaning and rinsing, all trace of residual water must be removed from the interior surface of the cell. This can be done by attaching a length of tubing to GGPCIV and flowing dry N_2 through the cell. Both GGPCIV and GGPCOV will need to be opened, and the Rb Retort and the glass inlet section may be uncorked. Using a heat gun, gently drive the residual water starting near GGPCOV and moving downstream. The cell should be sealed under a nitrogen atmosphere after drying (close GGPCIV, GGPCOV, and recork openings).

C.8 Coat the Cell Surface

The interior surface of the cell must be coated with SurfaSil®. SurfaSil® has been shown to decrease the relaxation rate of Xe when interacting with the wall. Typical wall times for surfaces treated with SurfaSil® are measured in tens of hours. Thermo Scientific, the manufacture of SurfaSil®, provides a recommended coating procedure. That procedure is reproduced here for the reader's convenience.

Caution: SurfaSil® produces HCl as a byproduct of coating surfaces.

1. Dilute the SurfaSil® solution in a nonpolar organic solvent. Cyclohexane has been used previously, but other solvents include acetone, toluene, carbon tetrachloride, methylene chloride, chloroform, xylene, or hexane. Mixtures of 10% mass to volume ratio have been used previously.

2. Introduce SurfaSil® solution into the cell and assure that the solution wets all the interior surfaces of the Optical Pumping Portion of the GGPC. This can be done by manual agitation of the cell.

3. Rinse the cell with the same solvent in which the reagent was diluted.

4. Rinse the cell with methanol. This rinse is required to prevent interaction of the SurfaSil® Coating with water and thus, reversing siliconization.

5. Air-dry the cell for 24 hours or heat at 100 °C for 20-60 minutes. Whether air-dried or heated, a constant flow of N_2 must be provided through the cell to prevent contamination of cleaned surfaces. The manufacture cautions that a vented, explosion-proof oven should be used. The author has previously used heat tape to heat dry the cell and has never encountered a dangerous situation in which an explosion-proof oven was required, i.e., the cells have never exploded while drying.

C.9 Introduce Glass Wool

After coating the surface, the glass wool should be introduced to the cell and sealed. The glass wool should be inserted into the GGPC via the Glass Wool Insertion Tube. Use of a glass rod to stuff the glass wool past the constriction is advised. The glass wool should be put into the Insertion Tube in sections rather than all at once to prevent clogging the constriction. After a sufficient amount of glass wool has been placed in the optical pumping cell (enough to completely fill the connecting tube), the Glass Wool Insertion Tube should flame sealed by heating the constricted area of the glass and pulling off the inlet tube. The constricted glass should be flame annealed with a cool (yellow) flame until covered in soot.

This procedure may be done without N_2 flowing through the cell provided it is done quickly.

C.10 Introduction of Rb into Cell

After the glass wool has been flame sealed in the cell, the Rb may be introduced into the cell to via the retort. N_2 should be flowing through the cell, and the cell valves should be configured such that the entire N_2 flow is exiting through the retort. N_2 flow rate must be kept low enough so that it does not dislodge the glass wool (this should only be a problem for GGPC1 since it has only one glass wool screen).

Rb is generally provided in scored ampoules. Before introduction, the exterior of the Rb ampoule should be thoroughly cleaned to prevent contamination of the cell. Some solvent such as acetone is suggested for this cleaning. Gloves should be worn while handling the ampoule to prevent hand oils from depositing onto the exterior surface.

After cleaning, the ampoule should be held near the Rb Retort and broken along the score. The ampoule should immediately be dropped into the Rb Retort to prevent reaction with the atmosphere. The retort should them be flamed sealed by pulling off the top $\approx$2 in. of the retort. It is strongly suggested that a glass rod be attached to the retort exhaust tube before attempting to pull it off because the surface will become very hot. The N_2 flow needs to be stopped just before the retort exhaust closes otherwise the gas pressure will burst the hot glass. The retort may be flame annealed after it is sealed.

C.11 Cell Bake-Out

After Rb introduction, the cell should be evacuated and heated to $\approx$100 °C, but not greater than 100 °C. If the surface is heated to temperatures significantly greater than 100 °C, the SurfaSil® Coating may degrade. Heating is done using three lengths of heat tape to cover the three primary portions of the GGPC: inlet tube, Rb Mixing Region, and optical pumping region. The heat tape should not surround the tube in which the

Rb resides. These heat tape lengths should be controlled using three Variacs capable of 20A/150V output.

The heat tape can be applied in the following manner. First, the cell should be wrapped in a layer of aluminum foil. This layer will help evenly distribute the thermal energy from the heat tape. Second, the heat tape should be wrapped around the three areas of the cell. Care should be taken to evenly wrap the heat tape around the cell. Third, apply a second layer of aluminum foil on top of the heat tape. Finally, attach thermal sensors to the exterior layer of the aluminum foil. At least three thermal sensors should be used (one for each section). Thermal sensors can be attached by placing them under a square of aluminum foil.

The cell should be actively evacuated while heating. The cell may be evacuated by any clean (non-oil based) pump or a pump that is properly cyrotrapped to prevent contamination of the cell. The pump should be capable of pumping down to 10^{-8} torr. Even if the pump is clean a cyrotrap between the cell and the vacuum system is advised to trap volatiles evolving off the surface of the cell during the baking.

The GGPC should be baked for at least 3 full days. It is advisable to monitor the surface temperature of the cell and the pressure in the cell at least twice a day.

C.12 Chase Rb onto Glass Wool

After baking is complete and the cell is cool, the Rb may be chased on to the glass wool. This is done by applying heat to the Rb via a relatively cool flame and vaporizing it. First, the heat tape and aluminum foil layers should be removed. Then one can start distilling and chasing the Rb.

The Rb Retort has a tube in which the Rb was introduced and two nubs with constrictions separating these segments. The Rb should be distilled from the introduction tube into the first nub. While chasing the Rb, all the glass of the retort on which one does not wish the Rb to condense should be kept hot. One should attempt to leave a small amount of Rb left in the introduction tube, because it is assumed that impurities in the Rb will have a higher boiling point and will be the last to vaporize.

After chasing the Rb into the first nub, the introduction tube will be pulled off by heating the area around the first constriction and closing the glass. Since the glass is under vacuum, care should be taken to prevent the glass from bulging (pooching) in, as this results in a weaker seal. To do this, apply more heat to the side of the constriction that will be pulled off. This will result in that side of the constriction pooching, and the glass remaining in the seal will have a concave geometry. The remaining seal may be flame annealed.

After allowing the glass to cool, the Rb can be chased from the first nub into the second nub in a manner similar to that previously described. One should avoid applying heat to the seal as this may result in the glass cracking. Again, a small amount of Rb should be left in the first nub. When the nub is cool enough to handle, it may be pulled off in a manner similar to that described above. After allowing the glass to cool, the Rb can be chased from the second nub onto the glass wool. Care should be taken to confine the Rb to the glass wool. Again, a small amount of Rb should be left in the second nub, after which, the second nub may be pulled off. Extreme care should be taken when pulling off this segment as this will be the final seal in the cell. The cell should appear like the model in Figure C.6 after this final seal is made.

C.13 Recheck the GGPC for Leaks

After the Rb has been chased onto the glass wool, it is advisable to recheck the cell for leaks using a He leak tester. This will assure that the seals on both the Glass Wool Insertion Tube and the Rb Retort are good.

C.14 Back-fill GGPC with N_2

After leak checking the cell, the GGPC should be back-filled with $\approx$1 atm of N_2.

C.15 Conclusion

This procedure evolved over time as we tested different method of producing these cells. However, this method should not be considered the optimal method, and the reader is encouraged to deviate from the presented designs and procedures as is seen fit for producing better polarizing cells. I have tried to present the reasoning behind the procedure and the designs here and in the body of the thesis so that the reader can make informed decisions about aspects that they might change to produce better cells.

REFERENCES

[1] J.J. Sakurai. *Modern Quantum Mechanics.* Addison-Wesley Publishing Co., 1993.

[2] W. Happer. Optical pumping. *Rev. Mod. Phys.*, 44(2):169–249, 1972.

[3] W. Happer and W.A. VanWijngaarden. An optical pumping primer. *Hyperfine Interactions*, 38:435–470, 1987.

[4] D. J. Griffiths. *Introduction to Quantum Mechanics.* Prentice Hall, 1994.

[5] T.G. Walker and W. Happer. Spin-exchange optical pumping of noble-gas nuclei. *Rev. Mod. Phys.*, 69:629–642, 1997.

[6] A. Kastler. The optical production and the optical detection of an inequality of population of the levels of spatial quantification of atoms. application to the experiments of stern and gerlach and to magnetic resonance. *Journal de Physique et le Radium*, 11:255–265, 1950.

[7] J. Brossel, A. Kastler, and J. Winters. Optical method of creating an inequality of population between zeeman sub-levels of atomic ground states. *Journal de Physique et le Radium*, 13:668–669, 1952.

[8] M. A. Bouchiat, T. R. Carver, and C. M. Varnum. Nuclear polarization in ^{3}He gas induced by optical pumping and dipolar exchange. *Phys. Rev. Lett.*, 5(8):373–375, Oct 1960.

[9] E. Babcock, I. Nelson, S. Kadlecek, B. Driehuys, L. W. Anderson, F. W. Hersman, and T.G. Walker. Hybrid spin-exchange optical pumping of He. *Phys. Rev. Lett.*, 91(12):123003, 2003.

[10] I.A. Nelson. *Physics of Pracitcaly Spin-Exchange Optical Pumping.* PhD thesis, University of Wisconsin-Madison, 2001.

[11] I.C. Ruset. *Hyperpolarized ^{129}Xe Production and Applications.* PhD thesis, University of New Hampshire, 2005.

[12] D. Raftery, H. Long, T. Meersmann, P. J. Grandinetti, L. Reven, and A. Pines. High-field NMR of adsorbed xenon polarized by laser pumping. *Phys. Rev. Lett.*, 66(5):584–587, 1991.

[13] M.S. Rosen, T.E. Chupp, K.P Coulter, R.C. Welsh, and S. D. Swanson. Polarized ^{129}Xe optical pumping/spin-exchange and delivery system for magnetic resonance spectroscopy and imaging studies. *Rev. Scient. Instruments*, 70(2):1546–1552, 1999.

[14] B. Driehuys, G.D. Cates, E. Miron, K. Sauer, D.K. Walter, and W. Happer. High-volume produticion of laser-polarized ^{129}Xe. *Appl. Phys. Lett.*, 69(12):1668–1670, 1996.

[15] I. C. Ruset, S. Ketel, and F. W. Hersman. Optical pumping system design for large production of hyperpolarized ^{129}Xe. *Phys. Rev. Lett.*, 96(5):053002, 2006.

[16] B. Chann, I. Nelson, and T.G. Walker. Frequency-narrowed external cavity diode laser array bar. *Opt. Lett.*, 25:1352–1354, 2000.

[17] N. N. Kuzma, B. Patton, K. Raman, and W. Happer. Fast nuclear spin relaxation in hyperpolarized solid ^{129}Xe. *Phys. Rev. Lett.*, 88(14):147602, 2002.

[18] P. L. Anthony, R. G. Arnold, H. R. Band, H. Borel, P. E. Bosted, V. Breton, G. D. Cates, T. E. Chupp, F. S. Dietrich, J. Dunne, R. Erbacher, J. Fellbaum, H. Fonvieille, R. Gearhart, R. Holmes, E. W. Hughes, J. R. Johnson, D. Kawall, C. Keppel, S. E. Kuhn, R. M. Lombard-Nelsen, J. Marroncle, T. Maruyama, W. Meyer, Z.-E. Meziani, H. Middleton, and J. Morgenstern. Determination of the neutron spin structure function. *Phys. Rev. Lett.*, 71(7):959–962, Aug 1993.

[19] K.P. Coulter, A.B. McDonald, W. Happer, T.E. Chupp, and M.E. Wagshul. Neutron polarization with polarized ^{3}He. *Nucl. Instr. Meth. Phys. Res.Sect. A*, 270(1):90–94, 1988.

[20] T. E. Chupp, R. J. Hoare, R. L. Walsworth, and B. Wu. Spin-exchange-pumped ^{3}He and ^{129}Xe zeeman masers. *Phys. Rev. Lett.*, 72(15):2363–2366, 1994.

[21] H. Imia, M. Narazaki, H.i Inoshita, A. Kimura, and H. Fujiwara. MR imaging of mouse lung using hyperpolarized ^{3}He: Image acquisition and T_1 estimation under spontaneous respiration. *Magn. Reson. Med. Sci.*, 5:57–64, 2006.

[22] J.C. Leawoods, D.A. Yablonskiy, B. Saam, D.S. Geirada, and M.S. Conradi. Hyperpolarized ^{3}He gas production and MR imaging of the lung. *Concepts in Magnetic Resonance*, 13(5):277–293, 2001.

[23] J. Granwehr, J.T. Urban, A.H. Trabesinger, and A. Pines. NMR detection using laser-polarized xenon as a dipolar sensor. *J. Mag. Res.*, 176:125–139, 2005.

[24] S.M. Rubin, S.-Y. Lee, E.J. Ruiz, A. Pines, and D.E. Wemmer. Detection and characterization of xenon-binding sites in proteins by ^{129}Xe NMR spectroscopy. *J. Mol. Biol.*, 322:425–440, 2002.

[25] T.J. Lowery, M. Doucleff, E.J. Ruiz, S. M. Rubin, A. Pine, and D.E. Wemmer. Distinguishing multiple chemotaxis y protein conformations with laser-polarzied ^{129}Xe NMR. *Protein Science*, 14:848–855, 2005.

[26] T.J. Lowery, S.M. Rubin, E.J. Ruiz, M.M. Spence, N. Winssinger, P.G. Schultz, A. Pines, and D.E. Wemmer. Applications of laser-polarizer ^{129}Xe to biomolecular assays. *Mag. Res. Imag.*, 21:1235–1239, 2003.

[27] S. W. Morgan, B. V. Fine, and B. Saam. Universal long-time behavior of nuclear spin decays in a solid. *Phys. Rev. Lett.*, 101:067601, 2008.

[28] G. Schrank, Z. Ma, A. Schoeck, and B. Saam. Characterization of a low-pressure high-capacity ^{129}Xe flow-through polarizer. *Phys. Rev. A*, 80:063424, 2009.

[29] J.H Moore, C.C. Davis, and M.A. Coplan. *Building Scientific Apparatus: A Practical Guide to Design and Construction.* Westview Press, 2002.

[30] R. Seydoux, A. Pines, M. Haake, and J.A. Reimer. NMR with a countinuously circulating flow of laser-polarized ^{129}Xe. *J. Phys. Chem. B*, 103:4629–4637, 1999.

[31] T. Su, G.L. Samuelson, S.W. Morgan, G. Laicher, and B. Saam. Liquid hyperpolarized ^{129}Xe produced by phase exchange in a convection cell. *App. Phys. Lett.*, 85:2429–2431, 2004.

[32] A.L. Zook, B.B. Adhyaru, and C.R. Bowers. High capacity production of >65% spin polarized xenon-129 for NMR spectroscopy and imaging. *J. Mag. Res.*, 159:175–182, 2002.

[33] T. Vo-Dinh. *Biomedical Photonics Handbook.* CRC Press, 2003.

[34] M. E. Wagshul and T. E. Chupp. Optical pumping of high-density Rb with a broadband dye laser and GaAlAs diode laser arrays: Application to ^{3}He polarization. *Phys. Rev. A*, 40(8):4447–4454, Oct 1989.

[35] M. V. Romalis, E. Miron, and G. D. Cates. Pressure broadening of Rb D_1 and D_2 lines by ^{3}He, ^{4}He, N_2, and Xe: Line cores and near wings. *Phys. Rev. A*, 56(6):4569–4578, Dec 1997.

[36] E. Hecht. *Optics.* Addison Wesley Longman, Inc., 1997.

[37] S.R. Breeze, S. Lang, I. Moudrakovski, C.I. Ratcliffe, J.A. Ripmeester, G. Santyr, B. Simar, and I. Zuger. Coatings for optical pumping cells and short-term storage of hyperpolarized xenon. *J. App. Phys.*, 87:8013, 2000.

[38] A. B.-A. Baranga, S. Appelt, M.V. Romalis, C.J. Erickson, A.R. Young, G.D. Cates, and W. Happer. Polarization of ^{3}He by spin exchange with optically pumped Rb and K vapors. *Phys. Rev. Lett.*, 80(13):2801–2804, 1998.

[39] R.C. Weast, editor. *Handbook of Chemistry and Physics.* CRC Press, 52 edition, 1971.

[40] B. Driehuys, D. Zollinger, D. Deaton, K.C. Hasson, and A. Langhorm. Polarized gas accumulators and heating jackets and associated gas collection method and thaw methods and polarized gas products. *U.S. Patent 6,305,190 B1*, October 23, 2001.

[41] C. Kittel. *Introduction to Solid State Physics.* John Wiley and Sons, Inc., 2004.

[42] A. B.-A. Baranga, S. Applet, C.J. Erickson, A.R. Young, and W. Happer. Alkali-metal-atom polarization imaging in high-pressure optical-pumping cells. *Phys. Rev. A*, 58(3):2282–2294, 1998.

[43] S. Appelt, A.B.-A. Baranga, C.J. Erickson, M.V. Romalis, A.R. Young, and W. Happer. Theory of spin-exchange optical pumping of ^{3}He and ^{129}Xe. *Phys. Rev. A*, 58(2):1412–1439, Aug 1998.

[44] M. Mehring and V.A. Weberruß. *Objected-Oriented Magnetic Resonance: Classes and Objects, Calculations and Computations.* Academic Press, 2001.

[45] F. Schuller. *The Liouville Space Formalism in Atomic Spectroscopy.* Heron Press Ltd., 2002.

[46] D. Budker, D.F. Kimball, and D.P. Demille. *Atomic Physics: An Exploration Through Problems and Solutions.* Oxford University Press, 2004.

[47] C.P. Slichter. *Principles of Magnetic Resonance.* Springer, 1996.

[48] B. H. Han, S. Park, and S. Y. Lee. Gradient waveform synthesis for magnetic propulsion using MRI gradient coils. *Phys. Med. Biol.*, 53:4639–4649, 2008.

[49] B. Chann, E. Babcock, L. W. Anderson, and T. G. Walker. Measurements of ^{3}He spin-exchange rates. *Phys. Rev. A*, 66(3):032703, Sep 2002.

[50] S. Appelt, T Ünlü, K Zilles, N.J. Shah, S. Baer-Long, and H. Halling. Experimental studies of rubidium absolute polarization at high temperatures. *Appl. Phys. Lett.*, 75(3):427–429, 1999.

[51] A. Fink, D. Baumer, and E. Brunner. Production of hyperpolarized xenon in a static pump cell: Numerical simulations and experiments. *Phys. Rev. A*, 72(5):053411, 2005.

[52] T.J. Killian. Thermionic phenomena caused by vapors of rubidium and potassium. *Phys. Rev.*, 27(5):578–587, May 1926.

[53] M. E. Wagshul and T. E. Chupp. Laser optical pumping of high-density Rb in polarized ^{3}He targets. *Phys. Rev. A*, 49(5):3854–3869, May 1994.

[54] I.B. Gornushkin, L.A. King, B.W. Smith, N. Omenetto, and J.D. Winefordner. Line broadening mechanisms in the low pressure laser-induced plasma. *Spectrochimica Acta Part B: Atomic Spectroscopy*, 54:1207–1217, 1999.

[55] I.A. Nelson and T.G. Walker. Rb-Xe spin relaxation in diulte Xe mixtures. *Phys. Rev. A*, 65:012712, 2001.

[56] D. K. Walter, W. M. Griffith, and W. Happer. Magnetic slowing down of spin relaxation due to binary collisions of alkali-metal atoms with buffer-gas atoms. *Phys. Rev. Lett.*, 88(9):093004, Feb 2002.

[57] S. Kadlecek, L.W. Anderson, and T.G. Walker. Field dependence of spin relaxation in dense Rb vapor. *Phys. Rev. Lett.*, 80(25):5512–5515, 1998.

[58] S. Kadlecek, T. Walker, D.K. Walter, C. Erickson, and W. Happer. Spin-axis relaxation in spin-exchange collisions of alkali-metal atoms. *Phys. Rev. A*, 63:052717, 2001.

[59] S. Kadlecek, L.W. Anderson, C.J. Erickson, and T.G. Walker. Spin relaxation in alkali-metal $^1\sigma_g^+$ dimers. *Phys. Rev. A*, 64:052717, 2001.

[60] S. Kadlecek. *Spin Relaxation in Alkali Metal Vapors.* PhD thesis, University of Wisconsin-Madison, 1999.

[61] B. Chann, I.A. Nelson, L.W. Anderson, B. Driehuys, and T.G. Walker. ^{129} Xe-Xe molecular spin relaxation. *Phys. Rev. Lett.*, 88(11):113201, 2002.

[62] W. Happer, E. Miron, S. Schaefer, D. Schreiber, W. A. van Wijngaarden, and X. Zeng. Polarization of the nuclear spins of noble-gas atoms by spin exchange with optically pumped alkali-metal atoms. *Phys. Rev. A*, 29(6):3092–3110, Jun 1984.

[63] D. K. Walter, W. M. Griffith, and W. Happer. Energy transport in high-density spin-exchange optical pumping cells. *Phys. Rev. Lett.*, 86(15):3264–3267, Apr 2001.

[64] B. Chann, E. Babcock, L. W. Anderson, and T. G. Walker. Skew light propagation in optically thick optical pumping cells. *Phys. Rev. A*, 66(3):033406, Sep 2002.

[65] B. Chann. *Studies of Spin-Exchange Optical Pumping.* PhD thesis, University of Wisconsin-Madison, 2003.

[66] B. Schoenborn, H. Watson, and J. Kendrew. Binding of xenon to sperm whale myoglobin. *Nature*, 207:28–30, 1965.

[67] B. Schoenborn. Binding of xenon to horse hemoglobin. *Nature*, 208:760–762, 1965.

[68] R.F. Tilton and I.D. Kuntz. Nuclear magnetic resonance studies of xenon-129 with myoglobin and hemoglobin. *Biochemistry*, 21:6850, 1982.

[69] S.M. Rubin, M.M. Spence, A. Pines, and D.E. Wemmer. Characterization of the effects of nonspecific xenon-protein interactions on ^{129}Xe chemical shifts in aqueous solution: Further development of xenon as a biomolecular probe. *J. Mag. Res.*, 152:79, 2001.

[70] A. Cherubini and A. Bifone. Hyperpolarised xenon in biology. *Prog NMR Spec.*, 42:1–30, 2003.

[71] P. Ascenzi, A. Bocedi, M. Bolognesi, A. Spallarossa, M. Coletta, R.D. Cristofaro, and E. Menegatti. The bovine basic pancreatic trypsin inhibitor (kunitz inhibitor): A milestone protein. *Curr. Pro. Pep. Sci.*, 4:231–251, 2003.

[72] D.P. Goldenberg, R.W. Frieden, J.A. Haack, and T.B. Morrison. Mutational analysis of a protein folding pathway. *Nature*, 338:127–132, 1989.

[73] J.X. Zhang and D.P Goldenberg. Mutational analysis of the BPTI folding pathway: II. effect of aromatic $\rightarrow$ leucine substitutions on folding kinetics and thermodynamics. *Protein Sci.*, 6:1563–1576, 1997.

[74] G. Bulaj and D.P Goldenberg. ϕ-values for BPTI folding intermediates and implications for transition states. *Nature Struct. Biol.*, 8:326–330, 2001.

[75] G. Bulaj and D.P. Goldenberg. Mutational analysis of hydrogen bonding residues in the BPTI folding pathway. *J. Mol. Biol.*, 313:639–656, 2001.

[76] S.A. Beeser, D.P Goldenberg, and T.G. Oas. Determinants of backbone dynamics in native BPTI: Cooperative influence of the 14-38 disulfide and the Tyr 35 side chain. *J. Mol. Biol.*, 284:1581–1596, 1998.

[77] S.A. Beeser, D.P Goldenberg, and T.G. Oas. Enhanced protein flexibility caused by a destabilizing amino acid replacement in BPTI. *J. Mol. Biol.*, 269:154–164, 1997.

[78] W.M. Hanson, S.A. Besser, T.G. Oas, and D.P. Goldenberg. Identification of a residue critical for maintaining the functional conformation of BPTI. *J. Mol. Biol.*, 333:425–441, 2003.

[79] A.T. Danishefsky, D. Housset, K.S. Kim, F. Tau, J. Fuchs, C. Woodward, and A. Wlodawer. Crevice-forming mutants in the rigid core of bovine pancreatic trypsin inhibitor: Crystal structures of F22A, Y23A, N43G, and F45A. *Protein Sci.*, 2:557–587, 1993.

[80] W. M. Hanson, G. Domek, M. Horvath, and D. P. Goldenberg. Rigidification of a flexible protease inhibitor variant upon binding to trypsin. *J. Mol. Biol.*, 366:230–243, 2007.

[81] A.D. Bain. Chemical exchange in NMR. *Prog NMR Spec.*, 43:63–103, 2003.

[82] S. M. Rubin, M. M. Spence, B. M. Goodson, D. E. Wemmer, and A. Pines. Evidence of nonspecific surface interactions between laser-polarized xenon and myoglobin in solution. *PNAS*, 97(17):9472–9475, August 2000.

[83] C. Hilty, T. J. Lowery, D.E. Wemmer, and A. Pines. Spectrally resolved magnetic resonance imaging of a xenon biosensor. *Angew. Chem. Int. Ed.*, 45:70–73, 2006.

[84] D. Baumer, E. Brunner, P. Blümler, P.P. Zänker, and H.W. Spiess. NMR spectroscopy of laser-polarized ^{129}Xe under continuous flow: a method to study aqueous solutions of biomolecules. *Angew. Chem. Int. Ed.*, 45:7282–7284, 2006.

[85] B. Kassell. Bovine trypsin-kallikrein inhibitor (kunitz inhibitor, basic pancreatic trypsin inhibitor, polyvalent inhibitor from bovine organs). *Methods Enzymol.*, 19:844–852, 1970.

[86] R. Seydoux. *NMR of ^{3}He dissolved in liquids and solids.* PhD thesis, University of Basel, 1995.

[87] L.-Q. Wang, Y. Shin, W.D. Samuels, G.J. Exarhos, I.L. Moudrakovski, V.V. Terskikh, and J.A. Ripmeester. Magnetic resonance studies of hierarchically ordered replicas of wood cellular structures prepared by surfactant-mediated mineralization. *J. Phys. Chem. B*, 107(50):13793–13802, 2003.

[88] R.W. Mair, M.I. Hrovat, S. Patz, M.S. Rosen, I.C. Ruset, G.P. Tupulos, L.L. Tsai, J.P. Butler, F.W. Hersman, and R.L. Walsworth. ^{3}He lung imaging in an open access, very-low-field human magnetic resonance imaging system. *Mag. Res. Med.*, 53:745–749, 2005.

[89] Xemed webpage. http://xemed.com/.

[90] W.E. Groth, K. Beyerle, E. Nann, and K.H. Welge. Enrichment of uranium isotopes by the gas centrifuge method. In *Peaceful Uses of Atomic Energy*, page 439, 1958.

[91] R. van Wissen, M. Golmbok, and J.J.H. Brouwers. Separation of carbon dioxide and methane in continuous countercurrent gas centrifuges. *Chem. Eng. Sci.*, 60:4397–4407, 2005.

[92] M. Golombok and L. Chewter. Centrifugal separation for cleaning well gas streams. *Ind. Eng. Chem. Res.*, 43:1743–1739, 2004.

[93] S.R. Auvil and B.W. Wilkinson. The steady and unsteady state analysis of a simple gas centrifuge. *A. I. Ch. E. J.*, 22(3):564–568, 1976.